# A Study of the Effects of Solution and Process Parameters on the Electrospinning Process and Nanofibre Morphology

by

Chitral Jayasanka Angammana

A thesis
presented to the University of Waterloo
in fulfillment of the
thesis requirement for the degree of
Doctor of Philosophy
in
Electrical and Computer Engineering

Waterloo, Ontario, Canada, 2011

# AUTHOR'S DECLARATION

I hereby declare that I am the sole author of this thesis. This is a true copy of the thesis, including any required final revisions, as accepted by my examiners.

I understand that my thesis may be made electronically available to the public.

# Abstract

Nanofibres have been the subject of recent intensive research due to their unique properties, especially their large surface-area-to-volume ratio, which is about one thousand times higher than that of a human hair. They also have several other remarkable characteristics, such as flexibility in surface functionality, superior mechanical properties such as stiffness and tensile strength, their capacity to be formed into a variety of shapes, and the fact that they can be produced from a wide range of organic and inorganic polymers. These outstanding properties make polymer nanofibres the optimal candidates for providing significant improvement in current technology and for opening the door to novel applications in many research areas.

Electrospinning is a straightforward and inexpensive process that produces continuous nanofibres from submicron diameters down to nanometre diameters. Many researchers have successfully electrospun a variety of polymer solutions into nanofibres. However, electrospinning any polymer solution directly is not straightforward or simple because of the number of parameters that influence the electrospinning process. The characteristics of the electrospun jet and the morphology of the resultant fibres are highly dependent on the properties of the polymer solution. In addition, what are favourable processing conditions for one polymer solution may not be suitable for another solution. A literature review revealed that there is no clear understanding of the behaviour of the electrospun jet and the way in which fibre morphology varies with variations in influential parameters. In addition, reported results contain significant inconsistencies and very little research has examined the effects of electrical parameters such as the electric field, the polarity of the electrode, and the conductivity and permittivity of the solution. Furthermore, no research has been conducted with respect to optimizing the electrospinning process.

In this thesis, a comprehensive study was carried out by giving a special attention to the effects of electric field that have not been thoroughly investigated in the past. The electric field between the needle tip and the collector plate was altered by varying the applied voltage, distance between the needle tip and the collector plate, the inner diameter of the needle, and polarity of the voltage. Based on the experimental work, it was found that the behavior of Taylor cone, the length of the straight jet portion, and whipping jet region is highly influenced by the distribution of the electric field between the needle tip and the collector plate. Based on the stability of the Taylor cone, it was concluded that the stable operating region of the electrospun jet is a very narrow region and it is between 0.9 – 1.1kV/mm for the range of experiments that were carried out in this study. The length of the straight jet portion of the electrospun jet shows a linear relationship to the applied electric field at the tip of the fluid droplet and the whipping jet region is influenced by both the electric field at the tip of the fluid droplet and the distance between the needle and the collector plate. A confirmation were made that there must be enough distance between the needle tip and the collector plate (>200mm) to operate over the complete range of voltages without affecting drying of

nanofibres. It was also concluded that the morphology and diameter of the collected nanofibres depend significantly on both the length of the straight jet portion and size of the whipping region.

The effects of polarity of the applied voltage on the electrospinning process and nanofibre morphology were investigated using the positive, negative, and AC voltages. However, it was found that the electrospinning can not be achieved with the application of 60Hz AC voltage. It was observed that the behavior of Taylor cone, the straight jet portion, and the whipping jet region depend on the polarity of the applied voltage. During the study, it was accomplished that the reason for this different behavior is the disparity of ionization in the polymer solution with the application of positive and negative high voltages.

In this thesis, the effects of multi-needle arrangements on the electrospinning process and fibre morphology were also explained. Finite element method (FEM) simulation results revealed that the local electric field strength around each needle tip weakens significantly in the case of multi-needle schemes due to the mutual influence of other needles in the arrangement compared to the single-needle system. The spacing between the needles was varied, and the effects of the needle spacing were examined. The experimental and simulation results were concealed the correlation between the degree of field distortion and the variation in the measured vertical angle of the straight jet portion for different needle spacing. It was concluded that the local field deterioration at the needle tips in multi-needle schemes degrades the electrospinning process significantly and produces considerable variation in the fibre morphology even though the influence of needle spacing on the average jet current and the fibre diameter are not very significant.

In this work, the effects of conductivity and ionic carriers on the process of electrospinning and hence on the morphology of nanofibres were studied using polyethylene oxide (PEO) and polyacrylic acid (PAA) aqueous solutions. Different salts including lithium chloride (LiCl), sodium chloride (NaCl), sodium fluoride (NaF), sodium bicarbonate ($NaHCO_3$), potassium chloride (KCl), and cesium chloride (CsCl) were added in different concentrations to the polymer solutions for introducing different ionic carriers into the solution. The results showed that the average fiber diameter decreases with increase in the conductivity of the solution. In addition, it was discovered that the formation of Taylor cone highly depends on the conductivity in the polymer solution. Formation of multi-jets at the fluid droplet when the conductivity of the polymer solution is increased during the electrospinning was also observed. These behaviors were completely explained using the distribution of the surface charge around the electrospun jet and the variation in the tangential electric field along the surface of the fluid droplet. The stretching of the polymer jet can be related to the amount of ionic carries and the size and mobility of positive and negative ions. The increasing amount of ionic carriers and smaller size positive ions enhance the stretching of the electrospun jet. In contrast, the lesser diameter negative ions decrease the stretching of the electrospun jet. The morphology of electrospun nanofibres can also be varied by altering the type of ionic carriers.

A charge modifier, which is a container that is used to hold a solvent surrounding the needle tip during the electrospinning, was introduced to facilitate the electrospinning of insulating and high conductivity polymer solutions. The co-axial flow of the filled solvent on the outer surface of the polymer solution helps to induce enough surface charges during electrospinning and it also keeps the electric field tangential to the fluid surface during the process. Therefore, the introduction of charge modifier greatly enhanced the electrospinning behavior of highly insulating and conductive polymer solutions and liquids. The developed charge modifier method was verified by using sodium alginate which is a biopolymer that cannot electrospin alone due to its high electrical conductivity and silicone rubber which is an insulating liquid polymer at room temperature.

One of the most commonly used theoretical model of the electrospinning process was modified to incorporate the non-uniform characteristics of the electric field at the tip of the needle. The non-uniform electric field between the needle tip (spinneret) and the collector plate was calculated based on the charge simulation technique (CST). It gives a better representation of the true electrospinning environment compared to the uniform field calculation in the existing model. In addition, a localized approximation was used to calculate the bending electric force acting on the electrospinning jet segments. It was also introduced a constant velocity to initiate the electrospinning jet during simulation. The incorporated modifications gave better results that closely match with the real electrospinning jet. The modified electrospinning model was used to understand the effects of parameters on the electrospinning process and fibre morphology.

# Acknowledgements

First and foremost, I would like to express my profound gratitude, and thanks to my supervisor, Prof. Shesha Jayaram for her continuous financial support, invaluable advice, and constant guidance throughout the duration of this work.

I also wish to express my appreciation to my PhD Committee (Dr. Hany Aziz, Dr. M.P. Anantram, Dr. Bo Cheng Cui, Dr. Leonardo Simon, Dr. Malay Mazumder, and Dr. Ting Tsui) for their valuable suggestions and constructive comments.

I would also like to thank Dr. Loong Tak Lim in the department of Food Science at the University of Guelph for his great support during the initial period of this project.

Also, I will always remember Dr. Mithulananthan Nadarajah for his help and encouragement for pursuing a PhD at the University of Waterloo.

I also extend my thanks to Dr. Edward Cherney and my friends in the high voltage engineering laboratory at the University of Waterloo: Ahmed, Alex, Ali, Emad, Isaias, Michael, Omar, Rafat, Rina, Saeed, Saleh, Sarajit, Susan, and Utkarsh, made it a pleasant place to work.

In particular, I would like to give a special thank to Emad and Susan whom I shared the office and lab space during these years and shared many opinions, complaints, and jokes.

I am grateful to my dear friends Nandana, Ishari, Subasha, Kosala, and Sahan for their kind attention and help during the period of transition when I first arrived in Canada.

My thanks go to Ishari Jayabahu in the department of Biology at the University of Waterloo and Ana Cristina Vega Lugo, Solmaz Alborzi, and Yucheng Fu at the University of Guelph for their valuable help during this work.

Finally, my deepest gratitude goes to all the members of my family and to my friends, for their life-long love, care, and support.

The financial support provided by NSERC of Canada and the Fellowship from Waterloo Institute of Nanotechnology (WIN) are also greatly appreciated.

Last but not least, I would like to thank Mrs. Barbara Trotter for proofreading this thesis.

# Dedication

*To my lovely wife Suramya,*

*To my dear parents, sisters, and grand father*

# Table of Contents

# List of Tables

# List of Figures

# Chapter 1
# Introduction

## 1.1 Introduction

Nanotechnology deals with nanostructures or matter at dimensions in the nanometre scale, where unique physical, chemical, and biological properties can appear in materials that can be used for novel applications. Nanostructures are structures or objects that have at least one dimension at the nanometre scale, which is one-billionth of a meter in the SI unit system. As examples, a nanoparticle can be considered a zero-dimensional nanostructure, whereas a nanotube, nanofibre, or nanorod is a one-dimensional nanostructure [1]. Similarly, a nanoplatelet or nanodisk can be considered two-dimensional nanostructures.

Polymer nanofibres are a type of one-dimensional nanostructure, with diameters varying from 1 nm to 1000 nm. Their nanometre diameter provides polymer nanofibres with several outstanding characteristics, such as a very large ratio of surface area to volume (aspect ratio). Infact, for a nanofibre, this ratio can be as large as $10^3$ times of that of a microfibre. Other advantages include flexibility in surface functionality, and superior mechanical performance compared with any other existing form of the material [2]. These excellent properties make polymer nanofibres optimal candidates for many important applications and offer the potential for significant improvements in current technology and the development of applications in new areas.

A number of processing techniques, such as drawing, template synthesis, phase separation, self-assembly, and electrospinning, have recently been used for preparing polymer nanofibres. Drawing is a process that can make very long single nanofibres one by one using materials that can undergo strong deformation while being drawn. However, with this technique, only viscoelastic materials can be used to form nanofibres because the material must be cohesive enough to support the stresses that develop during pulling [1-4]. Template synthesis uses hard templates with pores, such as membranes, in order to produce either solid or hollow nanofibres. The most significant advantage of template synthesis is that this process can be used to make nanofibres from a variety of materials, such as conducting polymers, metals, semiconductors, and carbons [1, 2, 5, and 6]. The phase separation method consists of five major steps: polymer dissolution, gelation, solvent extraction, freezing, and freeze drying. The result is a porous nanofibrous structure [1]. The main drawback of this process is the relatively long time required for transferring the solid polymer into a nano-porous form. Self-assembly is a “bottom-up” approach, in which nanofibres are assembled molecule by molecule in order to produce well-defined structures and functions [7-9]. However, self-assembly is also time-consuming for producing

continuous polymer nanofibres [2]. On the other hand, electrospinning is a straightforward and inexpensive process that produces continuous nanofibres from submicron diameters down to nanometre diameters. Table 1.1 shows a comparison of these processing techniques for obtaining nanofibres. As shown, the advantageous of electrospinning outweigh those of other nanofibre production techniques; the electrospinning process can thus be considered the only method that can be further developed for the mass production of continuous nanofibres from a variety of polymers [1].

Table 1.1: Comparison of processing techniques for obtaining nanofibres.

| Process | Technology | Scalability | Repeatability | Simplicity | Controllability |
|---|---|---|---|---|---|
| Drawing | Laboratory scale | No | Yes | Yes | No |
| Template synthesis | Laboratory scale | No | Yes | Yes | Yes |
| Phase separation | Laboratory scale | No | Yes | Yes | No |
| Self-assembly | Laboratory scale | No | Yes | No | No |
| Electrospinning | Industrial processing | Yes | Yes | Yes | Yes |

## 1.2 Electrospinning

The history of electrospinning dates back to the nineteenth century. It was first observed by Rayleigh in 1897 and studied in detail by Zeleny in 1914 with respect to electrospray technique [10]. In 1934, Formhals developed an experimental setup for producing artificial filaments using electric charges, and it was accepted and patented as a viable fibre-spinning technique in the late 1930s [11]. Thereafter, Taylor, Saville, Denn, and others made significant contributions to electrically driven jets and laid the groundwork for the electrospinning research that took place in the late 1960s and early 1970s [12-16]. With the rapid development of nanotechnology since the 1990s, researchers and scientists worldwide have been examining the process from a new perspective.

Electrospinning is a straightforward and inexpensive process that produces continuous nanofibres from submicron diameters down to nanometre diameters. The process involves an electrically charged jet of polymer solution or polymer melt consisting of polymer molecules with a chain sufficiently long that they do not break up due to Rayleigh instability. The surface of the fluid droplet that is held at the

spinneret by its own surface tension becomes electrostatically charged with the application of high voltage. The interaction of the electrical charges in the polymer fluid with the external electric field result in the formation of the well-known Taylor cone [12], as shown in Fig. 1.1 (a). When the cone is subjected to very strong electric field with an appropriate field gradient at the tip of the cone, the droplet becomes unstable, and a single fluid jet is drawn out from the head of the Taylor cone, as shown in Fig. 1.1 (b). Once the jet flows away from the Taylor cone in a nearly straight line, the travelling liquid jet is subjected to a variety of forces, such as a Coulomb force, an electric force imposed

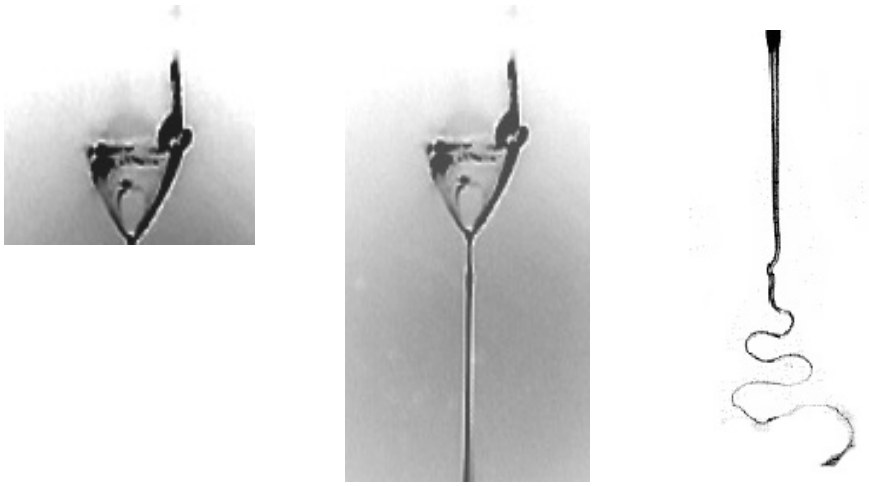

(a) (b) (c)

Fig. 1.1: (a) Taylor cone; (b) A single fluid jet drawn out from the Taylor cone; (c) Bending instability [13, 17].

by the external electric field, a viscoelastic force, a surface tension force, a gravitational force, and an air drag force [18]. The onset of bending instability can thus be observed. The bending takes a complex path, and other changes in the shape also occur, as illustrated in Fig. 1.1(c). The electrical forces stretch and thin the jets by very large ratios, and the solvent finally evaporates, and nanofibres can then be collected on the target.

The development of the electrospinning technique has provided significant momentum to the search for potential applications of nanofibres. The demand for novel materials has been increasing, and electrospun nanofibres could therefore mark a new era in materials science. As can be seen in Fig. 1.2, possible major applications can be categorized as bioengineering, environmental engineering, biotechnology, medical science, energy, electronics, defence, and security [1, 2, 19-25].

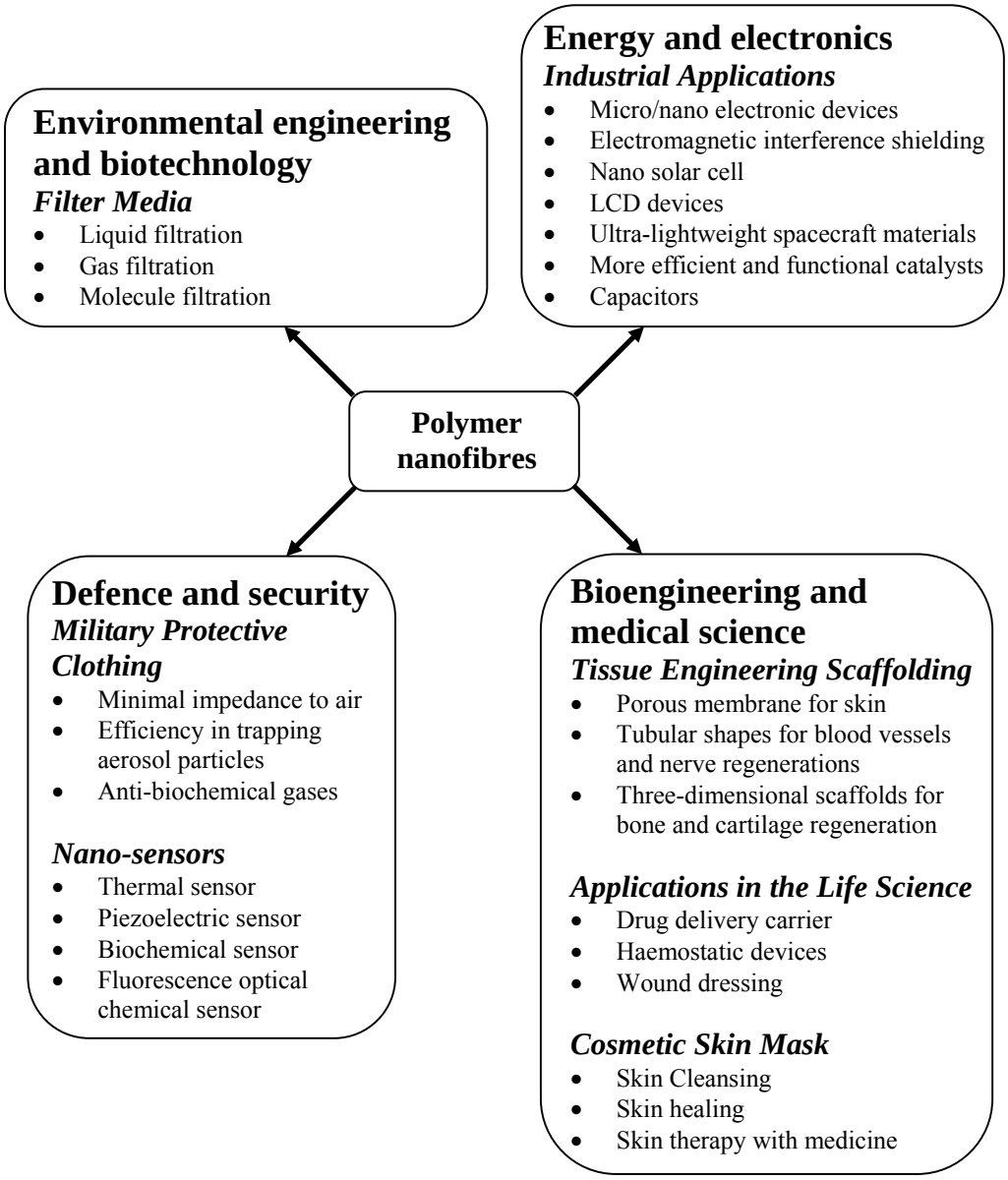


Fig. 1.2: Potential applications of electrospun nanofibres.

## 1.3 Materials

Numerous materials are used for electrospinning: most are polymers, composites, semiconductors, or ceramics [26]. A large number of polymers, both synthetic and natural, have been successfully electrospun into nanofibres, mostly from polymer solutions that are used in a variety of applications. Most of the electrospinning tests have been performed in research laboratories. It is important to mention that it is possible to electrospin all polymers into nanofibres, provided that the molecular weight of the polymers is sufficiently large and that the solvent can be evaporated quickly enough

during the process [19]. The specific properties of the material must be considered for each type of application. The electrospinning process and the apparatus may be modified for different polymers in order to produce electrospun fibres that have the desired morphology and properties.

### 1.3.1 Polymers

A polymer is a large molecule built up by the repetition of small, simple chemical units, known as monomers. In some cases, the repetition is linear, much as a chain is built from individual links. In other cases, the chains are branched or interconnected to form three-dimensional networks. An example of a polymer is polyethylene, which consists of repeating units of $[-CH_2CH_2-]_n$, as shown in Fig. 1.3. The length of the polymer chain is specified by the number of units repeated in the chain, which is called the degree of polymerization (DP) [27].

Many synthetic and natural polymers as well as polymer blends have recently been electrospun to form nanofibres for a variety of applications. Table A-1 in Appendix A shows a list of polymers that have already been electrospun successfully into nanofibres. Two of the areas with the greatest potential for using electrospun nanofibres are bioengineering and biotechnology. For many of these biomedical applications, natural polymers provide a distinct advantage compared with synthetic polymers because the material used must be bio-compatible and biodegradable. An additional advantage of electrospinning is that this method offers the ability to process natural polymers such as DNA, which can not be proceeded with conventional fibre-spinning techniques [28]. Natural polymer nanofibres are highly desirable for applications such as tissue engineering, drug delivery, and wound dressings because they degrade naturally after reacting with enzymes. The use of several proteins and polysaccharides, such as bombyx mori silk, casein, cellulose, chitosan, collagen, gelatine, wheat gluten, along with several other natural polymers has been investigated using electrospinning [28-34].

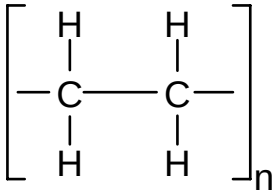


Fig.1.3: Molecular structure of polyethylene.

Polymer blends or polymer mixtures are a class of materials analogous to metal alloys, in which two or more polymers are blended to create a new material that has different physical properties. Because of limitations with respect to their molecular weights and solubility, many functional polymers

are not suitable for electrospinning. One of the most effective ways of solving this difficulty is to blend them with polymers that are well suited for electrospinning.

## 1.4 Electrospinning Apparatus

Fig. 1.4 illustrates a schematic diagram of a typical experimental apparatus used to perform the electrospinning experiments, which has been used by several researchers for their electrospinning experiments [18, 19, 26, 35-37]. The polymer solution is forced through a syringe needle unit at a constant rate using a syringe pump, resulting in the formation of a drop of polymer solution at the needle tip. A high-voltage DC source is used in order to apply a high voltage, typically 10kV or higher, between the needle and the collector plate. Other modifications, especially different collector designs, have been added to the electrospinning apparatus in order to overcome a number of the limitations of typical electrospinning schemes and to enhance the performance of the electrospun fibrous mesh [26].

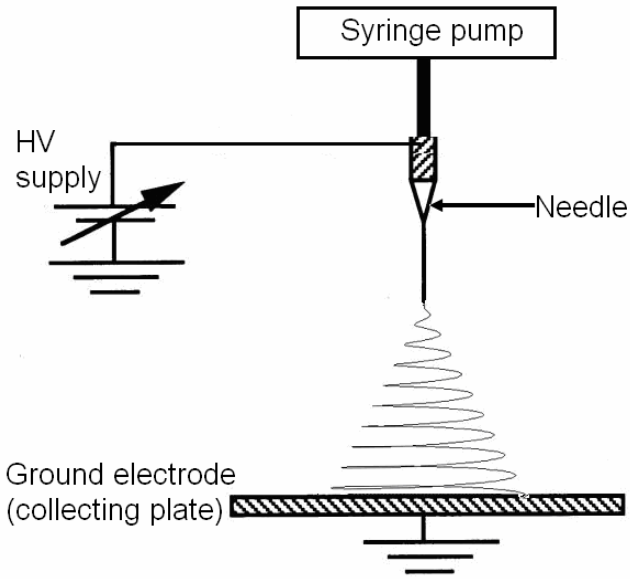


Fig. 1.4: Schematic of a typical electrospinning setup.

Although many researchers have used single-needle systems for electrospinning, the low fluid throughput during spinning has limited the industrial use of single-needle systems. To meet the requirement for high liquid throughput, several multi-jet schemes have recently been tested [38, 39]. In addition, the use of an electrospinning apparatus that does not have spinnerets (needleless electrospinning) and free-surface electrospinning have also been investigated by a few researchers [40-46]. Even more recently, as shown in Fig. 1.5, several types of commercial and laboratory-scale

electrospinning equipment have become available in the market, such as Elmarco's Nanospider™ technology, a handheld electrospinning machine developed by the Marburg group, and the NANON-01A from the Mechanics Electronics Computer Corporation (MECC).

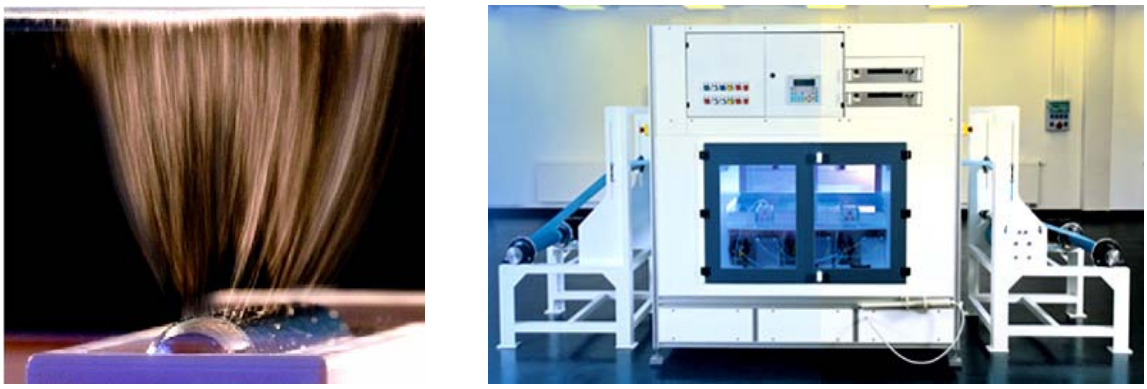

(a) (b)

Fig. 1.5: (a) Nozzle-free Nanospider™ ; (b) Nanospider (NS) organic production lines 1000 [47].

## 1.5 Motivation

Nanofibres have been the subject of recent intensive research due to their unique properties, especially their large surface-area-to-volume ratio, which is about one thousand times higher than that of a human hair. They also have several other remarkable characteristics, such as flexibility in surface functionality, superior mechanical properties such as stiffness and tensile strength, their capacity to be formed into a variety of shapes, and the fact that they can be produced from a wide range of organic and inorganic polymers [17]. These outstanding properties make polymer nanofibres the optimal candidates for providing significant improvement in current technology and for opening the door to novel applications in many research areas. Although, the electrospinning is a century-old technology, the popularity of nanofibres is making it becoming a dynamic research topic among the scientific community because of its simplicity and flexibility with respect to the production and control of nanofibre structures.

Many researchers have successfully electrospun a variety of polymer solutions into nanofibres. Moreover, recent research related to electrospun fibres has explored a number of new electospinnable materials that also produce nanofibre structures that have different characteristics. However, electrospinning any polymer solution directly is not straightforward or simple because of the number of parameters that influence the electrospinning process. The characteristics of the electrospun jet and the morphology of the resultant fibres are highly dependent on the properties of the polymer solution. In addition, what are favourable conditions for one polymer solution may not be suitable for another

solution. A literature review revealed that there is no clear understanding of the behaviour of the electrospun jet and the way in which fibre morphology varies with variations in influential parameters. In addition, reported results contain significant inconsistencies and very little research has examined the effects of electrical parameters such as the electric field, the polarity of the electrode, and the conductivity and permittivity of the solution. Furthermore, no research has been conducted with respect to optimizing the electrospinning process. A comprehensive investigation is therefore needed in order to determine methods of predicting the boundary conditions and of optimizing both the solution and the processing parameters for electrospinning.

## 1.6 Research Objectives

The main objectives of this research are to provide a comprehensive understanding of the effects of solution and process parameters on the electrospinning process and fibre morphology, and to optimize the electrospinning process in order to increase the speed and reliability of nanofibre production. The following are the specific objectives of this study:

1. Investigate the effects of electric field in the electrospinning process and the resulting nanofibre morphology, including the effects of multi-needle arrangements on the electrospinning process and fibre morphology.
2. Study the effects of the conductivity of the solution on the electrospinning process and on the morphology of the electrospun fibre.
3. Investigate the effects of ionic carriers on the electrospinning process and hence, on the nanofibre morphology.
4. Use parametric study to design a novel system for improving and controlling the performance of the electrospinning process.
5. Evaluate and compare the results of the experimental tests and numerical simulations using a variety of polymer solutions.

## 1.7 Thesis Organization

This thesis is organized into eight chapters:

1. Chapter 2 discusses the parameters that govern the electrospinning process and reviews the parametric studies that have been completed by several research groups.

2. Chapter 3 reviews the theoretical formulations and modelling techniques that have been developed for studying the electrospun jet and the electrospinning process. It also presents the improved electrospinning model incorporating the non-uniformity of the electric field.
3. Chapter 4 provides the details of experimental procedures used in this work and the techniques and results of the electric field simulation at the tip of the fluid droplet.
4. Chapter 5 reports the results of the investigation into the effects of the electric field on the electrospinning process and on fibre morphology.
5. Chapter 6 presents the results of the studies of the effect of the conductivity of the polymer solution and the effect of the ionic carries on the electrospinning process and on fibre morphology.
6. Chapter 7 discusses the theoretical aspects of the experimental observations.
7. Chapter 8 includes conclusions and recommendations for future research.

# Chapter 2
# Parametric Study

## 2.1 Introduction

The electrospinning process and the morphology and diameter of electrospun fibres all depend on the properties of the polymer solution, which include viscosity, conductivity, and surface tension; processing conditions, which include the voltage applied, the distance between the needle tip and the collector plate, the needle diameter, the temperature, and the shape of the collector plate; and environmental conditions, which include air pressure and humidity. These parameters can be influenced so that they either change the morphology of the nanofibres from a beaded structure to a porous structure or change the diameter of the fibre from the micrometer to the nanometer scale. They also generally affect the characteristics of the electrospun jet, such as the straight jet portion, the instability region, and the jet path. These parameters can be divided into three main categories: (1) the processing conditions, (2) the intrinsic properties of the polymer solution, and (3) the ambient parameters [1, 48]. The following sections provide a comprehensive review of the effects of these parameters on the electrospinning process and the fibre morphology produced.

## 2.2 Processing Conditions

Processing conditions play a major role in the electrospinning process because the entire electrospinning process is governed by the external electric field produced by the applied voltage and the induced electric field caused by the free and induced charges on the jet surface. In addition, the processing conditions and external parameters also have a significant effect on the diameter and morphology of the nanofibres. The electric field between the needle tip and the target can be controlled through variation parameters such as the applied voltage, the distance between the needle tip and the target, the shape of the collector, and the diameter of the needle. All of these factors are therefore considered in the category of processing conditions. Processing conditions also include parameters such as the feed rate and temperature of the solution. These parameters are reviewed in detail in the following subsections.

### 2.2.1 Voltage

One of the major parameters that can be used to change the electric field is the voltage applied between the two electrodes: the needle and the collector plate. Generally, either a positive or a negative voltage

of more than 6kV is required in order to cause the jet to initiate from the Taylor cone [12]. However, depending on the other processing conditions and solution parameters, a higher voltage may be required. If the applied voltage is higher, a greater amount of charge will cause the jet to accelerate faster, and more solution will be drawn out from the tip of the needle [1]. Fig. 2.1 shows the variation in the jet initiation with an increased electric field. As the figure shows, at a critical electric field (or voltage), the Taylor cone is no longer observed, and the jet seems to emanate directly from the nozzle [49].

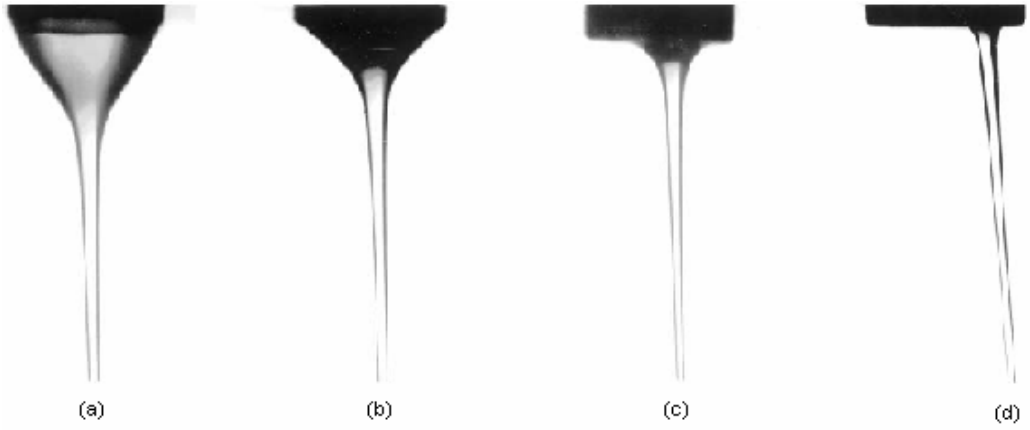


Fig. 2.1: Stable jet profile of a PEO-water solution with an increased electric field: (a) E = 0.047kV/mm; (b) E = 0.053kV/mm; (c) E = 0.060kV/mm; (d) E = 0.1kV/mm [49].

With each increase in the applied voltage the resultant electric field between the needle and the target increases as well, which leads to greater stretching of the solution due to the larger columbic force between the surface charges. An increase in the applied voltage therefore leads to a decrease in the diameter of the electrospun nanofibres [37, 50, 51]. Similarly, Pawlowski et al. [52] have demonstrated that the drier fibres can be obtained if the voltage is increased because of the faster evaporation of the solvent that results. In contrast Zhao et al. [53] have verified that a lower voltage leads to a weaker electric field, which reduces the acceleration of the jet and increases the flight time of the electrospinning jet, thus producing thinner fibres. Therefore, Zhao et al. [53] indicated that a voltage close to the minimum critical voltage required for the onset of electrospinning might be effective for obtaining thinner fibres.

Higher voltages are related to a greater likelihood of bead formation, possibly because of the increased instability of the jet as the Taylor cone recedes into the syringe needle with the increased voltage. The shape of the beads transforms from a spindle to a spherical shape with increased voltage, and sometimes the beads will join to form thicker fibres due to the increased density of the beads [54-

56]. On the other hand, Jarusuwannapoom et al. have reported that there should be less bead formation due to increased stretching of the solution jet at higher voltages [57]. The literature also includes studies that show that a high voltage affects both the physical appearance and crystallinity of the polymer fibres [1].

### 2.2.2 Electrode Arrangement

An alternative means to change the electric field between the needle tip and the target is to use different electrode arrangements. In the early stages of electrospinning, researchers used a needle and a flat collector plate as electrodes, as are illustrated in Fig. 1.4. However, with the development of electrospinning technology, many electrode arrangements have been tested as a means of changing the electric field and obtaining desired nanofibre morphologies.

Collector electrode arrangements such as parallel collecting electrodes; a rotating wire drum collector; a drum collector with a wire wound, rotating tube collector with knife-edge electrodes; a spinneret with a knife-edge blade; and a disc collector have all been investigated as ways to produce highly aligned fibres [26]. Similarly, electrode schemes such as an array of counter electrodes, a rotating drum with a sharp pin inside, a blade placed in line, ring collectors placed in parallel, and a yarn-collection mechanism that uses a water bath have all been tried with a goal of fabricating yarn from the fibres [26]. Multiple spinneret assemblies have also been used to mix fibres of different materials in desired ratios. In addition, as shown in Fig. 2.2, guard electrode arrangements have been tested as a means of controlling the electric field between the spinneret and the collecting plate. A comprehensive review of electrode designs that have been used for electrospinning can be found in [26].

Although many researchers have used single-needle systems for electrospinning, the low fluid throughput in spinning has limited the industrial use of single-needle systems. To meet the high liquid throughput requirements, several multi-jet schemes have recently been tested. Theron et al. presented a model using which, under comparable conditions, nine jets could be electrospun steadily from separate nozzles located with a pitch of 10 mm on a 400 $mm^2$ square [38]. Yarin et al. have provided a new approach that employs a ferromagnetic liquid sub- layer that yields about 26 jets/$cm^2$ in the upward direction. However, the process must operate at a much higher voltage, about 32kV, and the fibre diameter ranged from 200 nm to 800 nm [40]. Similarly, Yang et al. have reported that spinning with different heights of needles is more stable than spinning with a ring arrangement, and that the stable spinning voltage is higher for the ring system than for the one that has needles of different heights [39]. Reference [38] used numerical simulations to investigate the behaviour of jets in multi-jet electrospinning processes; the results showed that the mutual Coulombic interactions influence the

paths of individual electrified jets in electrospinning. Dosunmu et al. presented a device for electrospinning multiple jets from a cylindrical porous tube [44]. They also reported that a porous tube has a significantly greater production rate than a single-needle system.

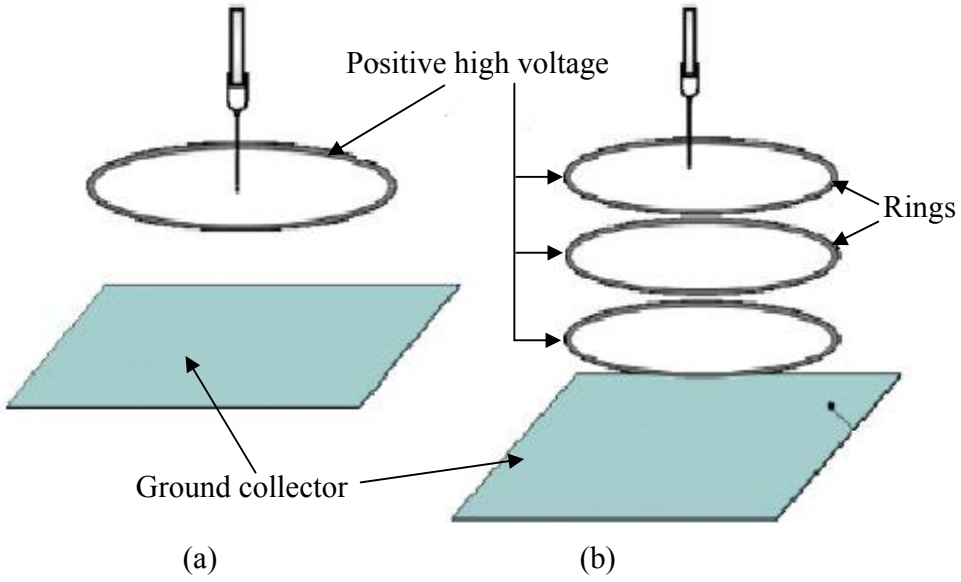


Fig 2.2: Arrangements for controlling fibre deposition area using rings as guard electrodes. (a) a single ring electrode and (b) a set of ring electrodes [38].

Despite the promising results, the above mentioned multi-needle schemes are technologically inconvenient because of the possibility of clogging. In addition, it is generally accepted that using needles for eletrospinning, which is defined as capillary spinning, leads to low productivity of nanofibres. These considerations have led to articles, such as [42] and [43], that discuss the theory of needleless electrospinning and free surface electrospinning. Another possible solution, in principle, is to obtain self-organized, multiple, electrically driven jettings from planar and cylindrical surfaces through the application of very high electric fields. Recent experimental and theoretical work has been undertaken in order to enhance the fibre production rate to an industrial scale through free surface electrospinning using both Newtonian and viscoelastic polymeric liquids. For example, a recent article [40] presented a needleless approach to the mass production of nanofibres using the combined effects of magnetic and electric fields acting on a magnetic fluid and layers of polymer solution. Jirsak et al. studied a device known as a Nanospider$^{TM}$, which is based on a rotating-cylinder solution-feeding system capable of producing nanofibres at an effective rate [45]. More recently, Lin et al. designed an electrospinning disc setup, in which a rotating disc replaces the cylinder in the Nanospider$^{TM}$ [46].

In most electrospinning schemes, the collector plate is made of conductive materials such as aluminium or copper, which are electrically grounded in order to produce an inherent stable potential difference between the two electrodes. When a non-conducting material is used as a collector, charges on the electrospinning jet quickly accumulate on the collector plate, which results in fewer fibres being deposited. This effect is caused by the increased repulsive forces of the accumulated charges on the target as more fibres are deposited than on a conductive collector plate [58].

### 2.2.3 Electrode Gap

The resultant electric field between the needle tip and the target as well as the flying time of the nanofibre can also be altered by adjusting the electrode gap distances. Varying the distance between the needle and the target causes a change in the behaviour of the electrospun jet and the morphology of the resultant nanofibres. The desired nanofibres can be collected if a reasonable time is allowed for the evaporation of most of the solvents. Shortening the distance between the two electrodes causes an increase in the electric field strength between the needle and the target and accelerates the electrospinning process, thus reducing the time available for evaporation. Therefore, when the distance between the needle tip and the target is decreased, the resultant fibres may merge to become an interconnected fibre mesh due to the presence of excess solvents, as shown in Fig. 2.3 [59].

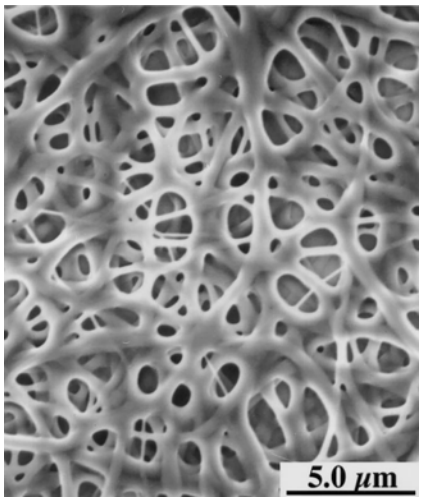


Fig. 2.3: Interconnected nanofibres collected using a shorter gap distance.

The increase in the electric field caused by shorter distances also results in beaded fibres and resultant jet instability [50, 51, and 57]. The average diameter of the fibre and the average jet current can both be decreased if the distance between the needle tip and the collector is increased since the

flying time is also increased, thus allowing enough time for the jet to elongate and become thin [1, 53, 60-62]. It has been also reported that the distribution of the diameter of the nanofibres becomes narrower when the distance between the two electrodes is increased [55]. Conversely, in other cases, it was observed that the average diameter of the fibre increases with increased distances due to the decreased strength of the electric field [50]. In addition, Zhao et al. [53] have observed that ethyl-cyanoethyl-cellulose/tetrahydrofuran solutions cannot be electrospun if the distance between the needle tip and the target is greater than 250 mm even with very high voltages [53, 55].

### 2.2.4 Flow Rate

The flow rate determines the amount of solution available for electrospinning. Maintaining a stable Taylor cone requires a minimum solution flow rate for a given voltage and electrode gap [1, 60]. At low flow rates, the Taylor cone recedes into the needle, and the jet originates from the liquid surface within the needle. In contrast, if the solution flow rate is greater than the electrospinning rate, it causes solution droplets to fall from the needle tip because of lack of time for electrospinning the complete droplet to be electrospun. It has been observed that the diameter of the fibre and the size of the bead both increase with an increased flow rate [51, 54, and 60]. Biber et al. have observed that the average diameter of the fibres decreases by increasing the flow rate of the solution. It was also reported that the distribution of the average diameter of the nanofibres broadens with increased flow rate of the solution [63]. Zong et al. have reported that different fibre morphologies can be obtained with variations in the solution flow rate for a given electric field. Zong et al. have observed that lower solution flow rates (20 μl/min) form thinner fibres with spindle-like beads, and conversely, higher solution flow rates (75 μl/min) form comparatively thicker fibres with large beads [54]. However, a compromise must be found between the increased diameter due to the higher volume flow rate and the increase in stretching due to the corresponding increase in the charge flow rate. Drying times are longer due to the higher volume of solution drawn from the needle tip, which results in the fibres fastening together because the time available for the solvents in the deposited fibres to evaporate during electrospinning may be insufficient. Yuan et al. conducted experiments using bisphenol-A polysulfone (PSF) with solution flow rates of 0.0066 ml/min and 0.011 ml/min, and they suggested that the lower feed rate is desirable for obtaining thinner and bead free fibres because more time is available for the solvent to evaporate [62].

### 2.2.5 Needle Diameter

Although the diameter of the needle has an effect on the electrospinning process, the literature contains very few studies in this area. A smaller needle diameter was found to reduce clogging at the tip of the

needle as well as the number of beads in the collected nanofibres due to the lower exposure of the solution to the atmosphere during electrospinning [1, 37]. A similar observation was done by [64] and the possible reasons were given as the decreased surface tension at the fluid droplet and the formation of smaller Taylor cone during the electrospinning. It was also presented that the smaller diameter needles lead to little increase in the heat of fusion and the temperature of melting [64]. In addition, using smaller-diameter needles means that the diameter of the electrospun nanofibres can also be smaller. The jet flying time of the solution between the needle and the collector plate can also be increased if the needle diameter is reduced because the surface tension of the droplet is increased and the jet acceleration, decreased. However, in their experiments, Zhao et al. have observed that if the needle orifice is less than 0.5mm, it is difficult to electrospin the solution due to increased surface tension [53]. Nair et al. have observed that the rate of electrospinning significantly increases by using the needles with higher inner diameter [65]. It was also reported that the more uniform or homogeneous fibres can be obtained using needles with larger diameter [63, 65]. Macossay et al. have electrospun polymethymethacrylate using different diameter needles and have observed that there is no correlation between the average fibre diameter and the diameter of the needle [66].

## 2.3 Intrinsic Properties of the Polymer Solution

The properties of the polymer solution depend not only on the nature of the components used, which includes the chemical composition of the polymer and the solvent, the corresponding molecular weight and its distribution, but also on the properties of the polymer solution, such as concentration, surface tension, viscosity, permittivity, and solution conductivity [19]. According to the literature, the properties of the polymer solution greatly influence both the electrospinning process and the resultant fibre morphology.

### 2.3.1 Viscosity

One of the most significant parameters that influence the diameter and morphology of the fibre is the viscosity of the solution, which is indirectly affected by polymer characteristics such as molecular weight and concentration. Generally, when a polymer with a higher molecular weight is dissolved in a solvent, the viscosity of the polymer solution is higher than that of a solution of the same polymer that has a lower molecular weight. Similarly, the viscosity of a polymer solution increases with an increased concentration of polymer in that solution.

It is obvious that the viscosity of the solution and the polymer chain entanglements have a direct relationship [1]. If the viscosity of the solution is high, then the polymer chain entanglements are also

high, and vice versa. Polymer chain entanglements have been found to have a significant impact on whether the jet breaks up into small droplets and on whether the resultant electrospun fibres contain beads [67]. In the electrospinning process, for fibre to be formed a minimum amount of polymer chain entanglement, i.e, viscosity, is required. On the other hand, if the viscosity is too high, then either

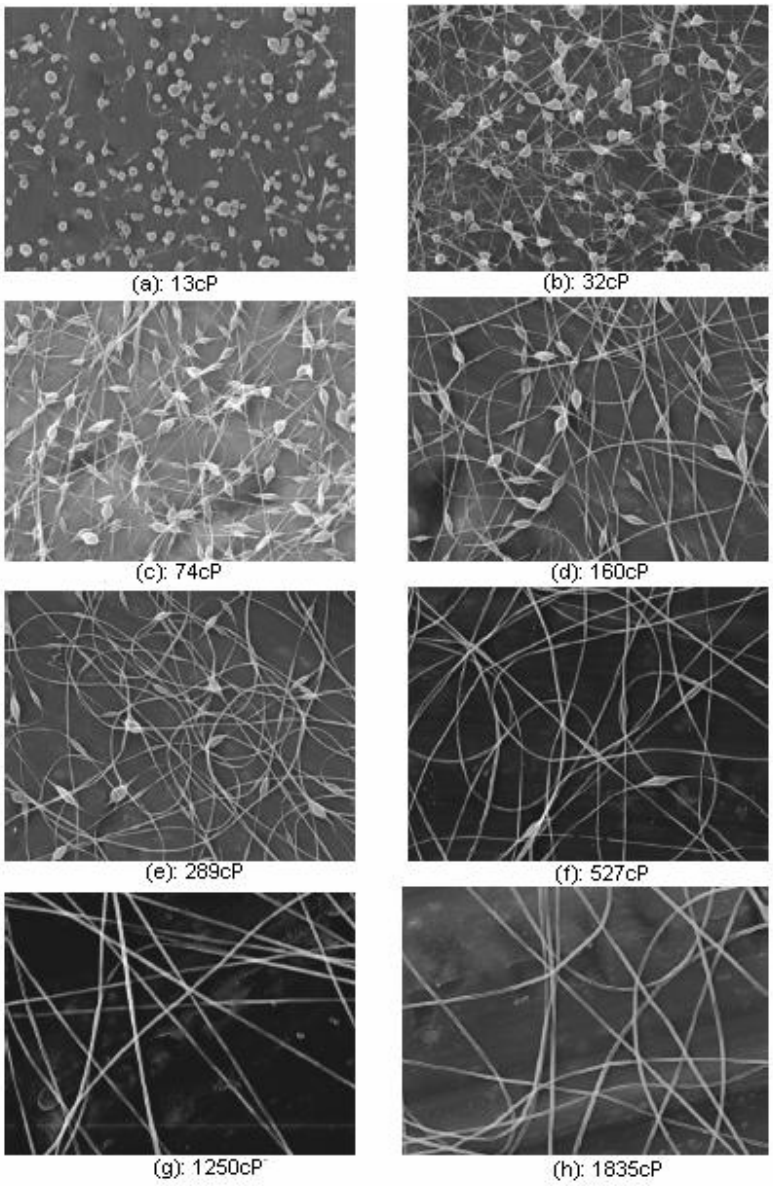


Fig. 2.4: Morphology of beaded fibres with increased solution viscosity [68].

pumping the solution through the syringe pump becomes very difficult, or the solution may dry at the tip of the needle before electrospinning is initiated [41, 54].

Fig. 2.4 shows images of bead formation in electrospun nanofibres. Beads and beaded fibres are less likely to be formed with more viscous solutions. The shape of the beads changes from spherical to elliptical when the viscosity of the solution varies from low to high values. Higher viscosity also results in larger diameter fibres and smaller deposition areas. A list of articles that describe the variations that occur in fibre morphology when the viscosity of the solution is varied can be found in [1].

### 2.3.2 Surface Tension

Surface tension is caused by the attraction between the molecules in a liquid, which is created by a number of intermolecular forces. In the bulk of the liquid, each molecule is pulled equally in all directions by neighbouring liquid molecules, resulting in a net force of zero. At the surface of the liquid, the molecules are subjected to a net inward force that is balanced only by the resistance of the liquid to compression. The net effect causes the surface area to diminish until it possesses the lowest ratio possible of surface area to volume.

In electrospinning, the charges on the polymer solution must be high enough to overcome the surface tension of the solution. As the electrospun jet accelerates from the tip of the needle to the target, the polymer jet is stretched, and the surface tension of the solution may cause the jet to break up into droplets, resulting in spraying which is called electrospraying [69]. In addition, if there is a lower concentration of polymer molecules, the surface tension causes beaded fibres to form [54]. A lower surface tension in the spinning solution also helps the electrospinning jet to initiate at a lower electric field.

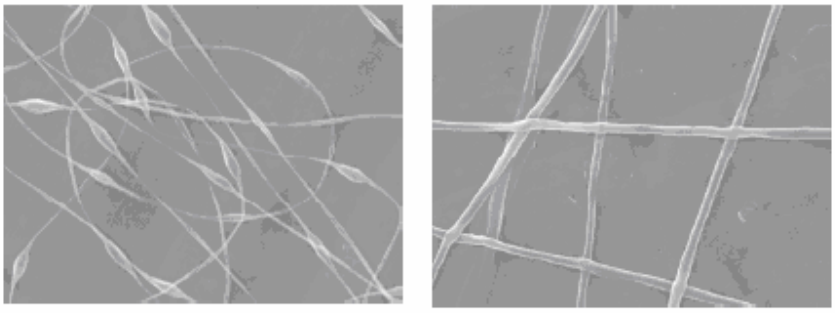


Fig. 2.5: Variation in beaded fibres with the use of different solvents: (a) distilled water and (b) mixture of distilled water and ethanol [68].

The surface tension of a solution is a function of the type and composition of the solvent. Different solvents may thus contribute differently to alterations in the surface tension [1, 48, 54]. Adding a

surfactant to the polymer solution also changes the surface tension. Generally, if all other variables are held constant, surface tension determines the upper and lower boundaries of the electrospinning process. Fig. 2.5 shows the nanofibres electrospun from a PEO/water/ethanol solution with an identical PEO-to-solvent w/w concentration.

### 2.3.3 Conductivity

The repulsion of the charges at the surface of the electrospinning jet causes the solution to stretch and form the nanofibres. A significant reduction in the diameter of the electrospun nanofibres can therefore be observed when the electrical conductivity of the solution is increased because the jet carries more charges. The formation of beaded fibres can be avoided if a small amount of salt or polyelectrolyte is added to the polymer solution because the electrical forces of the increased charge carried by the electrospinning jet cause the jet to elongate, and uniform fibres are produced. However, if the conductivity of the solution is too high, it is very difficult or impossible to spin the fibres even with very high voltages. Similarly, it is also impossible to form fibres if the solution has zero conductivity [57].

Kim et al. [70] have observed this behaviour of the fibre diameter decreasing when the conductivity of a poly (2-acrylamido-2-methyl-1-propane sulfonic acid) solution is increased. In general, electrospun nanofibres with the smallest fibre diameter can be obtained using the highest conductivity of the solution [54]. The minimum voltage for electrospinning to occur can also be reduced if the conductivity of the polymer solution is increased [71]. Additionally, a higher solution conductivity, i.e, an increased charge concentration, results in greater bending instability and creates a larger deposition area of collected fibres [72].

It has been reported as well that the size of the ions in the solution has a significant impact on the electrospun fiber diameter in addition to the amount of charges carried by the jet. Ions with a smaller atomic radius have a higher charge density and thus, a higher mobility under an external electric field [54, 72]. In [73], a novel method on producing bead free ultra fine electrospun fibers with narrow fiber diameter distribution from Poly(3-caprolactone) has been described. The authors have achieved high quality fibers by increasing the conductivity of the polymer solution with the use of a new solvent system that involved an acid base reaction to produce weak salt complexes. But, Stanger et. al [74] found that an increase in charge density results in a decrease in the mass deposition rate and initial jet diameter during the electrospinning. In addition, a theory was proposed where they correlated the reduction of the diameter of the curvature of Taylor cone with the increase in charge density and hence, the decrease of total electrostatic forces due to the smaller effective area [74]. Similarly, other

researchers have reported that the different behavior of the Taylor cone with compared to the Taylor's observation of ionic liquids [75-77].

The use of bio-degradable polymers has been significantly increased in the recent past to minimize the environmental damage caused by the synthetic polymers. Therefore, there is a growing market for electrospun nanofibres using natural polymers with many potential applications in the areas of food, medical, and pharmaceutical fields [1]. Thus, many natural polymers such as cellulose acetate, chitin, chitosan, alginate, collagen, gelatin, and silk have been tried to electrospin by researches worldwide [1, 54]. However, most of the times, they have used a carrier synthetic polymer to electrospin natural bio-polymers, because of their extensive polyelectrolyte behavior [1, 18, 72, 78, and 79]. Similarly, some researches have tried to electrospin conductive polymers to make highly efficient semiconductor devices such as Schottky nanodiodes. For example, Pinto et. al. have experimented electrospinning polyaniline which is a conductive polymer; however, they have only succeeded electrospinning polyaniline by making a polymer blend, mixing with polyethylene oxide (PEO) [80, 81]. In addition, to authors' knowledge, electrospinning highly insulating materials such as silicone rubber has not been carried out to-date.

### 2.3.4 Permittivity

As with conductivity, the permittivity of a solvent has a significant influence on the electrospinning process and fibre morphology. However, not much discussion has been published about these effects. Theron et al. describe a method for determining the permittivity of an electrospinning solution by measuring the complex impedance of a small cylindrical volume of the fluid [82]. Bead formation and the diameter of the resultant electrospun fibres can be decreased by using a solution with a higher permittivity. The bending instability and the traversed jet path of the electrospinning jet increase with higher permittivity, which results in a reduction in the diameter of the fibre and a larger fibre deposition area. Solvents such as N,N-Dimethylformamide (DMF) can be used to increase the permittivity of polymer solutions [61, 83].

## 2.4 Ambient Parameters

The interaction between the surrounding environment and the electrospinning jet may affect the electrospinning process and fibre morphology. However, few studies have examined this area.

### 2.4.1 Temperature

Very little research has examined the effect of temperature on the electrospinning process and on the fibre morphology. Increases in temperature cause the evaporation rate to increase and the viscosity of the solution to decrease. Using polyurethane at a higher temperature, Demir et al. [55] have been able to produce electrospun fibres that are more uniform. Their results may be due to the lower viscosity of the polymer solution at higher temperatures [55].

Similarly, Vrieze et al. have investigated the effects of temperature on electrospinning and have observed that the evaporation rate of the solvent decreases exponentially with decreasing temperature resulting thinner fibres [84]. It was also reported that the increasing temperature lowers the viscosity of the solution thus, producing higher stretching rate and thinner fibres [84]. The increased mobility of polymer molecules at higher temperatures also allows the columbic force to stretch the electrospun jet further [1]. Conversely, when biological substances such as enzymes and proteins are used for electrospinning, high temperatures may cause them to lose their functionality [1]. Wang et al. have observed that a larger voltage is required to start the electrospinning at high temperatures with compared to the room temperature due to the formation of a larger Taylor cone at the needle tip [84, 85]. Their results using polyacrylonitrile were also shown that the electrospinning at higher temperatures possess the advantages of producing fibres with a smaller diameter, lower order of crystalline, and a higher orientation of chain [85].

### 2.4.2 Humidity

The humidity of the electrospinning environment may have an influence on the polymer jet during electrospinning. Moisture may condense on the surface of the fibre when the process is carried out in a very humid environment [1]. The condensation may significantly influence the fibre morphology; for example, circular pores can form on the fibre surfaces especially when polymers dissolved in volatile solvents are used [86]. Casper et al. have reported that the size and depth of the circular pores increase with increasing humidity until they unite to form large, irregular structures [86]. Solutions with higher molecular weights cause the fibres to contain larger pores that are less uniform in shape and size. However, the presence of humidity does not influence the shape or diameter of the fibre [86]. The level of humidity also determines the rate at which the solvent in the polymer solution evaporates: a volatile solvent may dry rapidly if the humidity is low [1]. It has also been suggested that high humidity can help somewhat to discharge the charged particles in the electrospun jet [1, 87].

Different gases exhibit different behaviour in the electrostatic field. The composition of the air in an enclosed electrospinning chamber may therefore affect the electrospinning process and fibre

morphology [1]. Similarly, atmospheric pressure also influences the electrospinning process, and its effect on the electrospinning jet could be investigated under enclosed conditions. In general, a reduction in the surrounding pressure has a detrimental effect on the electrospinning process because it leads to unstable jet initiation, fast bubbling of the solution at the needle tip, and direct discharges of the electrically charged solution [1].

# Chapter 3
# Theoretical Modeling

## 3.1 Introduction

The basic principles for dealing with electrified fluids were published in a series of papers by Taylor in the early 1960s [12, 13]. His ideas later became known as the *leaky dielectric model.* With the advancement of nanotechnology and the popularity of the electrospinning process, several other mathematical models were developed in order to describe the behaviour of the electrospun jet. More recently, electrospinning models have been created so that the electrospinning process could be approximately analyzed based on the parameters that govern the process. As shown in Fig. 3.1, the electrospinning process consists of three stages that correspond to the behaviour of the electrospun jet: the formation of the Taylor cone, the ejection of the straight jet, and the unstable whipping jet region. Based on these stages, an electrospinning model can therefore be divided into three major sections [1]:

1. Modeling the criteria for jet initiation from the droplet
2. Modeling the straight jet portion
3. Modeling the entire jet

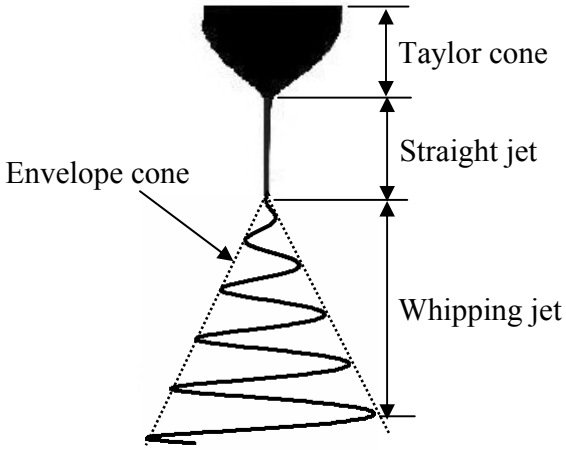


Fig. 3.1: Behaviour of the electrospun jet.

## 3.2 Modeling the Criteria for Jet Initiation

In 1882, Rayleigh conducted a theoretical study of the stability of an isolated charged liquid droplet and predicted that it becomes unstable when the charge is sufficiently large compared to the stabilizing effect of the surface tension. Zeleny tried to adapt this theory to the case of an electrified droplet and

observed that the droplet loses its stability and a liquid jet is initiated at its vertex with the increase of an applied voltage [10]. Taylor carried out a similar type of work using a soap solution and determined the critical voltage that causes the stability of the droplet to deteriorate and the liquid jet to initialize [12]. He also studied the shape of the droplet during the initiation of the jet and verified that the shape is transformed from semi spherical to conical [12]. Fig. 3.2 shows the step-by-step initiation of the jet and the transformation of the droplet shape, as studied by Taylor.

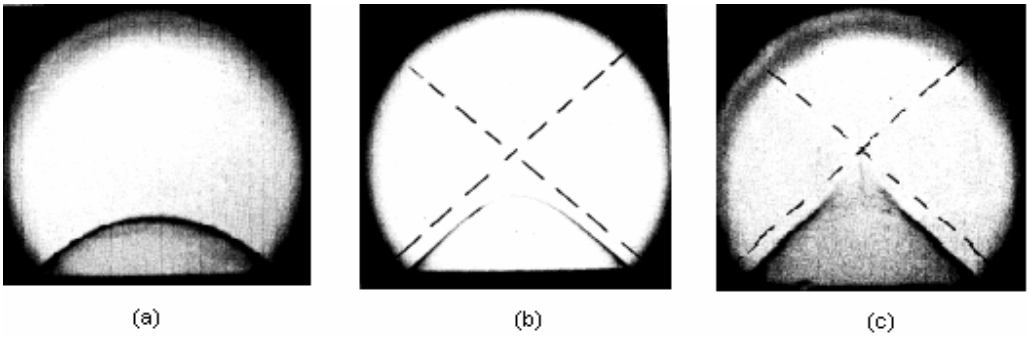


Fig. 3.2: Liquid jet initiation and Taylor cone formation of an electrified droplet: (a) Before instability; (b) Beginning of instability; (c) Jet formation stage [12].

Hartman et al. developed a physical model for calculating the shape of the liquid cone and jet, the electric fields inside and outside of the cone, and the density of the surface charge on surface of the liquid. A one-dimensional momentum equation was used for simulating the flow field in the model [88]. Yan et al. [89] improved this model further by introducing a cone-jet model coupled with an axi-symmetric flow field, and they solved both the hydrodynamic and electrostatic equations using an adaptive grid generation scheme, which is essential for updating the cone-jet shape. They were able to calculate both the cone-jet shape and the velocity field within the meniscus [89]. Subsequently, Yarin et al. [90] introduced an additional shape, one tending towards a sharper cone than Taylor's, that can precede the stability failure and the onset of jetting. The idea was theoretically formulated and experimentally verified using a sessile droplet [90].

## 3.3 Modeling the Straight Jet Portion

The analytical relationship between the radius $r$ of the jet and the axial distance $z$ from the needle tip have been the subject of regular investigation since the electrospinning process was first patented by Formhals in 1934. Spivak et al. developed a general electrohydrodynamic model of a weakly conductive viscous jet accelerated by an external electric field, which took into account the inertial, hydrostatic, viscous, electric, and surface tension forces. A nonlinear rheological constitutive equation,

named the Oswald-deWaele law, was used to describe the polymer solution. A one-dimensional differential equation for the jet radius (equation (3.1)) was derived, and this type of mathematical model can be used to provide better control and optimization of the electrospinning process.

$$\frac{d}{dz}\left\{R^{-4}+WeR^{-1}-\mathrm{Y}R^{2}-\frac{1}{\mathrm{Re}}\left[\frac{1}{2}\frac{d}{dz}\left(R^{-2}\right)\right]^{m}\right\}=1 \tag{3.1}$$

The notations can be found in Appendix B [91].

Ji-Huan et al. predicted the critical length of the straight jet portion of the electrospun jet from the needle point to the point where instability occurs [92]. The well-known Chauchy's inequality, provided in Appendix B, was used to determine the critical length of the straight jet portion of the electrospun jet, and it was recommended as being much more effective and convenient than any other conventional approaches, such as numerical and experimental [92].

## 3.4 Modeling the Entire Jet

After traveling linearly for a specific position of its path, the ejected liquid jet usually becomes unstable with respect to jet propagation because the solvent is continuously evaporating, and the diameter is thinned because of the stretching. To the naked eye, this instability appears as splaying in the form of repeated bifurcations from the initial single jet into multiple jet streams. However, subsequent experimental evidence gathered from high-speed cameras and theoretical models suggests that the apparent splaying is an optical illusion produced by very fast whipping motion of the jet. In a major study conducted by Hohman et al., they developed a theoretical framework for understanding the physical mechanisms of electrospinning and proposed a method of quantitatively predicting the parameter regimes where the electrospinning occurs [93]. The theory consists of two basic components: a stability analysis of a cylinder of fluid with a static charge density in an external electric field and a theory about how the properties of solution vary along the jet as it thins away from the nozzle [93]. By analyzing the various instabilities in the jet, they were able to make predictions about the onset of electrospinning that quantitatively agree with experimental results.

The complete set of dimensionless equations that govern the electrospun jet are as follows. The notations are provided in Appendix C [93].

1. Conservation of mass

$$\frac{\partial\left(h^{2}\right)}{\partial t}+\frac{\partial\left(h^{2}v\right)}{\partial z}=0 \tag{3.3}$$

2. Conservation of charge

$$\frac{\partial(\sigma h)}{\partial t}+\frac{\partial}{\partial z}\left(\sigma h v+\frac{K^{*}}{2}h^{2}E\right)=0 \tag{3.4}$$

3. Conservation of momentum

$$\frac{\partial v}{\partial t}+v\frac{\partial v}{\partial z}=-\frac{\partial}{\partial z}\left(\frac{1}{h}-\frac{\partial^{2}h}{\partial z^{2}}-\frac{E^{2}}{8\pi}-2\pi\sigma^{2}\right)+\frac{2\sigma E}{\sqrt{\beta}h}+g^{*}+\frac{3\upsilon^{*}}{h^{2}}\frac{\partial}{\partial z}\left(h^{2}\frac{\partial v}{\partial z}\right) \tag{3.5}$$

4. Coulomb's integral for the electric field

$$E-\ln\frac{1}{\chi}\left[\frac{\beta}{2}\frac{\partial^{2}\left(h^{2}E\right)}{\partial z^{2}}-4\pi\sqrt{\beta}\frac{\partial(h\sigma)}{\partial z}\right]=\Omega_{0} \tag{3.6}$$

Feng et al. simplified the above model by eliminating the ballooning instability of the electric field calculation. The simplified model was tested by comparing its predictions with the experimental data for a variety of boundary conditions and parameter values, such as the electric Peclet number, the Froude number, the Reynolds number, and the Weber number. Non-Newtonian rheology was also introduced into the theoretical model of electrospinning, and the effects of extension thinning, extension thickening, and strain hardening of the polymer solution were examined [94].

### 3.4.1 Discrete Model of the Entire Jet

Reneker et al. contributed significantly to the modeling of electrospinning by developing a discrete three-dimensional model to describe the dynamics of electrospinning [18]. Their proposed model for electrospinning is summarized in this section.

First, a rectilinear electrified liquid jet in an electric field parallel to its axis is considered. A segment of the jet is modeled using a Maxwellian viscoelastic element, which consists two types of elements: *dashpot*, which describes the forces as being in proportion to the velocity, and *spring,* which describes the forces as being in proportion to the elongation, as shown in Fig. 3.3 (a) [18].

The entire electrospun jet is represented by a modeled system of beads that have a charge *e* and a mass *m* and that are connected by viscoelastic Maxwellian elements, as illustrated in Fig. 3.3 (b). The parameters that correspond to the elements connecting bead *i* and bead *i+1* are denoted by subscript *u*, and those that correspond to the elements connecting bead *i* and bead *i-1*, by subscript *d*. The symbols used in following equations and their definitions are listed in Table 3.1. The lengths $l_{ui}$ and $l_{di}$ of these elements are given by

$$l_{ui} = [(x_{i+1} - x_i)^2 + (y_{i+1} - y_i)^2 + (z_{i+1} - z_i)^2]^{1/2} \tag{3.7}$$

$$l_{di} = [(x_i - x_{i-1})^2 + (y_i - y_{i-1})^2 + (z_i - z_{i-1})^2]^{1/2} \tag{3.8}$$

where $x_i, y_i,$ and $z_i$ are the Cartesian coordinates of the beads. The viscoelastic forces acting along the elements are given by

$$\frac{d\sigma_{ui}}{dt} = G\frac{1}{l_{ui}}\frac{dl_{ui}}{dt} - \frac{G}{\mu}\sigma_{ui} \tag{3.9}$$

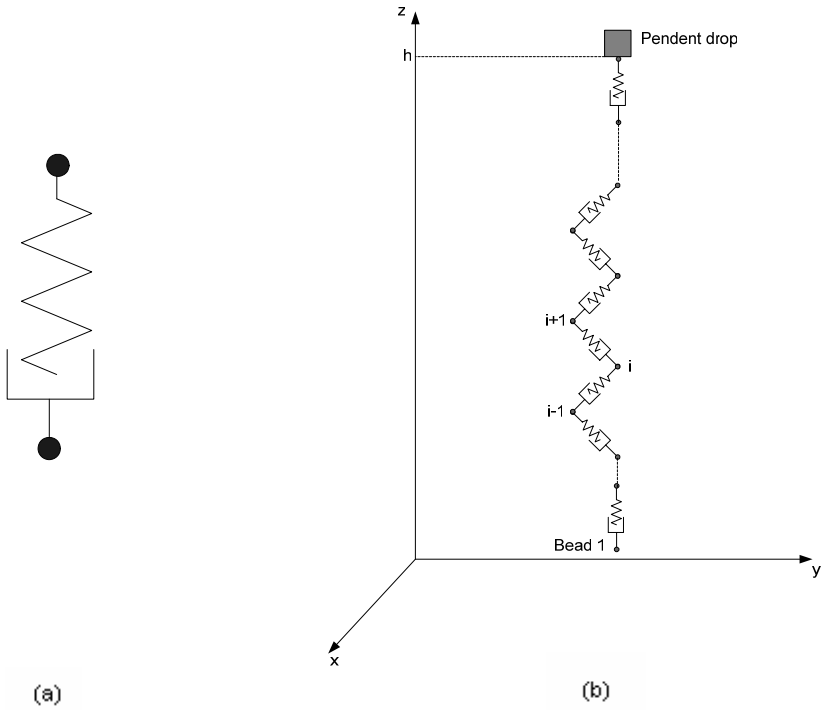


Fig. 3.3: (a) Maxwellian viscoelastic element; (b) Bending electrospun jet modeled using a system of beads connected by viscoelastic maxwellian elements [18].

$$\frac{d\sigma_{di}}{dt} = G\frac{1}{l_{di}}\frac{dl_{di}}{dt} - \frac{G}{\mu}\sigma_{di} \tag{3.10}$$

The total number of beads *N* increases over time, and the net Coulomb force acting on the $i^{th}$ bead from all other beads is given by

$$f_c = \sum_{\substack{j=1 \\ i \neq j}}^{N} \frac{e^2}{R_{ij}^2}\left[\left(\frac{x_i - x_j}{R_{ij}}\right)\underline{i} + \left(\frac{y_i - y_j}{R_{ij}}\right)\underline{j} + \left(\frac{z_i - z_j}{R_{ij}}\right)\underline{k}\right] \tag{3.11}$$

where $\underline{i}, \underline{j}$, and $\underline{k}$ are the unit vectors along the $x, y$, and $z$ axes, respectively. The distance $R_{ij}$ is calculated by

$$R_{ij} = [(x_i - x_j)^2 + (y_i - y_j)^2 + (z_i - z_j)^2]^{1/2} \tag{3.12}$$

The electric force imposed on the $i^{th}$ bead by the electric field, which is created due to the applied potential difference between the needle tip and the collector plate, is given by

$$f_e = -e\frac{V_0}{h}\underline{k} \tag{3.13}$$

Table 3.1: Symbols and their definitions.

| Symbol | Definition | Unit |
|---|---|---|
| $a_0$ | Initial cross-section radius | mm |
| $a$ | Cross-section radius of the jet | mm |
| $e$ | Charge of the bead | $(g^{1/2}mm^{3/2})/s$ |
| $G$ | Elastic modulus | $g/(mms^2)$ |
| $h$ | Distance from the needle tip to the target | mm |
| $k$ | Jet curvature | $mm^{-1}$ |
| $L$ | Length scale = $(e^2/\pi a_0^2 G)^{1/2}$ | mm |
| $l$ | Length of the ideal rectilinear jet | mm |
| $m$ | Mass of the bead | g |
| $t$ | Time | s |
| $V_0$ | Applied voltage | $g^{1/2}mm^{1/2}/s$ |
| $\alpha$ | Surface tension coefficient | $g/s^2$ |
| $\rho$ | Fluid density | $g/mm^3$ |
| $\mu$ | Solution viscosity | g/mm/s |
| $\sigma$ | Stress | $g/(mms^2)$ |
| $\omega$ | Perturbation frequency | $s^{-1}$ |

The net viscoelastic force acting on the $i^{th}$ bead of the jet is given by

$$f_{ve} = \pi a_{ui}^2 \sigma_{ui} \left[ \left( \frac{x_{i+1} - x_i}{l_{ui}} \right) \underline{i} + \left( \frac{y_{i+1} - y_i}{l_{ui}} \right) \underline{j} + \left( \frac{z_{i+1} - z_i}{l_{ui}} \right) \underline{k} \right] - \pi a_{di}^2 \sigma_{di} \left[ \left( \frac{x_i - x_{i-1}}{l_{di}} \right) \underline{i} + \left( \frac{y_i - y_{i-1}}{l_{di}} \right) \underline{j} + \left( \frac{z_i - z_{i-1}}{l_{di}} \right) \underline{k} \right] \tag{3.14}$$

When the mass is conserved and evaporation is neglected, the rectilinear filament radii $a_{ui}$ and $a_{di}$ are given by

$$\pi a_{ui}^2 l_{ui} = \pi a_0^2 L \tag{3.15}$$

$$\pi a_{di}^2 l_{di} = \pi a_0^2 L \tag{3.16}$$

The surface tension force acting on the $i^{th}$ bead and tending to restore the rectilinear shape of the bending part of the jet is given by

$$f_{st} = -\frac{\alpha \pi (a^2)_{av} k_i}{\left(x_i^2 + y_i^2\right)^{1/2}} \left[ \lfloor x_i \rfloor sign(x_i) \underline{i} + \lfloor y_i \rfloor sign(y_i) \underline{j} \right] \tag{3.17}$$

where $\alpha$ is the surface tension coefficient; $k_i$ is the jet curvature calculated using the coordinates of beads *i-1*, *i*, and *i+1*; and $(a^2)_{av} = (a_{ui} + a_{di})^2 / 4$. The *sign* can be defined as

$$\begin{aligned} sign(x) &= 1, \quad if \rightarrow x > 0 \\ sign(x) &= -1, \quad if \rightarrow x < 0 \\ sign(x) &= 0, \quad if \rightarrow x = 0 \end{aligned} \tag{3.18}$$

The equation governing the radius vector of the position of the $i^{th}$ bead, $\underline{r} = x\underline{i} + y\underline{j} + z\underline{k}$, can be formulated in the following form based on Newton's second law and the forces described in equations (3.11), (3.13), (3.14), and (3.17):

$$m \frac{d^2 \underline{r_i}}{dt^2} = \sum_{\substack{j=1 \\ i \neq j}}^{N} \frac{e^2}{R_{ij}^3} (\underline{r_i} - \underline{r_j}) - e \frac{V_0}{h} \underline{k} + \frac{\pi a_{ui}^2 \sigma_{ui}}{l_{ui}} (\underline{r_{i+1}} - \underline{r_i}) - \frac{\pi a_{di}^2 \sigma_{di}}{l_{di}} (\underline{r_i} - \underline{r_{i-1}}) - \frac{\alpha \pi (a^2)_{av} k_i}{\left(x_i^2 + y_i^2\right)^{1/2}} \times \left[ \lfloor x_i \rfloor sign(x_i) \underline{i} + \lfloor y_i \rfloor sign(y_i) \underline{j} \right] \tag{3.19}$$

For the first bead, i=1, and N, the total number of beads is also 1. As more and more beads are added, N becomes larger and the first bead i=1 remains at the bottom end of the growing electrospinning jet. For this bead, all the parameters with subscript d should be set equal to zero since there are no beads below i=1 [18].

Both space- and time-dependent perturbations lead to the development of electrically driven bending instability. The developing spatial perturbation can be modeled as the last bead; *N* that is pulled out from the needle tip is added at the upper end of the jet. When the distance $l_{d,N}$ between this bead and the needle tip becomes long enough, a new bead *i=N+1* is inserted at a small distance from the previous bead. A small perturbation is added to its *x* and *y* coordinates at the same time, as given in the following equations:

$$x_i = 10^{-3} L \sin(\omega t) \tag{3.20}$$

$$y = 10^{-3} L \cos(\omega t) \tag{3.21}$$

Here, $\omega$ is the perturbation frequency. All the equations are made dimensionless before the calculation. The condition that the impenetrable target at *z=0* is enforced numerically, and the charge on each element of the jet is removed as soon as it arrives at the target. This calculation closely simulates the development of the electrically driven bending instability, as shown in Fig. 3.4. The calculation begins with only two beads, *N=2*, and as the jet flows, the number of beads in the jet, *N*, increases.

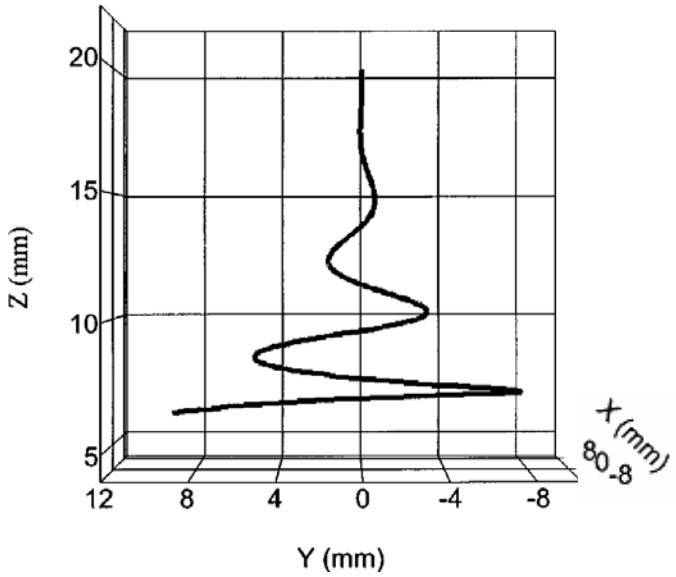


Fig. 3.4: Three-dimensional simulation of the bending instability of the electrospun jet.

Yarin et al. later introduced a localized approximation with an appropriate cutoff of the integral in

order to calculate the bending electric force, whereas in Reneker's model, the whole integral is accounted in the calculation of the bending electric force in the discrete form. In addition, the effects of the evaporation of the solvent and the solidification of the electrospun polymer jet were also added to the model [95]. As a result, a more accurate model could be achieved for comparing quantitative analysis with the actual electrospun jet. However, it is very difficult to use experimental data for validating the correctness of the above physical model of electrospinning because of the difficulties involved in estimating correct values for the basic parameters necessary for modeling, such as the charge density, the electric field geometry, the mass and charge flow rates, variations in fluid parameters, and the initial conditions [96]. The model should therefore be fine tuned so that the input parameters can be matched to experimental observations.

### 3.4.2 Improved Discrete Model of the Entire Jet

Similar to the discrete electrospinning model that is discussed in Section 3.4.1, a rectilinear electrified liquid jet is modeled using a Maxwellian viscoelastic element as shown in Fig. 3.5. The Maxwell model satisfactorily represents the rheological behavior of concentrated polymeric systems in strong uniaxial elongation, which is the case of electrospinning [18]. The beads A and B in Fig. 3.5 possess a charge $e$ and mass $m$. Bead A is assumed to be fixed by non-Coulomb forces. Therefore, the stress $\sigma$ of the Maxwellian viscoelastic element is given by

$$\frac{d\sigma}{dt} = G\frac{1}{l}\frac{dl}{dt} - \frac{G}{\mu}\sigma \tag{3.22}$$

The momentum balance for bead B is given by

$$m\frac{dv}{dt} = -\frac{e^2}{l^2} - \frac{eV_0}{h} + \pi a^2\sigma \tag{3.23}$$

Where, $\left(-\frac{e^2}{l^2}\right)$ and $\left(-\frac{eV_0}{h}\right)$ are the Coulomb repulsive force and the force due to the external electric field (considering parallel plane electrodes) acting on bead B respectively.

The velocity of bead B is calculated by

$$\frac{dl}{dt} = -v \tag{3.24}$$

The symbols of variables used in Equations (3.22), (3.23) and (3.24) can be found in Table 3.1.

However, the force due to the external electric field $\left(-\frac{eV_0}{h}\right)$ is modified considering the actual experimental environment, especially incorporating the non-uniformity of the electric field between the

needle tip and the collector plate. The method used for calculating the distribution of electric field between the needle tip and the collector plate is based on the charge simulation technique (CST) [97, 98]. As shown in Fig. 3.5, a needle of radius *R* is considered for the simulation positioning above the collector plate at spacing *h*. The Taylor cone at the tip of the needle is approximated by a hyperboloid with a radius of *r* at the tip. The Taylor cone at the tip of the needle and the needle are simulated by a point charge $q_1$ at the centre of the tip of the Taylor cone and a set of finite-line charges ($q_2$, $q_3$, ….$q_N$) on the needle shank respectively. The length of the finite-line charges is small at the tip and increases in a geometric progression along the z-direction. The concept of image charges is considered to calculate the distribution of electric field between the flat ground collector plate and the needle.

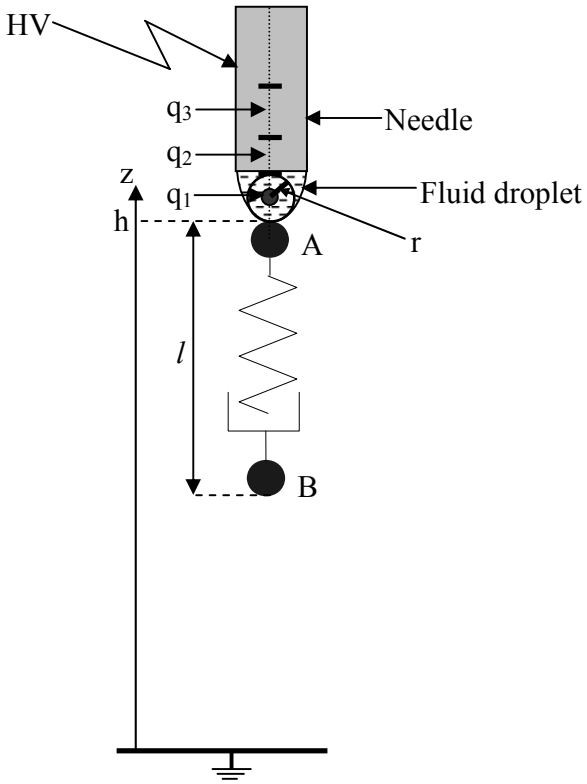


Fig. 3.5: Modeled segment of the rectilinear part of the electrospun jet.

Therefore, as shown in Equations (3.25) to (3.27), the x-, y- and z- components of the electric field at the point *P* in space are equal to the sum of the x-, y- and z-field components generated at point *P* by the charges, $q_j, j=1, 2, ..., N$ and their image charges, $q'_j$ [97].

$$E_x(P,j) = \sum_{j=1}^{N} q(j) A_x(P,j) + \sum_{j=1}^{N} q'(j) A_x(P,j) \tag{3.25}$$

$$E_y(P,j)=\sum_{j=1}^{N}q(j)A_y(P,j)+\sum_{j=1}^{N}q^{'}(j)A_y(P,j) \tag{3.26}$$

$$E_z(P,j)=\sum_{j=1}^{N}q(j)A_z(P,j)+\sum_{j=1}^{N}q^{'}(j)A_z(P,j) \tag{3.27}$$

where $A_x(P,j)$, $A_y(P,j)$, and $A_z(P,j)$ are the field coefficients in the x-, y- and z- directions. They are defined by Equations (3.28) to (3.33).

(1) Considering a point charge along the z-axis: as shown in Fig. 3.5, for a point charge $q_j$ (such as $q_1$) located at the coordinates (*0, 0,* $z_j$ ), the coefficients of the electric field at the point P ($x_P$, $y_P$, $z_P$) is defined as

$$A_x(P,j)=\frac{x_P}{4\pi\varepsilon_0\left(\sqrt{(x_P)^2+(y_P)^2+(z_P-z_j)^2}\right)^3} \tag{3.28}$$

$$A_y(P,j)=\frac{y_P}{4\pi\varepsilon_0\left(\sqrt{(x_P)^2+(y_P)^2+(z_P-z_j)^2}\right)^3} \tag{3.29}$$

$$A_z(P,j)=\frac{(z_P-z_j)}{4\pi\varepsilon_0\left(\sqrt{(x_P)^2+(y_P)^2+(z_P-z_j)^2}\right)^3} \tag{3.30}$$

(2) Considering a finite line charge along the z-axis: as shown in Fig. 3.5, for a line charge $q_j$ (such as $q_2$) positioning along the *z*-axis between the coordinates (*0, 0,* $z_{j1}$ ) and (*0, 0,* $z_{j2}$ ), then the coefficients of the electric field at the point P ($x_P$, $y_P$, $z_P$) in space is defined as

$$A_x(P,j)=-\frac{1}{4\pi\varepsilon_0(z_{j2}-z_{j1})}\frac{x_P}{\sqrt{x_p^2+y_p^2}}\times\left[\frac{(z_P-z_{j2})}{\beta_1}-\frac{(z_P-z_{j1})}{\beta_2}\right] \tag{3.31}$$

$$A_y(P,j)=-\frac{1}{4\pi\varepsilon_0(z_{j2}-z_{j1})}\frac{y_P}{\sqrt{x_p^2+y_p^2}}\times\left[\frac{(z_P-z_{j2})}{\beta_1}-\frac{(z_P-z_{j1})}{\beta_2}\right] \tag{3.32}$$

$$A_z(P,j)=-\frac{1}{4\pi\varepsilon_0(z_{j2}-z_{j1})}\times\left[-\frac{1}{\beta_1}+\frac{1}{\beta_2}\right] \tag{3.33}$$

where $\beta_1 = \sqrt{(x_p)^2 + (y_p)^2 + (z_{j2} - z_p)^2}$ and $\beta_2 = \sqrt{(x_p)^2 + (y_p)^2 + (z_{j1} - z_p)^2}$

Here, charges $q_j$, $j=1, 2,..., N$ and their image charges, $q_j^{'}$ are determined by using the boundary conditions. Thus, the Dirichlet boundary condition applied at the surface of the stressed needle is,

$$V = \sum_{j=1}^{N} q(j)B(P,j) + \sum_{j=1}^{N} q^{'}(j)B(P,j) \tag{3.34}$$

The Dirichlet boundary condition applied at the surface of the grounded collector plate is

$$0 = \sum_{j=1}^{N} q(j)B(P,j) + \sum_{j=1}^{N} q^{'}(j)B(P,j) \tag{3.35}$$

where $B(P,j)$ is the potential coefficients calculated at the P[th] boundary point due to the jth simulation charge as expressed in Equations (3.36) and (3.37)

(1) Considering a point charge along the z-axis: as shown in Fig. 3.5, for a point charge $q_j$ (such as $q_1$) located at the coordinates ($0, 0, z_j$), the coefficients of the potential at the point P ($x_P, y_P, z_P$) is defined as

$$B(P,j) = \frac{1}{4\pi\varepsilon_0\left(\sqrt{(x_P)^2 + (y_P)^2 + (z_P - z_j)^2}\right)} \tag{3.36}$$

(2) Considering a finite line charge along the z-axis: as shown in Fig. 3.5, for a line charge $q_j$ (such as $q_2$) positioning along the $z$-axis between the coordinates ($0, 0, z_{j1}$) and ($0, 0, z_{j2}$), then the coefficients of the potential at the point P ($x_P, y_P, z_P$) in space is defined as

$$A_x(P,j) = -\frac{1}{4\pi\varepsilon_0(z_{j2} - z_{j1})}\ln\left[\frac{(z_{j2} - z_P + \beta_1)}{(z_{j1} - z_P + \beta_2)}\right] \tag{3.37}$$

- The force in the $z$ direction on the $i^{th}$ bead due to the non-uniform electric field created by the potential difference between the needle tip and the target is given by,

$$f_e = -e\left[E_x(P,j)\underline{i} + E_y(P,j)\underline{j} + E_z(P,j)\underline{k}\right] \tag{3.38}$$

- A localized approximation as shown in the equation (3.39) is used to calculate the bending electric force acting on the electrospinning jet, and this is the same approximation which was exercised by Yarin *et al*. in their calculations [95].

$$\chi^* = \left[\frac{8}{9}\frac{\rho}{\mu^2}\frac{e_0^2}{\pi}\ln\left(\frac{1}{\chi^*}\right)\right]^{1/6} \tag{3.39}$$

where, $\chi^*$ can be defined as,

$$\ln\left(\frac{1}{\chi^*}\right) = \ln\left(\frac{L_{cutoff}}{a_0}\right) \tag{3.40}$$

The length $L_{cutoff}$ is the cut of length which is used for electric force calculations, and $a_0$ is the initial jet radius.

- The constant velocity of the first particle, $U_0$ is introduced to initiate the computation until the distance between the tip and the particle equals the initial bead length, $l_0$ [96].

$$U_0 = -\frac{Q}{\pi a_0^2} z \tag{3.41}$$

where the volume flow rate, $Q$; the initial jet radius, $a_0$; and the initial bead length, $l_0$ are considered as input data.

Fig. 3.6 (a) illustrates a simulation of the electrospun jet by using the similar values that were used in [18] and the improved model. However, it is very difficult to use the experimental data for validating the correctness of the physical model. This is due to the difficulties in estimating proper values of the

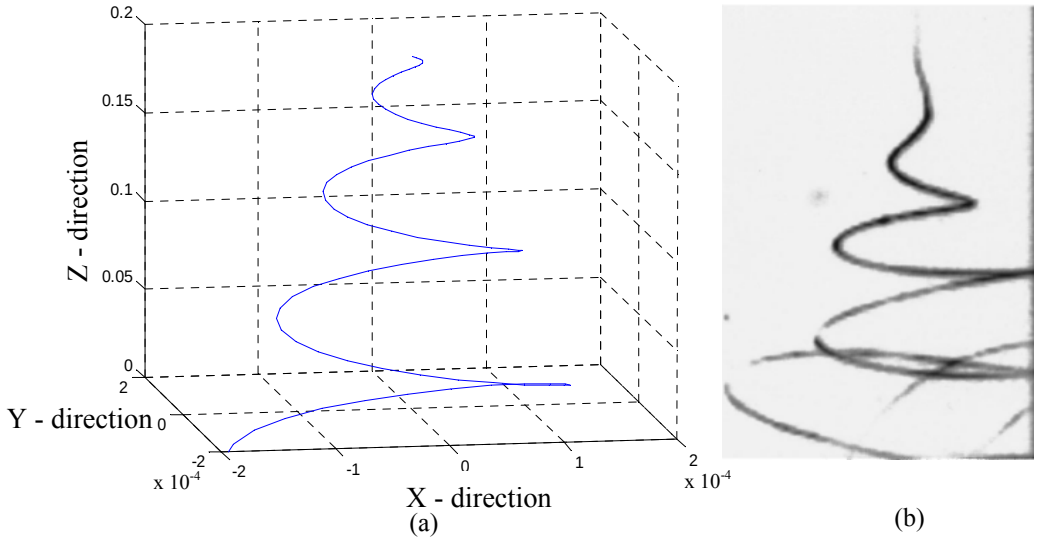


Fig. 3.6: (a) Simulation of a growth of the bending instability along the jet axis of a charged jet subject to a small perturbation. (b) Stereographic image of an electrically driven bending instability [18].

basic parameters necessary for modelling, such as charge density, mass, charge flow rate, variation of fluid parameters, and initial conditions. Fig. 3.6 (b) illustrates a stereographic image which shows a real electrospun jet. A comparison of bending instability in *x* and *y* directions versus *z* direction is shown in Fig 3.7. The z measurements are taken from the collector plate in upward direction. The simulated shape of the electrospun jet using the improved model closely matches with the real jet as shown in Fig. 3.6 (a), Fig. 3.7 (a) and Fig. 3.7 (b).

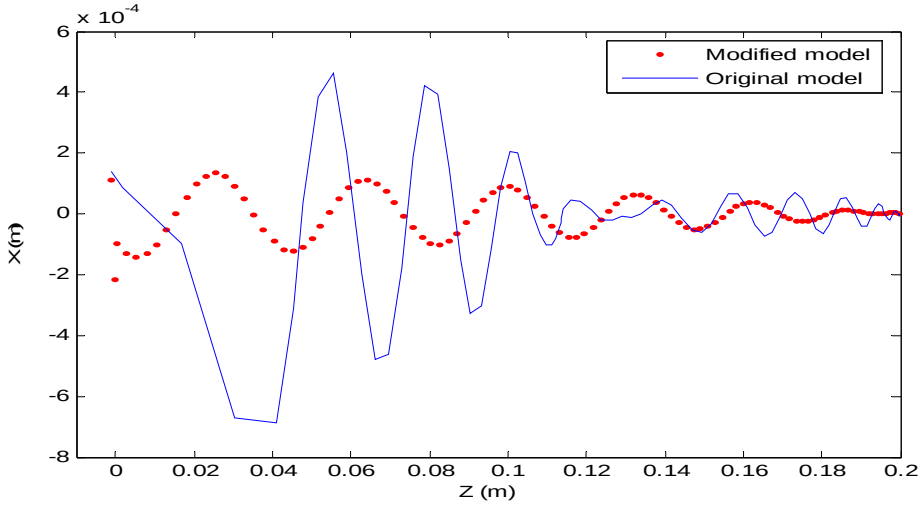


(a)

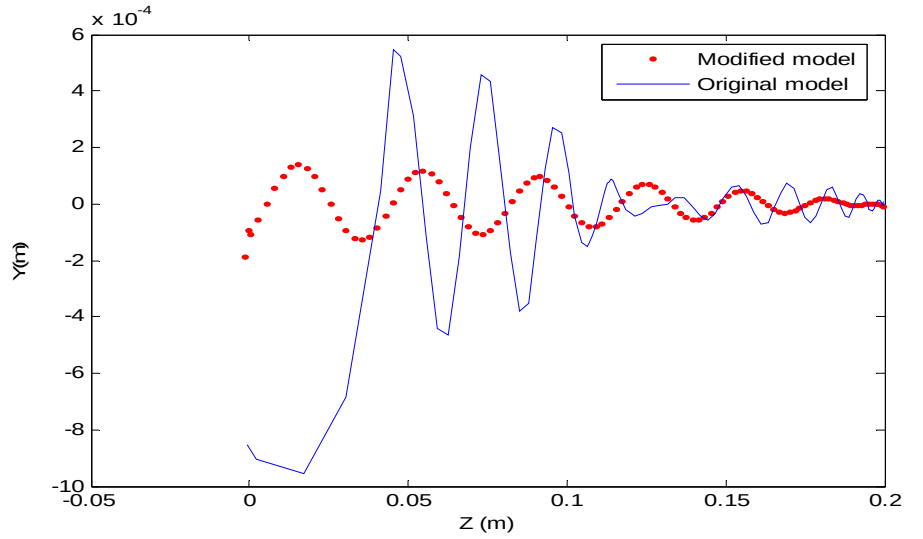


(b)

Fig. 3.7: Bending instability in *x* and *y* directions versus *z*-direction. (a) Variation in *x*-direction. (b) Variation in *y*-direction.

# Chapter 4

# Simulation and Experimental Procedures

## 4.1 Electric Field Simulation

The electric field between the needle tip and the collector plate was varied by changing the applied voltage as well as the distance between the needle tip and the collector plate. The distribution of the electric field between the needle tip and the collector plate was simulated by using a finite element method (FEM) software COMSOL® Multiphysics. The "Conductive Media DC Application Mode" was used for the simulation since the used polymer solution was assumed to be a weakly conductive liquid. The system is governed by Equation (4.1) [99]. The input parameters to the model were the conductivity of the solution ($K$) and the applied voltage to the needle ($V$).

$$-\nabla.\left(K\nabla V - J\right) = Q \tag{4.1}$$

Where, $J$ is the externally generated current density and $Q$ is the value of current source [99]. As expected, the electric field at the tip of the fluid droplet increases with the increase in applied voltage and decreases with the increase in distance between the needle tip and the collector plate.

### 4.1.1 Single-Needle Arrangement

A symmetrical fluid droplet at the tip of the needle was considered for the simulation as shown in Fig. 4.1. In our calculations of electric field, the charged jet was ignored as the main objective was to study the jet initiation. The electric field near the needle tip is mainly influenced by the external

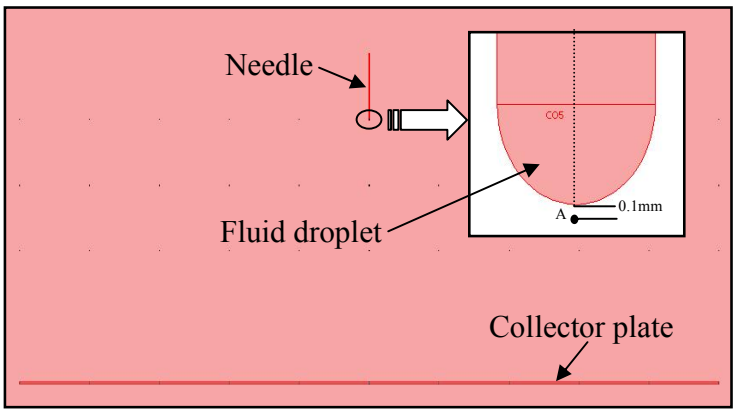


Fig. 4.1: Needle and collector plate arrangement used for single-needle FEM simulation.

electric field due to the applied voltage. However, the charged jet and the space charge distribution must be accounted for greater accuracy of the results. The initial average electric field in close proximity to the tip of the fluid droplet (at point A in Fig. 4.1) for different configurations was calculated and the results are illustrated in Fig. 4.2.

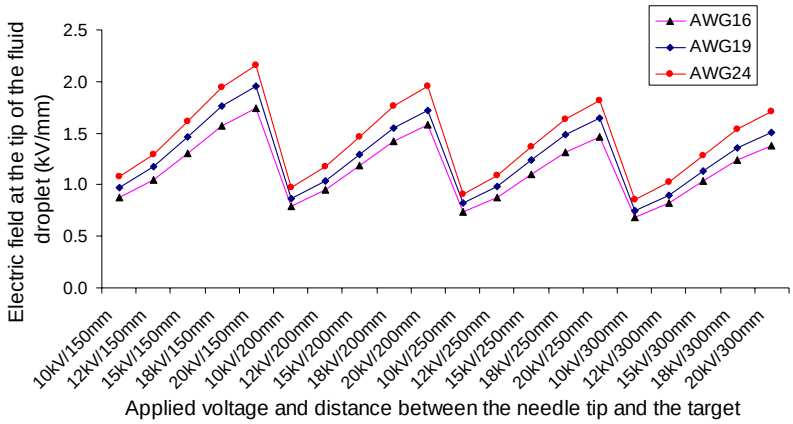


Fig. 4.2: Variation in the electric field at the tip of the fluid droplet for different needle configurations with the applied voltage and distance between the needle tip and collector plate.

### 4.1.2 2-Needle Arrangement

Fig. 4.3 illustrates a cross section of three dimensional (3D) COMSOL model that was used to calculate the electric field distribution between the needles and the target for a 2-needle arrangement. Needle dimensions of AWG 19 were used in the modeling, and the needles were placed 250 mm vertically

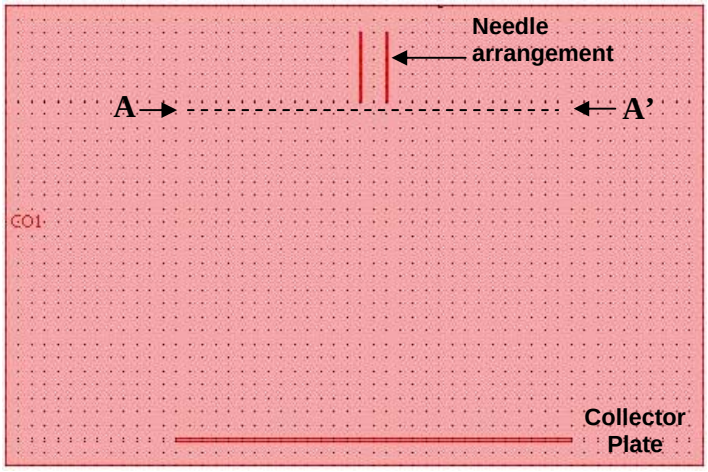


Fig. 4.3: Needle and collector plate arrangement used for 2-needle FEM simulation.

above the target to match with the experimental setup. The diameter of the target is 300 mm. The simulation was carried out for single-needle, 2-needle, 3-needle, and 4-needle systems by varying the needle spacings.

Fig. 4.4 shows the electric field and potential distribution between the needles and the target for an application of 15 kV DC for both single-needle and 2-needle arrangements. The surface plots show the potential distribution, and the arrows indicate the field distribution. Although the overall field distribution appears identical for both cases, the local electric field distribution is significantly different. Fig. 4.5 shows the corresponding local electric field distribution at the needle tip for both cases. The maximum electric field strength at the tip is 2.40 kV/mm in the case of the singe-needle arrangement,

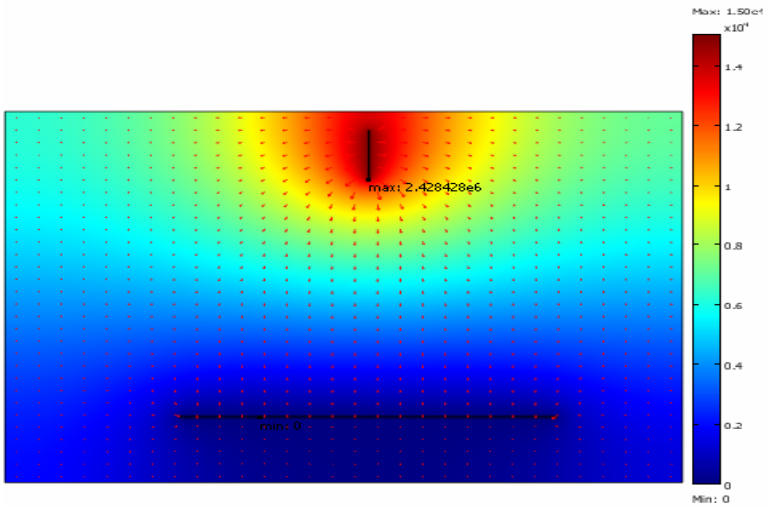


(a)

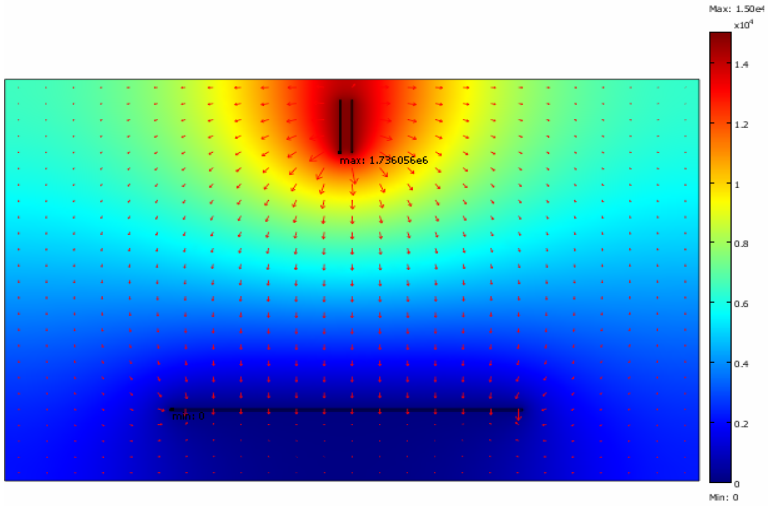


(b)

Fig. 4.4: Electric field distribution: (a) Single-needle arrangement. (b) 2-needle arrangement.

and 1.74 kV/mm for the 2-needle arrangement at 15 kV. In the single-needle arrangement, a significant enhancement in the electric field can be observed at the tip. However, in the 2-needle arrangement, the local electric field at each needle tip has deteriorated. Although an identical voltage with a similar magnitude and polarity has been applied in both cases, the electric field lines at the tips of the needles in the 2-needle arrangement has been significantly weakened than in the single-needle arrangement due to the repulsive field that has caused field distortion at the tips of the needles.

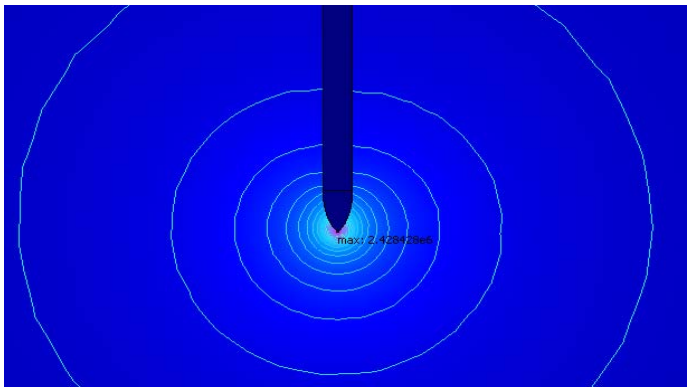

(a)

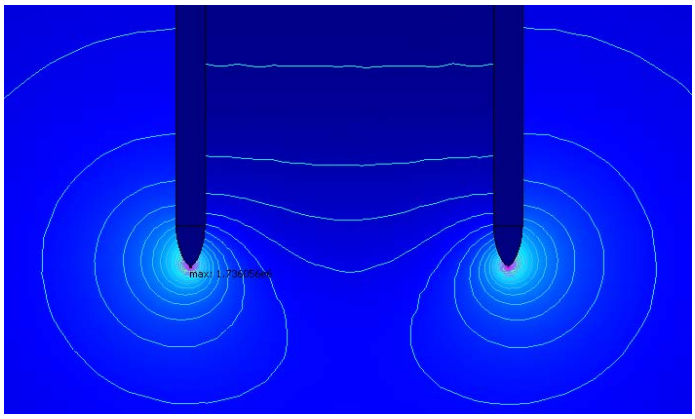

(b)

Fig. 4.5: Local electric field distribution: (a) Single-needle arrangement. (b) 2-Needle arrangement.

The spacing between the 2-needle arrangement was varied from 10 mm to 100 mm in 10 mm steps to investigate the optimum needle spacing in multi-jet electrospinning. The simulated field results are shown in Fig. 4.6 (a), the maximum electric field strength is observed for a single-needle arrangement followed by for the 2-needle arrangement for a spacing of 10 mm. Although the magnitude of the

maximum electric field drops significantly when 2 needles are used, the field varies very little as a function of the needle spacing for the range used in this study (10 mm to 100 mm) and does not follow any specific trend. The reason for this wavering behavior is the change in the distance between the collector edges and the needles as the spacing is changed whereas an infinite length collector plate is used the field strength at the needle tips gradually increases beyond 20mm spacing as shown in Fig 4.6 (b). The behavior of the electrospun jet is therefore highly unpredictable when the spacing of the needles varies. Achieving fiber uniformity is also difficult. Most importantly, the minimum voltage required in order to begin the electrospinning process is higher in the case of the 2-needle arrangement than for the single-needle arrangement.

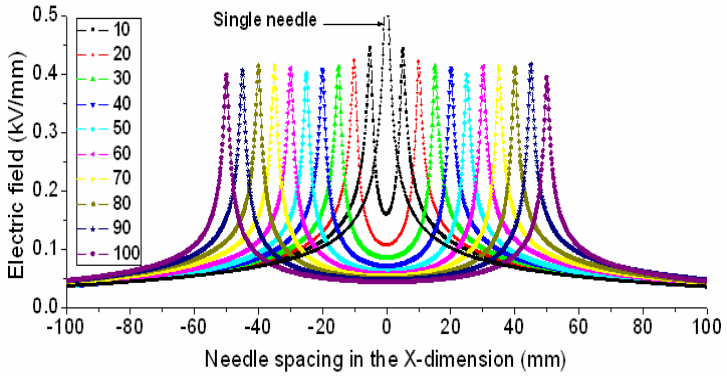


(a)

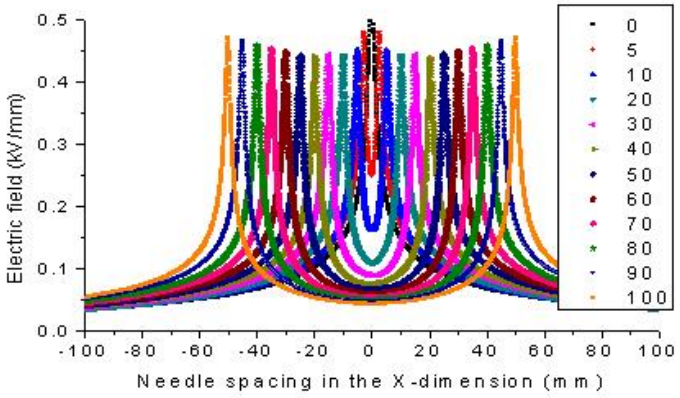


(b)

Fig. 4.6: Illustration of the electric field distribution along the line A-A' (Fig. 4.3) for different needle spacing in mm: (a) with the collector plate of actual experimental setup and (b) with an infinite collector plate.

### 4.1.3 Multi-Needle Arrangement

Fig. 4.7 shows the local electric field distribution at the needle tip for a 3-needle arrangement. Compared to the 2-needle arrangement, the maximum electric field at the tips of the needles is further reduced to 1.51 kV/mm. In addition, the electric field at the tip of the centre needle is reduced very significantly due to the influence of the other two needles. The reductions in the electric field at the tip of the centre needle with 10 mm, 20 mm, and 30 mm needle spacing are 25.7 %, 26.3 %, and 26.5 % of the maximum electric field of the arrangement, respectively.

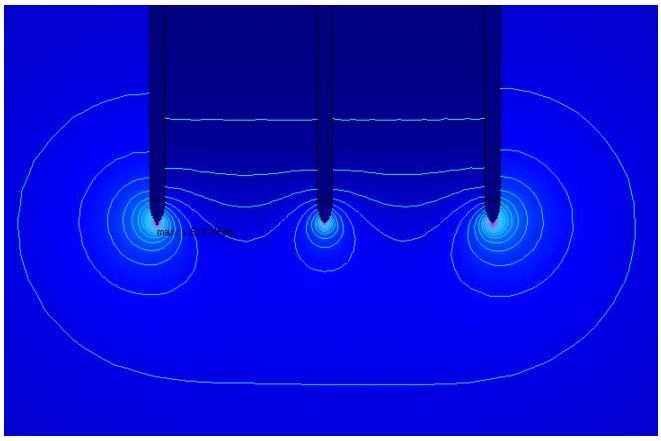

Fig. 4.7: Local electric field distribution for a 3-needle arrangement.

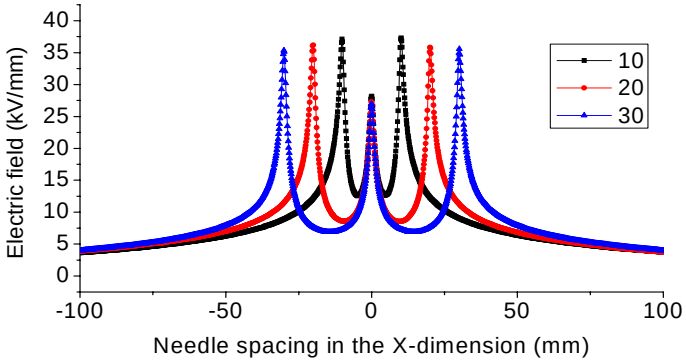


Fig. 4.8: Illustration of the electric field distribution along the line A-A' (Fig. 4.3) for different needle spacing in mm with a 3-needle arrangement.

The spacing between the needles was varied from 10 mm to 30 mm in 10 mm steps and the simulated electric field results are shown in Fig. 4.8, which reveals that, as with the 2-needle arrangement, the maximum electric field strength occur with the 10 mm needle spacing. The field also varies very little

at the tip of each needle for needle spacing from 10 mm to 30mm. However, due to the significant variation in the electric field at the tip of each needle, the behavior of the electrospun jet from each needle is considerably different, resulting in highly non-uniform fibers.

Fig. 4.9 and Fig. 4.10 show the local electric field distribution at the needle tip for a 4-needle arrangement. Compared to the single-, 2-, and 3-needle arrangements, the maximum electric field at the tips of the needle is further reduced to 1.45kV/mm. The percentage reductions in the electric field at the tips of the two middle needles are presented in Table 4.1. As shown in the table, the reductions in the electric field at the tips of the needles range from 27.21 % to 29.82 %. Therefore, the reduction in the electric field at the tips of needles 2 and 3 in Fig. 4.9 is higher than the reduction in the electric field at the tip of the centre needle with a 3-needle arrangement in Fig 4.7.

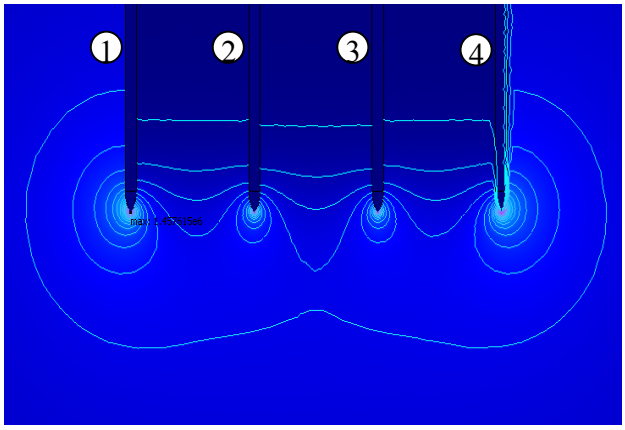


Fig. 4.9: Local electric field distribution for a 4-needle arrangement.

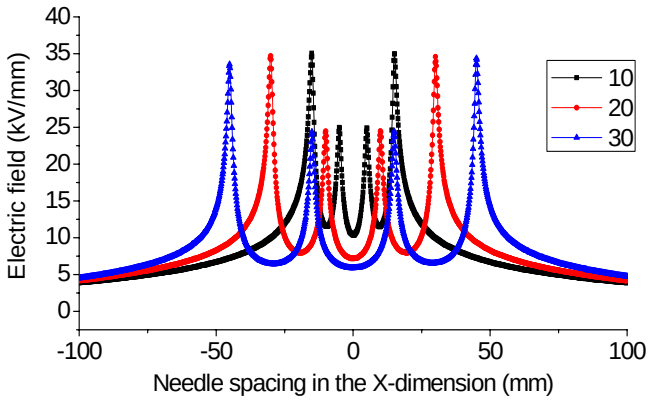


Fig. 4.10. Illustration of the electric field distribution along the line A-A' (Fig. 4.3) for different needle spacing in mm with a 4-needle arrangement.

From the observations of the electric field simulation, it can be concluded that as the number of needles in the arrangement increases, the electric field at the tip of each needle decreases significantly due to the influence of the surrounding needles in the arrangement. The weakening of the field is more severe at the tips of the centre needles than at the tips of either of the end needles. This field deterioration at the needle tips significantly affects fiber uniformity. As well, the minimum voltage required to start the electrospinning process also increases considerably, which results in the need for higher voltage sources.

Table 4.1: Percentage reductions of the electric field at the tip of the middle needles.

| Needle | Percentage reductions in the electric field at the tips of the centre needles for different needle spacing, % | | |
|---|---|---|---|
| | 10 mm | 20 mm | 30 mm |
| 2 | 28.94 | 29.49 | 27.33 |
| 3 | 29.14 | 29.82 | 27.21 |

## 4.2 Experimental Setups

### 4.2.1 Single-Needle Electrospinning

Fig. 4.11 illustrates a schematic of the experimental setup that was used to perform the electrospinning experiments and the apparatus was basically similar to that used in the previous work [18, 19, 26, 35-37]. The polymer solution was fed through a syringe needle arrangement at a constant rate from a syringe pump, resulting in the formation of a drop of polymer solution at the needle tip. Three different flow rates including 0.05 ml/min, 0.1ml/min, and 0.2ml/min were used during the experiments. Three needles of AWG of 16 (1.291mm), AWG of 19 (0.912mm), and AWG of 24 (0.511mm) inner diameters were used to investigate the effect of electric field on the electrospinning process and fibre morphology. Spellman high voltage DC power supply was used to apply the high voltage between the needle and the collector plate. The dimensions of the collector plate were chosen to be significantly larger than the distance between the needle and the collector plate hence; the edge effect could be ignored. A Keithley system electrometer (pico-ammeter) model 6514 was used to measure the jet current; it was connected between the collector plate and the ground electrode with a protection circuit, as shown in Fig. 4.11 [100].

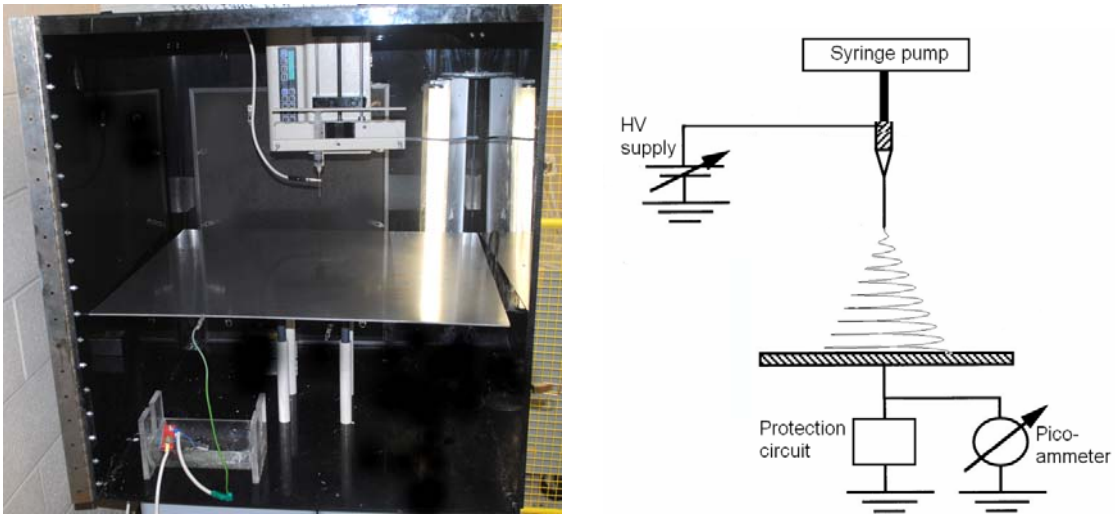


(a) (b)

Fig. 4.11: Electrospinning experimental apparatus: (a) Photograph of the apparatus and (b) Schematic of the apparatus.

### 4.2.2 Multi-Needle Electrospinning

Fig. 4.12 illustrates the setup used to perform the multi-jet electrospinning experiments. The polymer solution is forced through a syringe arrangement at a constant rate of 0.1 ml/min from a syringe pump through low density polyethylene (LDPE) tubes with an AWG of 19, resulting in the formation of a drop of polymer solution at the needle tip. Spellman high voltage DC power supply was used to apply the required high voltage between the needles and the collector plate.

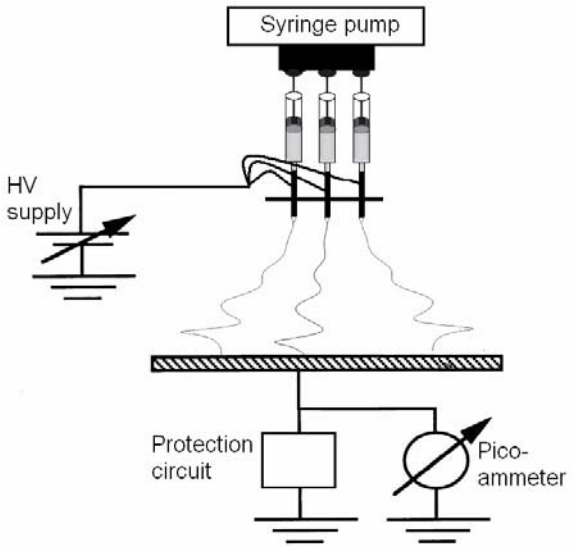


Fig. 4.12: Schematic of the experimental apparatus of multi-needle electrospinning.

The needles were mounted vertically above the collector plate in all experiments. A Keithley system electrometer (pico-ammeter) model 6514 was used to measure the total jet current; it was connected between the collector plate and the ground electrode with a protection circuit (see Appendix D), as shown in Fig. 4.12. A variable voltage was applied between the needles and the target, and in all cases a distance of 250 mm was maintained between the needles and the target. The electrospun fibers were collected on a flat 300 mm diameter target.

### 4.2.3 Monitoring of the Straight Jet Portion

As shown in Fig. 4.13, the straight jet portion of the electrospun jet moves away from the vertical line with the distortion in the local electric field at the needle tip due to the presence of the

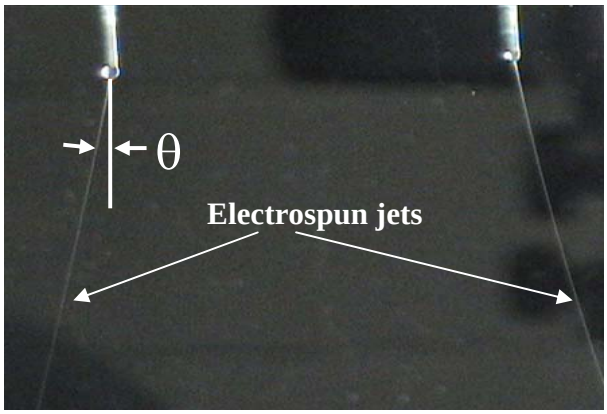


Fig. 4.13: Representation of the vertical angle of the straight jet portion of the electrospun jet.

additional needle/needles in the multi-jet schemes. Here, the angle between the vertical line and the straight jet portion of the actual electrospun jet is defined as the vertical angle of the straight jet portion, $\theta$. A SONY® DCR-HC28 camcorder was used to capture the images of the straight jet portion of the jet during electrospinning and an image processing tool was used to calculate the angle, $\theta$.

### 4.2.4 Characterizing the Morphology of Nanofibres

The electrospun fibres were investigated with a Scanning Electron Microscope (SEM) model Leo 1530 Gemini that is shown in Fig. 4.14. An image processing tool was used to determine the average fibre diameter. About 50 fibre diameters were measured from multiple SEM images to calculate the average fibre diameter for the analysis.

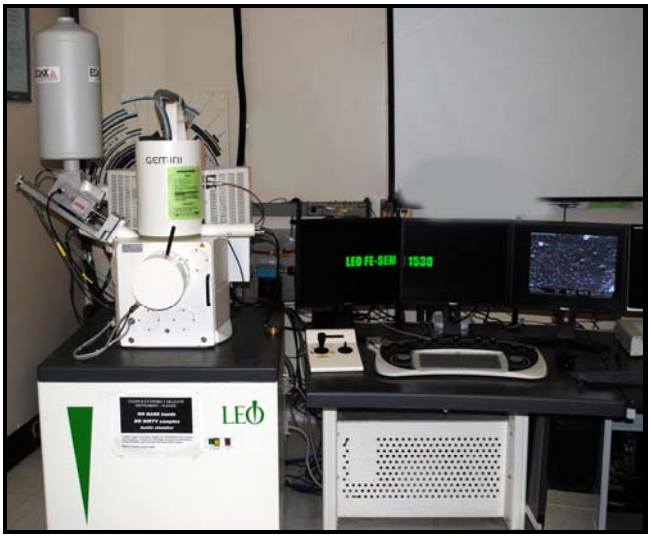


Fig. 4.14: Leo 1530 Gemini Field Emission Scanning Electron Microscope (FESEM).

### 4.2.5 Variation in the Conductivity of the Liquid under DC High Voltage

Fig. 4.15 shows a schematic of the experimental apparatus that was used to determine the variation in the conductivity of a liquid sample with the application of DC high voltage. Spellman high voltage DC power supply was used to apply the required high voltage between the needle and the ground electrodes. As shown in Fig. 4.15, an ammeter was used to measure the total current flow through the liquid under test. When the magnitude of the applied voltage is increased, the liquid in the container ionizes resulting in the variation in the conductivity of the liquid. The current through the circuit varies

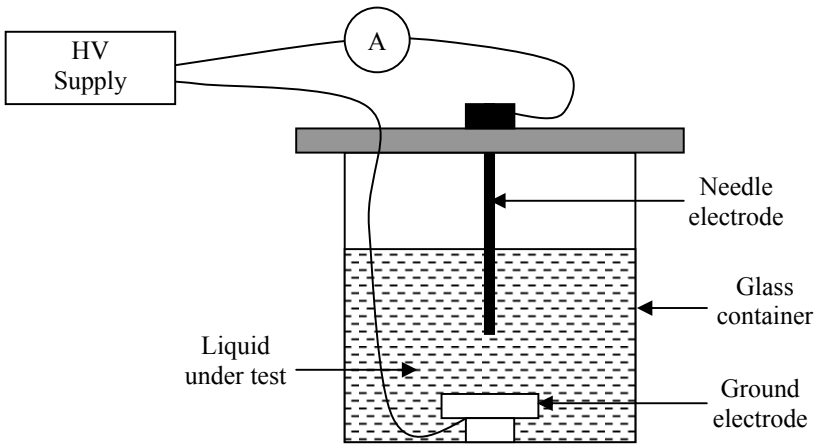


Fig. 4.15. Schematic of the experimental arrangement of determining the variation in the conductivity of a liquid under DC high voltage.

with the variation in the conductivity of the liquid and hence, the measured current is an estimation of the amount of variation in the conductivity of the liquid.

### 4.2.6 Measurement of Solution Parameters

The dynamic viscosities of the samples were measured using a shear capillary rheometer mounted on an Instron Universal Testing Machine Model 1122. Tests were conducted at 4 crosshead speeds from 100 to 400 mm/min by 100 mm/min steps with samples of 50 ml loaded into the barrel. The length of the capillary was 150 mm, and the inner diameter was 1.5 mm. The area of the plunger was $5.3 \times 10^{-4}$ $m^2$. The viscosity was determined using the relationship between the pressure drop and flow rate which correspond to shear stress and shear rate, respectively. All tests were conducted at room temperature and ambient air.

A custom-made laboratory setup was used to measure the surface tension of the samples using the ring method. A platinum-iridium ring with a diameter of 19.05 mm was used, and maximum accuracy was achieved by washing the ring repeatedly using boiling water, petroleum ether, and acetone, respectively. Each sample, contained in a 50 mm diameter glass dish, was placed on a precision electronic balance (Mettler-Toledo Laboratory & Weighing Technologies) and was measured the force required to lift the ring from the solution. Thereafter the surface tension was calculated using Equation (4.2).

$$\gamma = \left( \frac{Mg}{4\pi R_{ring}} \right) \times \beta_{st} \tag{4.2}$$

where $M$ is the mass of the liquid in kg, lifted above the liquid surface before it breaks up, $g$ is the acceleration of gravity, $R_{ring}$ is the radius of the ring, and $\beta_{st}$ is the surface tension correction factor which depends on force and $R_{ring}$ [101].

In addition, the conductivity of the samples was measured by means of an OAKTON® conductivity meter model CON 110. The measuring electrode was rinsed with de-ionized water to remove any impurities adhering to the electrode body. After air drying, the electrode was rinsed with a small volume of sample liquid to avoid contamination or dilution. Then, the electrode was dipped into the sample with taking care to ensure that the liquid level is above its upper steel band. The sample was stirred smoothly to create a homogenous sample. Finally, the reading was taken after allowing enough time for stabilizing the measurement.

# Chapter 5
# Effects of Electric Field

## 5.1 Introduction

As reported in the literature, the entire electrospinning process is governed by the external electric field caused by the applied voltage between the electrodes and the induced electric field caused by free and induced charges on the fluid surface [1, 10-15, 18]. Therefore, the electric field is a crucial parameter in electrospinning, and parameters such as voltage, polarity, distance between the needle tip and the target, the shape of the collector, and needle characteristics can be used to control the electric field. Consequently, these parameters can be used to notably vary the nanofibre morphology. In this chapter, a comprehensive analysis is carried out to investigate the effects of external and induced electric fields on single-needle and multi-needle electrospinning processes which include the Taylor cone formation, the straight jet portion, and the unstable or whipping jet region. The variations in the morphology of nanofibres are also examined.

## 5.2 Preparation of Materials

Polyethylene oxide (PEO) with an average molecular weight of 600,000Da purchased from Aldrich® was chosen to prepare the solutions. PEO fibres were electrospun using 2.5%, 5%, and 7.5% (w/w) concentrations of PEO in de-ionized water. The solutions were stored at room temperature and all electrospinning experiments were done at room temperature and atmospheric air.

## 5.3 Effects of Electric Field on a Single-Needle System

The electrospinning process consists of three stages according to the behaviour of the electrospun jet as shown in Fig. 5.1. This includes the formation of Taylor cone, the ejection of straight jet, and the unstable whipping jet region. According to our observations, the electric field at the tip of the fluid droplet and the distance between the needle tip and the target influence in different ways the three major stages of the electrospinning process, described earlier.

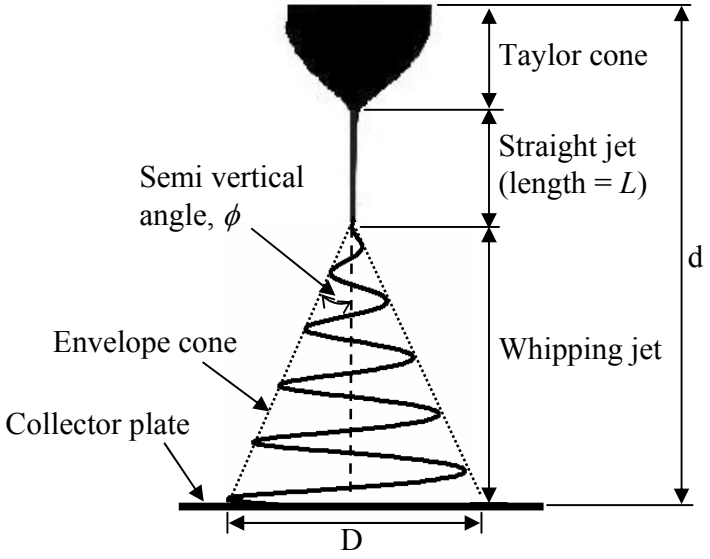


Fig. 5.1: Behaviour of the electrospun jet.

### 5.3.1 Behavior of Taylor Cone

As reported in the literature, the fluid droplet at the needle tip forms the Taylor cone with the application of an external electric field. However, the behaviour of the fluid droplet is highly influenced by the strength of the applied electric field. As shown in Fig. 5.2 (a), if the applied field strength is below a lower threshold value (~0.9kV/mm), polymer droplets were formed during the electrospinning process. This changes the electrospun jet current intermittently and hence, the fibre uniformity is affected. On the other hand, if the electric field is increased beyond an

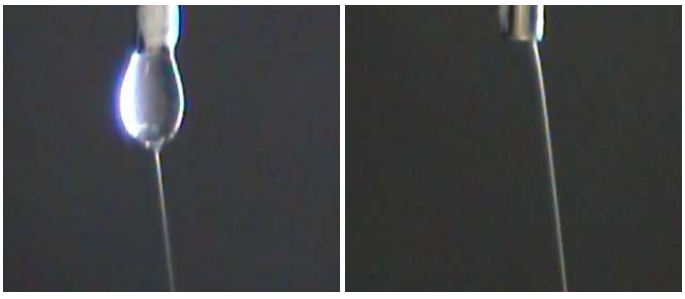

(a) (b)

Fig. 5.2: Behaviour of the fluid droplet at the tip of the needle: (a) Applied electric field is below the lower threshold and (b) Applied electric field is above the higher threshold.

upper threshold value (~1.1kV/mm), the Taylor cone disappears at the tip of the needle. It causes the straight jet to be unstable forming non-uniform fibres. This is illustrated in Fig. 5.2 (b). Therefore, it was observed that the working range of electric field is a very narrow range (0.9–1.1kV/mm) for perfect electrospinning.

### 5.3.2 Effects on Jet Current

The surface charges induced by the applied electric field govern the entire electrospinning process. Therefore, the jet behaviour can be analyzed by measuring the amount of surface charge that is carried by the electrospun jet. The jet current represents the charge carried by the jet and therefore, the measured jet current was used for the investigation. Fig. 5.3 (a) illustrates the behaviour of the measured electrospun jet current with varying electric field for the different needles. Similarly, Fig. 5.3 (b) and Fig. 5.3 (c) illustrate the behaviour of electrospun jet current for different flow rates and PEO concentrations respectively. The variation of average jet current, $I$ as a function of applied electric field strength, $E$ approaches the power law relationship ($I=kE^{P}$) with increasing field. The coefficient $p$ lies between 3.1 and 3.4. In the literature, it has also been reported that the average jet current $I$ as a function of applied voltage $V$ approaches a power law relationship with increasing voltage [55, 82]. As shown in Fig. 5.3 (a), the needles with larger diameter show a higher jet current while the needles with a smaller diameter induce a higher electric field at the tip. This is caused by the larger droplet size at the larger diameter needle forming more surface charges at the fluid surface. Similarly, as shown in Fig. 5.3 (b), the jet current increases with the increase of flow rate of the polymer solution. The flow of charges increases with the increase of flow rate resulting in higher jet current. In addition, as illustrated in Fig. 5.3 (c), a higher jet current was observed with the increase of PEO concentration in the aqueous polymer solution.

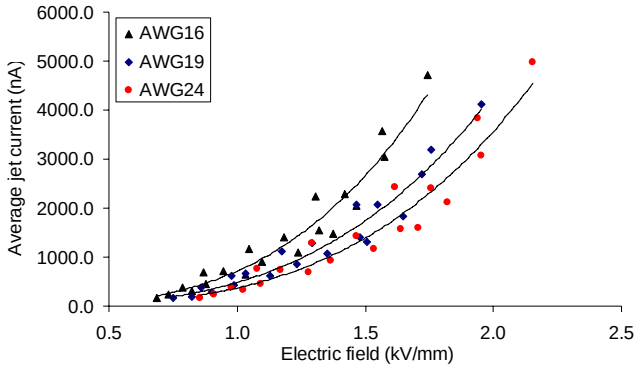


(a)

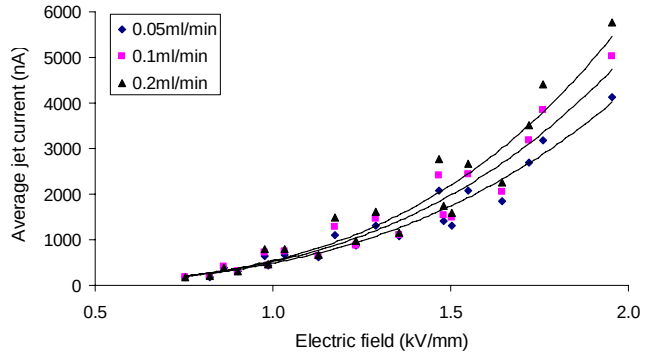


(b)

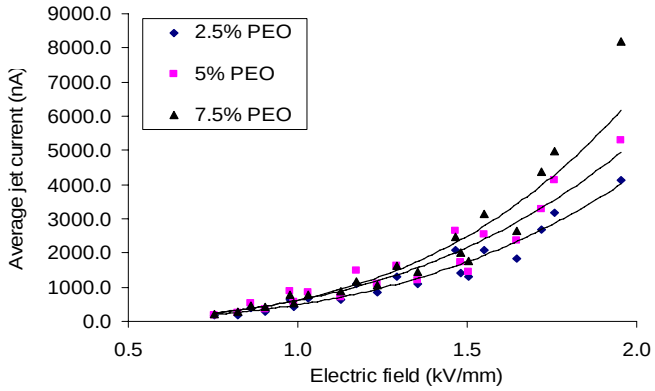


(c)

Fig. 5.3: Behaviour of the average electrospun jet current with the increase of applied electric field. Here, the same data set of electric field as in Fig. 3 has been used: (a) Using 2.5% PEO/water solution with 0.05ml/min flow rate for needles with different diameters, (b) Using 2.5% PEO/water solution with the needle of AWG19 inner diameter for different flow rates, and (c) for different aqueous PEO solutions with the needle of AWG19 inner diameter and flow rate of 0.05ml/min.

### 5.3.3 Behavior of Straight Jet

The interaction of applied electric field with the electrostatic charges at the fluid surface results in the ejection of straight fluid jet. Therefore, both the applied electric field and the amount of induced charges determine the behaviour of the straight jet portion. Fig. 5.4 shows the variation of the length of the straight jet portion, *L*. It is observed that the length of the straight jet portion increases linearly with

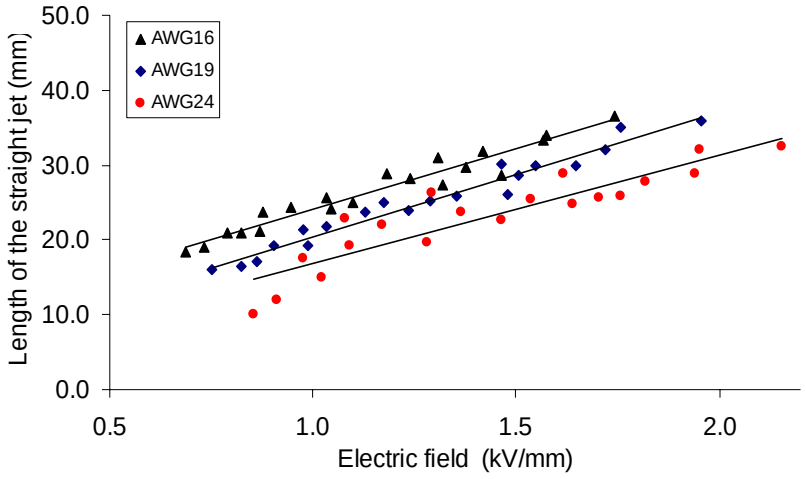


(a)

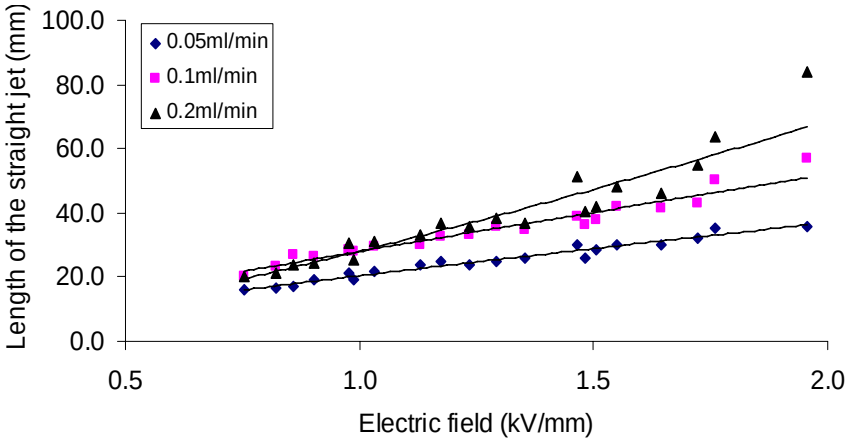


(b)

Fig. 5.4: Behaviour of the length of the straight jet with the increase of applied electric field. Here, the same data set of electric field as in Fig. 3 has been used: (a) Using 2.5% PEO/water solution with 0.05ml/min flow rate for needles with different diameters and (b) Using 2.5% PEO/water solution with the needle of AWG19 inner diameter for different flow rates.

the increase of applied electric field. Moreover, as shown in Fig. 5.4 (a), the larger diameter needles generate increased length of the straight jet. The reason must be due to the increased surface charges with the increased size of the fluid droplet. As shown in Fig. 5.4 (b), the length of the straight jet portion increases with the increase of solution flow rate from 0.05ml/min to 0.2ml/min. This concludes that the increase of surface charges increase the interaction between the external electric field and the charges forming longer straight jets.

The data of the length of the straight jet of 5% PEO solution was presented in Table 5.1. It also confirms the similar trend with the straight jet formation as those in the other cases. However, at very high electric fields, the solid fibres were not able to obtain due to increased stretching of the straight jet portion. In addition, there is no visible whipping region at very high electric fields.

Table 5.1: Length of the straight jet with the increase of applied voltage for varying distance between the needle and the collector plate of 5% PEO solutions at the flow rate of 0.05ml/min.

| Voltage (kV) | Length of the straight jet portion ($L$) for different distances between the needle and the collector plate (mm) | | | |
|---|---|---|---|---|
| | 150mm | 200mm | 250mm | 300mm |
| 10 | 54.6 | 36.8 | 17.1 | 18.9 |
| 12 | 65.0 | 40.5 | 50.3 | 25.7 |
| 15 | 95.0 | 46.8 | 42.2 | 42.7 |
| 18 | No fibre formation | 46.9 | 55.1 | 46.1 |
| 20 | No fibre formation | 42.7 | 46.2 | 46.6 |

### 5.3.4 Characteristics of Whipping Jet

Once the straight electrospun jet flows away from the Taylor cone, it is subjected to the bending instability. It makes the jet path to take a conical shape as shown in Fig. 5.1. The stretching of the electrospun jet and the bending instability are controlled by the Coulomb force between charges and the force due to the external electric field. As reported in the literature, most of the stretching of the fibre is happening in the whipping region. Therefore, the size of the whipping region has a greater influence on the diameter of nanofibres. The behaviour of the electrospun jet in the whipping region is investigated by measuring the diameter of the collected area ($D$) since it is proportional to the semi vertical angle ($\phi$) of the envelope cone. Fig. 5.5 (a), (b), and (c) illustrate the variation of $D$ with the increase of applied

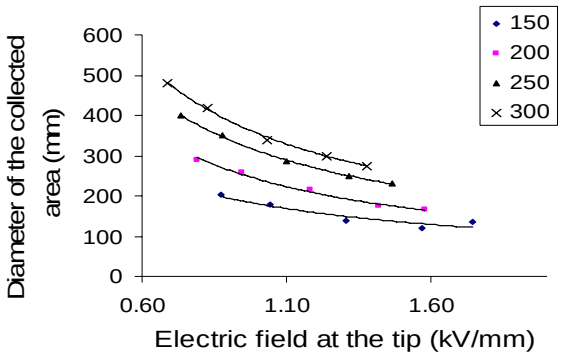


(a)

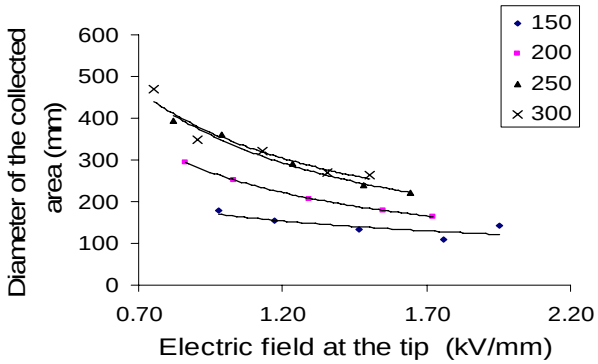


(b)

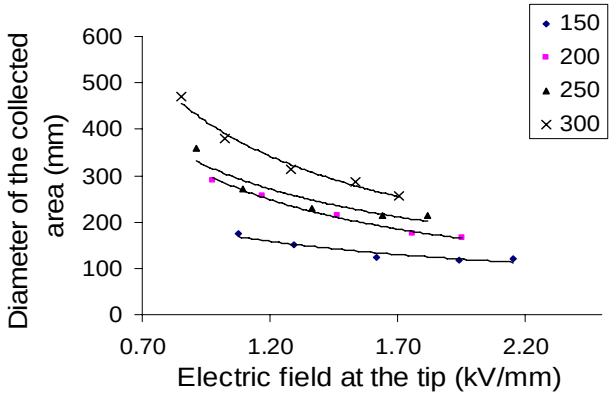


(c)

Fig. 5.5: Behaviour of *D* with the increase of applied electric filed for a range of distances between the needle tip and the collector plate (in millimeters) for a 2.5% PEO/water solution at a flow rate of 0.05ml/min. Here, the same data set of electric field as in Fig. 3 has been used: (a) Needle of AWG of 16 inner diameter, (b) Needle of AWG of 19 inner diameter, and (c) Needle of AWG of 24 inner diameter.

electric field for needles with different inner diameters. As shown in the figures, *D* depends not only on

the applied electric field but also on the distance between the needle tip and the collector plate. However, $D$ decreases with the increase of applied electric field. The results show a relationship of $D = k E^q d^r$ with increasing the electric filed ($E$) and the distance between the needle and the collector plate ($d$). It was observed that the coefficient of $q$ lies between (-0.7) and (-0.8). Furthermore, the coefficient, $r$ is very close to 1 in all the experiments. Similar observation was done with varying solution flow rate and PEO concentration.

### 5.3.5 Morphology of Nanofibres

Fig. 5.6 (a), (b), and (c) show the variation of average fibre diameter with increasing electric field of needles with different inner diameters for a 2.5% PEO/water solution at the solution flow rate of 0.05ml/min. Similarly, Table 5.2 and 5.3 show the values of average fibre diameter for a 5% PEO/water solution at the flow rate of 0.05ml/min and 2.5% PEO/water solution at the flow rate of 0.1ml/min. The diameter and uniformity of nanofibres are significantly influenced by the behaviour of all three regions in the electrospinning process. Therefore, the determination of fibre diameter with varying applied electric field is not straightforward due to the different behaviour of the electrospun jet in different regions. However, by comparing the fibre diameters with the applied electric field and the distance between the needle tip and the collector plate, it can be concluded that the fibre diameter decreases with increasing electric field if there is enough space for whipping region as the fibre diameter can be decreased with the increased stretching of the electrospun jet. The stretching of the electrospun jet increases with the increase of surface charges at the jet surface and flying time of the jet. The surface charges at the fluid surface increases with the increase of applied electric field. Equally, the length of the straight jet portion increases with the increase of applied electric field. On the other hand, whipping time decreases with the increase of applied electric field. Therefore, if the distance between the needle tip and the collector plate is not large enough, there is not enough time for the electrospun jet to decrease its diameter even at higher electric fields; hence, increases the fibre diameter with increasing electric field. Furthermore, it was observed that the fibre diameter cannot be varied significantly by changing the applied electric field. The fibre diameter can be varied considerably by changing the material parameters such as conductivity and viscosity.

Fig. 5.7 illustrates the SEM images of electrospun fibres for different combinations of applied voltages and distances between the needle tip and the collector plate. It is observed that the shape of the beads changes from spherical to spindle with the increase of distance between the needle tip and the target or the use of smaller diameter needle. The shape of the beads depends on the degree of stretching during the electrospinning process. The stretching into nano-scale mainly occurs during the whipping region. The whipping region is increased significantly with increasing the distance between the needle

tip and the collector plate. This results in the transformation of beads from spherical to spindle like shape due to the increased stretching.

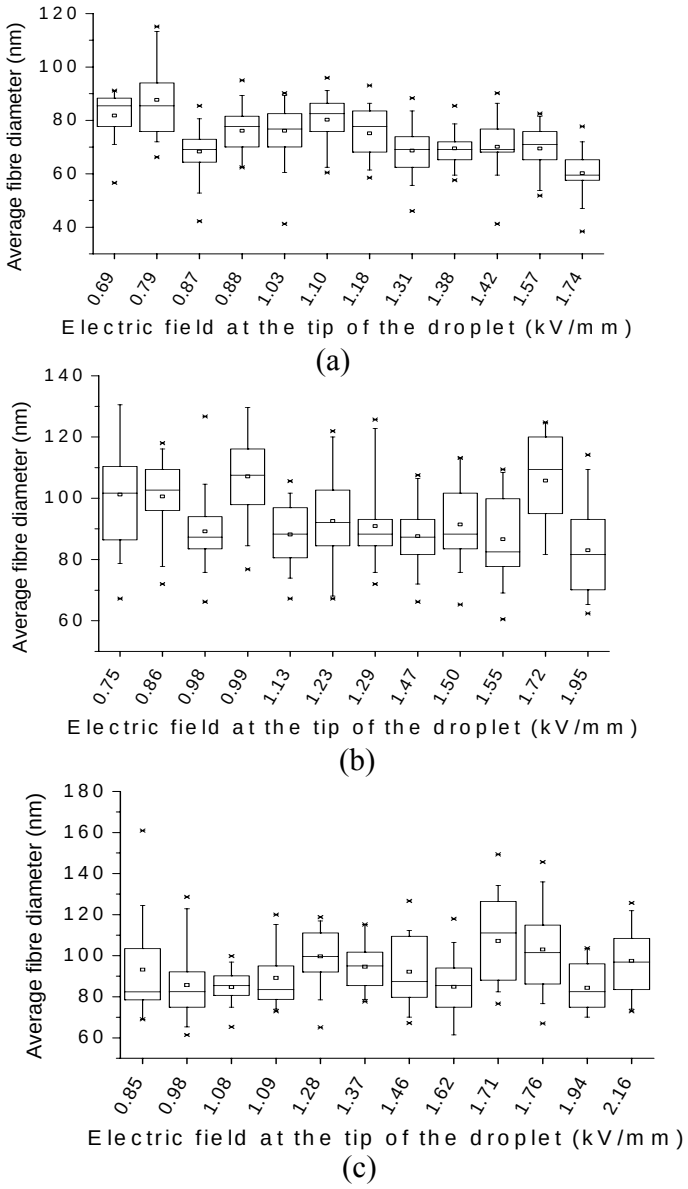


Fig. 5.6: Variation of average fibre diameter with the increase of electric field at the tip of the fluid droplet. The average fibre diameter is represented by the cross inside the box; the median is represented by the horizontal line inside the box; the 25$^{th}$ and 75$^{th}$ percentiles are represented by the horizontal lines of the box. Error bars above and below the box indicate the 90$^{th}$ and 10$^{th}$ percentiles. The crosses above and below the box represent the maximum and the minimum of the sample respectively: (a) Needle of AWG of 16 inner diameter, (b) Needle of AWG of 19 inner diameter, and (c) Needle of AWG of 24 inner diameter.

Fig. 5.8 and Fig. 5.9 illustrate the SEM images of electrospun fibre morphologies with varying solution flow rate and PEO concentration at a constant electric field respectively. As shown in Figures 5.8 (a), (b), and (c), the shape of the beads changes from spherical to spindle like shape with increasing the solution flow rate. The increased flow rate helps to increase the surface charge density at the fluid surface resulting in a greater stretching during the electrospinning process. As illustrated in Figures 5.9 (a), (b), and (c), the increased PEO concentration has helped to completely eliminate the beads in the fibre. The viscosity and conductivity of the solution change considerably with the increase of polymer concentration producing beads free nanofibres during the electrospinning process.

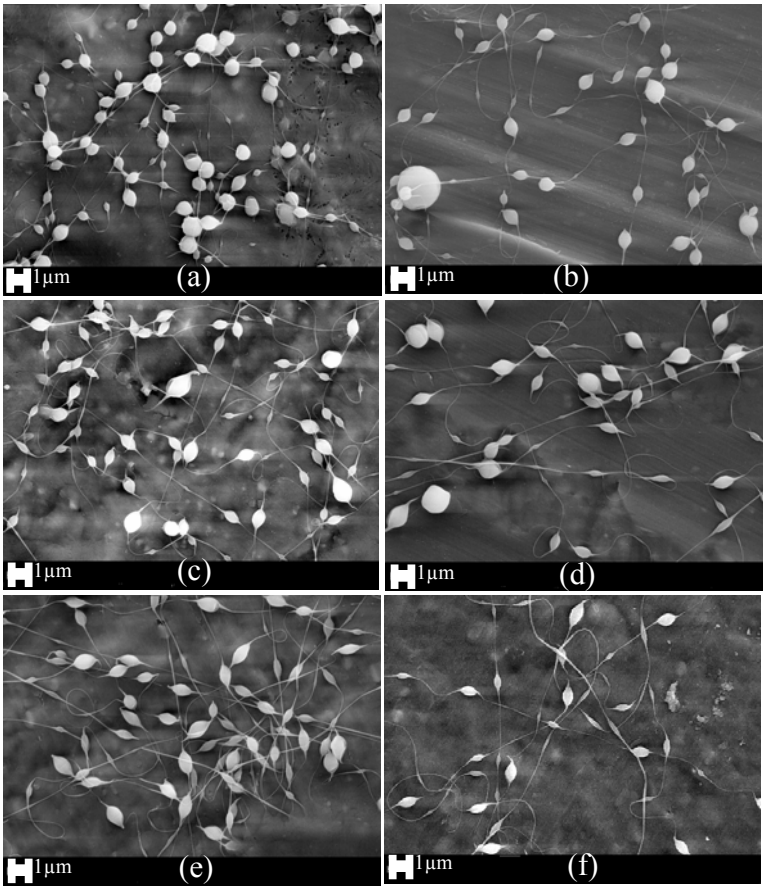


Fig. 5.7: SEM images of electrospun fibres with beads using 2.5% PEO/water solution at the flow rate of 0.05ml/min: (a) AWG16-10kV-150mm, (b) AWG16-10kV-300mm, (c) AWG19-10kV-150mm, (d) AWG19-10kV-300mm, (e) AWG24-10kV-150mm, and (f) AWG24-10kV-300mm.

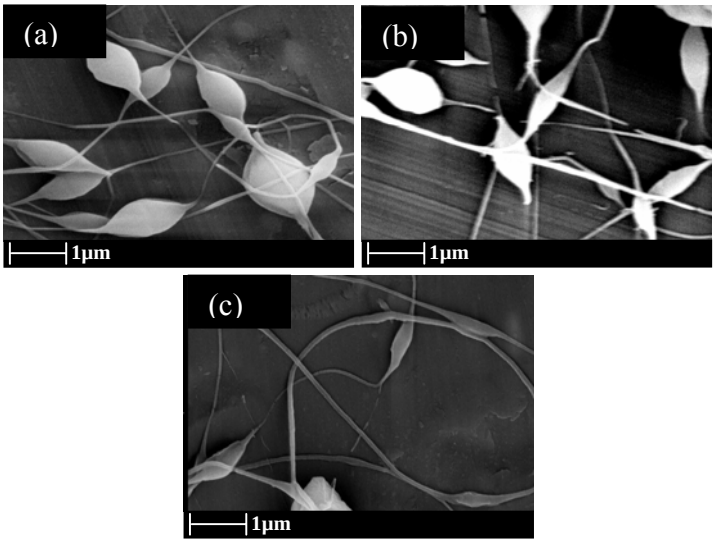


Fig. 5.8: Different morphologies of electrospun fibres of 2.5% PEO/water solution with a configuration of AWG19-20kV-300mm: (a) At the flow rate of 0.05ml/min, (b) At the flow rate of 0.1ml/min, and (c) At the flow rate of 0.2ml/min.

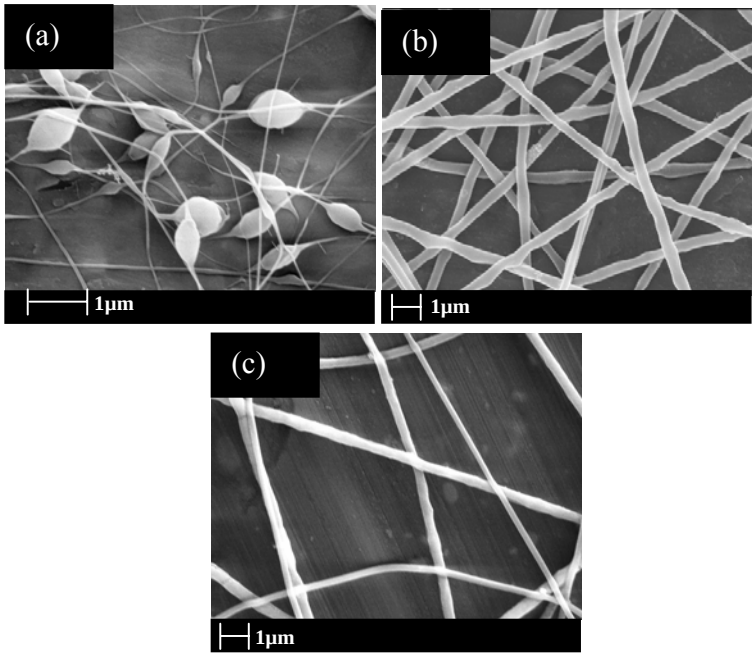


Fig. 5.9. Different morphologies of electrospun fibres with a configuration of AWG19-20kV-250mm and a flow rate of 0.05ml/min: (a) 2.5% PEO/water solution, (b) 5% PEO/water solution, and (c) 7.5% PEO/water solution.

Table 5.2: Average fibre diameter with the increase of applied voltage for varying distance between the needle and the collector plate of 5% PEO solutions at the flow rate of 0.05ml/min.

| Voltage (kV) | Average fibre diameters for different distances between the needle and the collector plate using a needle of AWG 19 (nm) | | | |
|---|---|---|---|---|
| | 150mm | 200mm | 250mm | 300mm |
| 10 | 532 ± 100 | 393 ± 50 | 351 ± 54 | 320 ± 60 |
| 15 | - | 366 ± 65 | 407 ± 70 | 412 ± 50 |
| 20 | - | 330 ± 40 | 363 ±75 | 382 ± 55 |

Table 5.3: Average fibre diameter with the increase of applied voltage for varying distance between the needle and the collector plate of 2.5% PEO solutions at the flow rate of 0.1ml/min.

| Voltage (kV) | Average fibre diameters for different distances between the needle and the collector plate using a needle of AWG 19 (nm) | | | |
|---|---|---|---|---|
| | 150mm | 200mm | 250mm | 300mm |
| 10 | 112 ± 40 | 82 ± 20 | 78 ± 15 | 115 ± 45 |
| 15 | 110 ± 30 | 107 ± 40 | 124 ± 35 | 96 ± 25 |
| 20 | - | 113 ± 35 | 95 ± 30 | 127 ± 40 |

## 5.4 Effects of Electrode Polarity

The effects of polarity of applied voltage were investigated using the experimental setup that is shown in Fig. 4.11 (a). Positive and negative DC, 60Hz AC, and pulse (square) voltages were investigated during the experiments. The shapes of these waveforms are shown in Fig. 5.10.

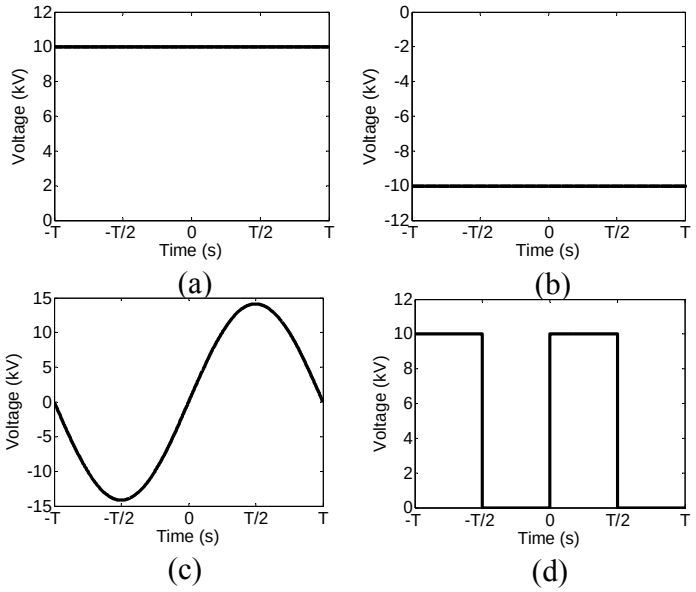


Fig. 5.10: Shapes of waveforms: (a) positive DC, (b) negative DC, (c) 60Hz AC, and (d) Square pulse.

### 5.4.1 Experimental Results

#### 5.4.1.1 Behavior of Jet Current

Experimental data for the variation in average jet current versus applied voltage for both positive and negative polarities are shown in Fig. 5.11. Observations again confirmed the

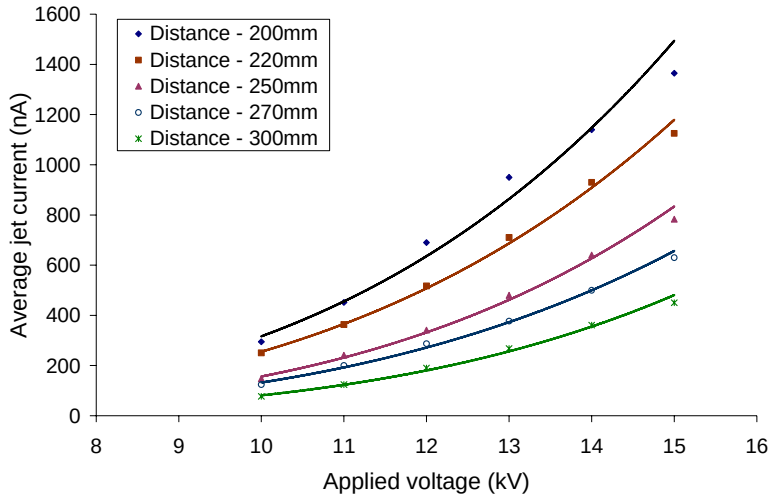


(a)

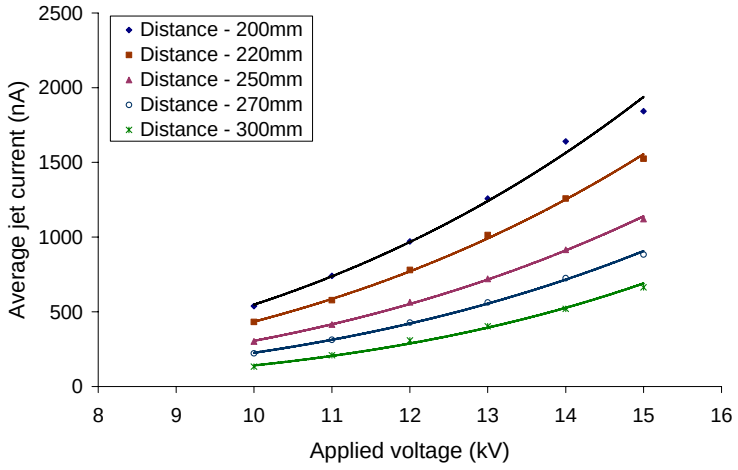


(b)

Fig. 5.11: Variation of average jet current with the application of high voltage to the needle of AWG 19 inner diameter (a) positive polarity (b) negative polarity.

power law relationship ( $I = kV^P$ ) of average jet current with increasing voltage for both positive and negative polarities. A comparison of constant values of power law behaviour in average jet current for both positive and negative polarities is shown in Table 5.4. As shown in Fig. 5.12, the average jet current is always higher in the case of negative polarity compared to the case of positive polarity at all the respective voltages. This is, in fact, a highly interesting observation to investigate because it truly means higher charge flow occurs through the electrospinning jet with the application of negative voltage compared to the positive voltage.

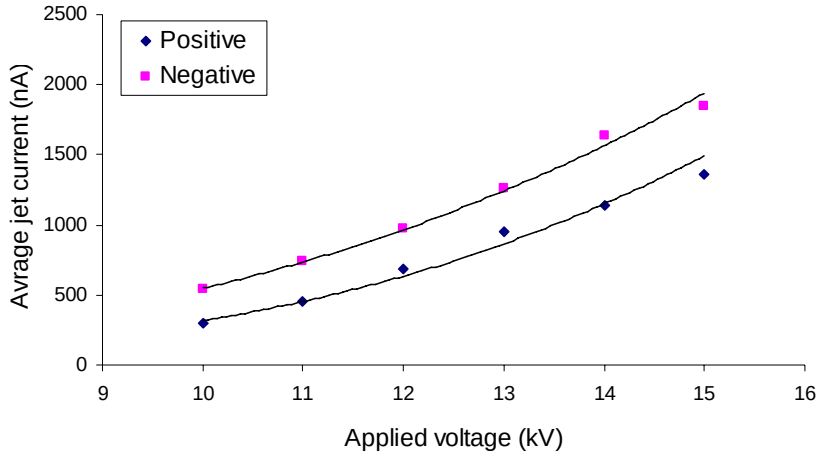


(a)

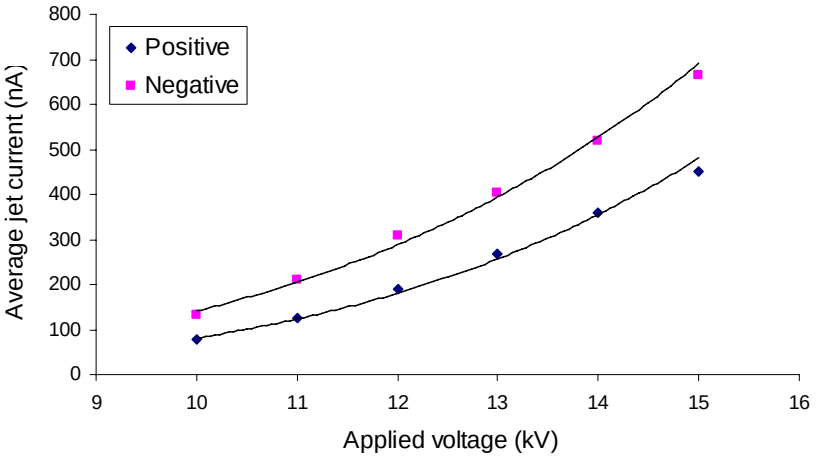


(b)

Fig. 5.12: Comparison in the average jet current with the application of positive and negative high voltage to the needle electrode: (a) electrode separation – 200mm. (b) electrode separation – 300mm.

Table 5.4: Comparison of constants of power law relationship for positive and negative polarities.

| Distance between the needle and the collector plate (mm) | Values of constant of proportionality ($k$) and exponent ($P$) | | | |
|---|---|---|---|---|
| | $k$ | | $P$ | |
| | Positive | Negative | Positive | Negative |
| 200 | 0.047 | 0.418 | 3.830 | 3.117 |
| 220 | 0.043 | 0.309 | 3.776 | 3.148 |
| 250 | 0.012 | 0.174 | 4.128 | 3.245 |
| 270 | 0.015 | 0.083 | 3.955 | 3.431 |
| 300 | 0.003 | 0.017 | 4.391 | 3.918 |

#### 5.4.1.2 Behavior of the Straight Jet Portion

Fig. 5.13 shows the relationship between the average length of the straight jet portion and the applied voltage with the application of positive voltage. As illustrated, the length of the straight jet portion increases with increased applied voltage linearly for all the distances between the needle electrode and the collector plate. However, it was not possible to measure the length of the straight jet portion with the application of negative voltage since it was highly unstable and vibrant. Use of a high speed camera may help to capture the straight jet portion with the application of negative high voltage. Fig. 5.14 (a) and (b) show the photographs of straight jet portion with the application of positive and negative DC voltages respectively.

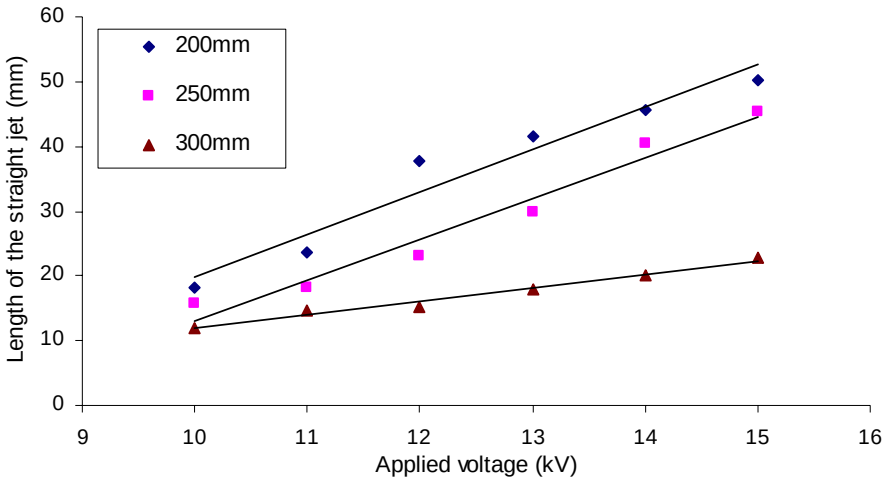


Fig. 5.13: Average length of the straight jet portion with the application of positive polarity to the needle electrode.

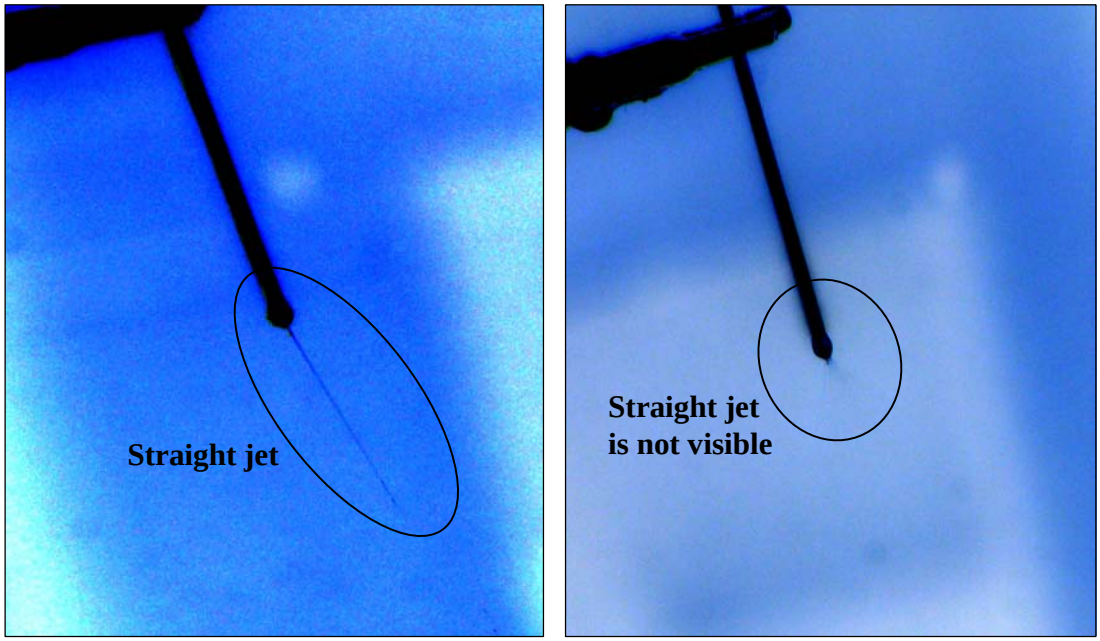


(a) (b)

Fig. 5.14: Photographs of the straight jet portion: (a) positive polarity (b) negative polarity.

#### 5.4.1.3 Behavior of the Whipping Jet

The behaviour of the whipping jet is investigated by measuring the area of the collected nanofibres. MATLAB image processing toolbox was used to calculate the deposition area of collected fibres and the results are presented in pixels. As shown in Fig. 5.15 (a), the deposition area increases with increasing voltage, both positive and negative polarity. Moreover a larger collection area can be observed with the application of negative polarity compared to positive polarity. As shown in Fig. 5.12, the average jet current is higher in the case of negative polarity and it means that the jet carries more charge in the case of negative polarity. This causes jet to elongate and traverse more in lateral directions resulting larger deposition area. However, as illustrated in Fig. 5.15 (b) and (c), if the electric field strength is less than 0.04kV/mm, a larger deposition area can be observed in the case of positive polarity compared to negative polarity. The results are discussed in more detail in Chapter 7.

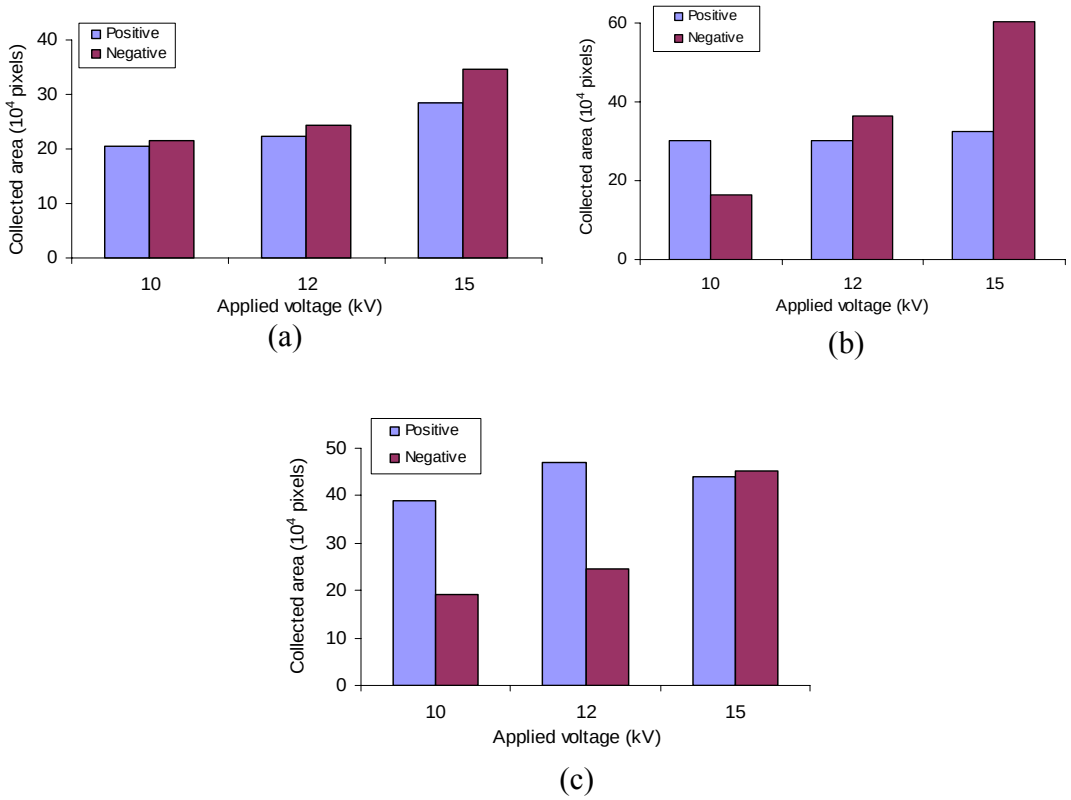


Fig. 5.15: Deposition area of the collected fibres for different distances between the needle tip and the collector plate: (a) gap distance – 200mm (b) gap distance – 250mm (c) gap distance – 300mm.

#### 5.4.1.4 Characteristics of Fibre Morphology

Each diameter of about 50 nanofibres was examined using image processing software and an average fibre diameter was calculated. As expected, thinner fibres were obtained with the application of negative polarity compared to the positive polarity. This means that the stretching of the electrospun jet is higher in the case of negative polarity with compared to the positive polarity. The results are presented in Table 5.5.

Table 5.5: Average fibre diameter of electrospun fibres with the application of positive and negative voltages to the needle electrode.

| Polarity | Voltage (kV) | Average fibre diameter of electrospun fibres for different distances between the needle tip and the collector plate (nm) | | |
|---|---|---|---|---|
| | | 200mm | 250mm | 300mm |
| Positive | 10 | 366 | 319 | 301 |
| | 15 | 353 | 410 | 397 |
| Negative | 10 | 263 | 235 | 244 |
| | 15 | 380 | 374 | 330 |

### 5.4.2 AC and Pulse Voltages

Electrospinning was tried using 60 Hz AC voltage; however, it was not able to electrospin continuous nanofibres. A straight jet formation and whipping jet region were not visible with the application of 60 Hz; hence it mostly produced droplets than fibres. High voltage square pulses were also tried to fabricate and chop nanofibres. A square pulse generator built in the laboratory was used for experiments. It was observed that the parameters such as the pulse width, the duty ratio, pulse-on voltage, and pulse-off voltage significantly affect on the electrospun jet, the droplet formation, and the diameter and bead formation of nanofibres [102, 103].

## 5.5 Effects of Electric Field on Multi-Needle Systems

Single-needle systems have been used in electrospinning experimental research; however, the low fluid throughput in fibre production has industrial limitations. To meet a high liquid throughput requirement, several multi-jet schemes have recently been tested. The main drawback of the currently existing schemes is the deterioration of the local electric field at the needle tip due to the presence of other needles in the arrangement. This results in non-uniform fiber formation and the requirement of higher voltage for jet initiation. In this section, the distortion of the electric field in multi-needle schemes and its effects on the electrospinning process has been investigated.

### 5.5.1 Experimental Results

#### 5.5.1.1 Behavior of the Straight Jet Portion

Fig. 5.16 shows the variation in vertical angle of the straight jet portion ($\theta$) with the space in 2-needle arrangements that varying from 10 mm to 100 mm for applied voltages of 10 kV, 15 kV, and 20 kV. Although the angle $\theta$ initially decreases sharply for needle spacings less than 40 mm, thereafter, the variation is not much significant.

Table 5.6 presents the variation in the vertical angle of the straight jet portion of multiple needle arrangements for a range of needle spacing. It can be observed that, with an increase in voltage, the vertical angle increases, and in contrast, an increase in needle spacing produces a decrease in the vertical angle. Most importantly, the results show that the vertical angle of the straight jet portion increases with an increase in the number of needles in the needle arrangement. A similar observation was reported in [38].

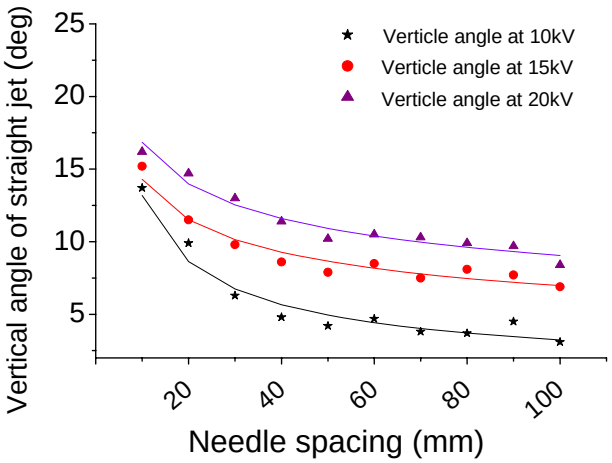


Fig. 5.16: Variation in the vertical angle of the straight jet portion of a 2-needle arrangement for different needle spacing.

Table 5.6: Vertical angle of the straight jet portion of the jets for the two end needles of each needle arrangement.

| Needle Arrangement | Applied Voltage (kV) | Vertical Angle of Straight Jet in Degrees | | |
|---|---|---|---|---|
| | | 10 mm spacing | 20 mm spacing | 30 mm spacing |
| 2-Needle | 10 | 13.7 | 9.9 | 6.3 |
| | 15 | 15.2 | 11.5 | 9.8 |
| | 20 | 16.2 | 14.7 | 13.0 |
| 3-Needle | 10 | * | 10.3 | 6.8 |
| | 15 | * | 13.4 | 11.5 |
| | 20 | 14.2 | 17.6 | 14.8 |
| 4-Needle | 10 | * | * | * |
| | 15 | 17.4 | 11.7 | 9.8 |
| | 20 | 18.8 | 14.3 | 13.9 |

* There is no electrospinning due to the field deterioration and hence the vertical angle can not be calculated.

#### 5.5.1.2 Behavior of the Jet Current

The jet current determines the charge that is carried by the electrospinning jet during the electrospinning process, as represented by Equation (5.1) [94];

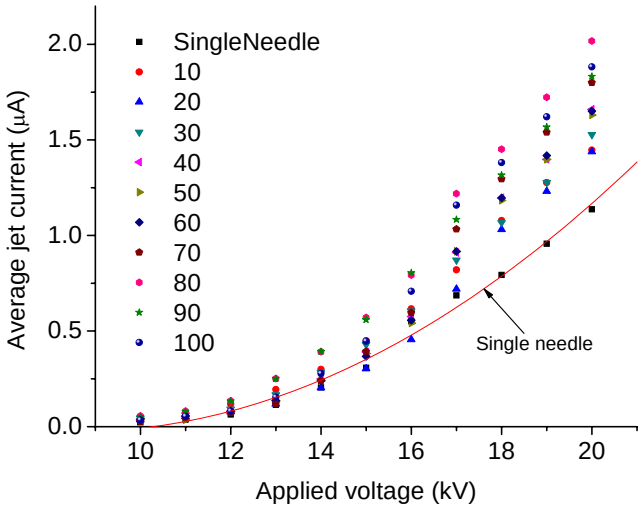


Fig. 5.17: Variation in the average jet current with an increase in applied voltage for a 2-needle arrangement and different needle spacing in millimetres. For comparison, the test data for a single-needle arrangement is also shown.

$$I = \pi R^2 KE + 2\pi R \upsilon \sigma \tag{5.1}$$

where $I$ is the average total current, $E$ is the electric field, $K$ is the conductivity of the liquid, $R$ is the radius of the electrospun jet, $\upsilon$ is the velocity of the jet, and $\sigma$ is the surface charge density of the jet. The jet current is therefore an appropriate parameter for evaluating the electrospinning process and the diameter of the fibre. Fig. 5.17 and Fig. 5.18 show the variations in the average jet current for a single jet and multi-jet arrangements for a range of applied voltages. The jet currents of single needle arrangement as well as multi-jet arrangements shown in figures approach power law behavior ($I=kV^P$) of an average jet current $I$ as a function of the applied voltage $V$. In addition, it is observed that the value of exponent $P$ lies between 5.4 and 6.5. Theron et al. [82] and Demir et al. [55] have also observed that the power law behaviour for a single needle arrangement. The authors have also reported that the value of exponent $P$ would be between 2.4 and 3.3 for a PEO solution. It can be observed that the required minimum voltage to start the electrospinning increases considerably with the addition of more needles to the needle arrangement. This effect can be observed in the behaviour of the jet current, that is, the circled data points in Fig. 5.18 (a) and (b), which represent the zero current at low voltages since there is no jet or fibre formation during this period. Furthermore, as shown in Fig. 5.17 and Fig. 5.18, the total jet current with multi-jet schemes is not multiples of the jet current in the single needle scheme. Moreover, this behaviour is dominant at lower voltages.

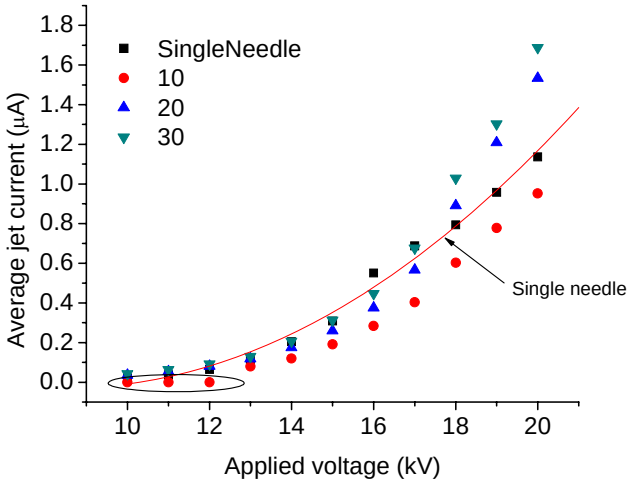


(a)

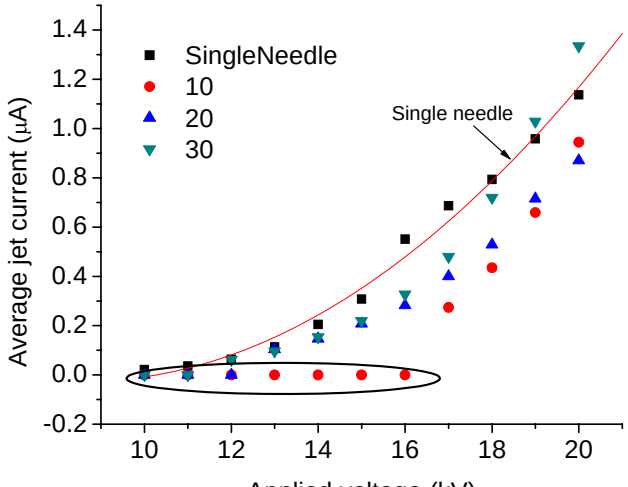


(b)

Fig. 5.18: Variation in the average jet current with an increase in applied voltage for different needle spacing in millimeters: (a) 3-needle arrangement. (b) 4-needle arrangement. For comparison, the test data for a single-needle arrangement is also shown. The circled data points represent the zero current at low voltages.

#### 5.5.1.3 Characteristics of the Whipping Jet

Quantitative and qualitative analysis of the area of the collected electrospun fibres is very important and can be used effectively to determine the behaviour of the jet and the angle of the looping envelope during the fibre spinning. Fig. 5.19 is a schematic of the electrospinning process that shows the angle of the looping envelope. This parameter is very important because one can determine the traversed jet path

from it and hence obtain an estimate of the rate of solvent evaporation, and the diameter, and morphology of the fibre.

Fig. 5.20 shows the differences in the collected area of the electrospun fibres for different needle arrangements. As illustrated, the collected area for a single-needle arrangement is almost circular whereas, when the number of needles in the arrangement is increased, the shape of the collected area changes from circular to elliptical. A similar observation was reported in [38].

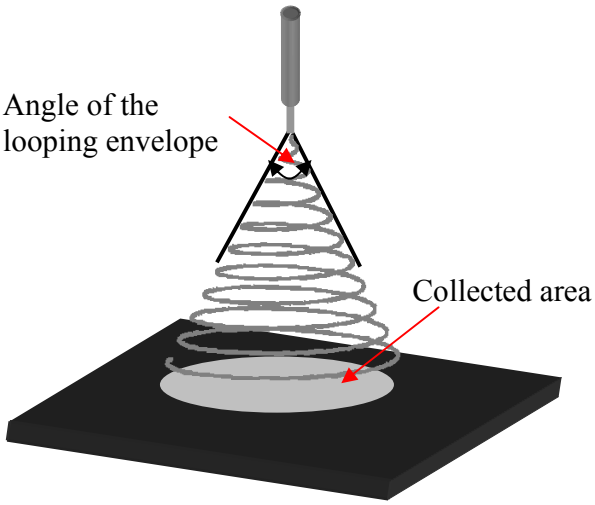


Fig. 5.19: Schematic of the electrospinning process.

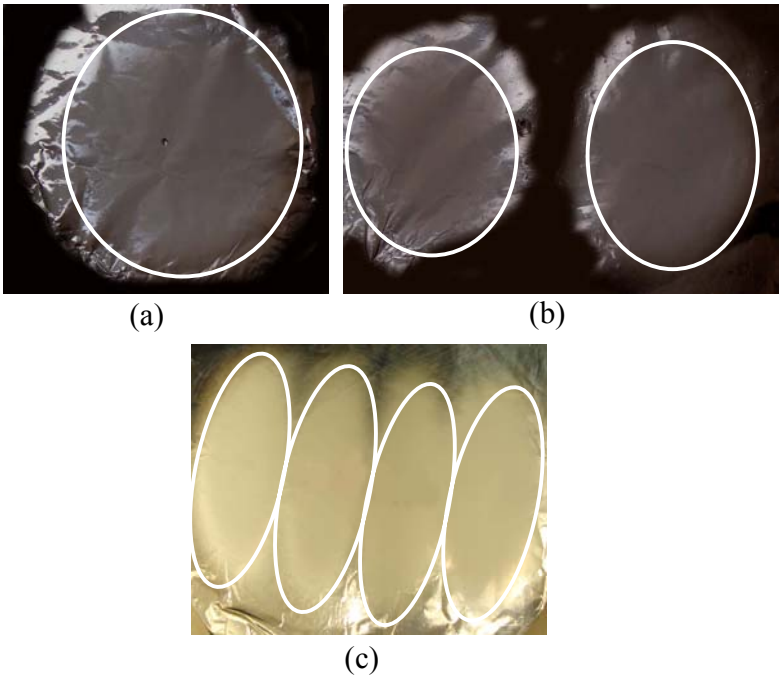


Fig. 5.20: Photographs of the fibre collection area for single-needle and multi-jet arrangements: (a) Single-needle arrangement, (b) 2-needle arrangement, and (c) 4-needle arrangement.

#### 5.5.1.4 Characteristics of Fibre Morphology

Fig. 5.21 shows the variation in the average fibre diameter with the increase of spacing between the two needles. It was observed that the diameter of the fibre with a 2-needle arrangement is thinner than that of the fibre produced using a single-needle system.

Fig. 5.22 shows the variation in the average fibre diameter for needle arrangements with 1, 2, 3, and 4 needles. The diameter of the fibre decreases with the increase in the number of needles in the arrangement. In addition the non-uniformity of the fibres has also increased with the increase in the number of needles in the needle arrangement.

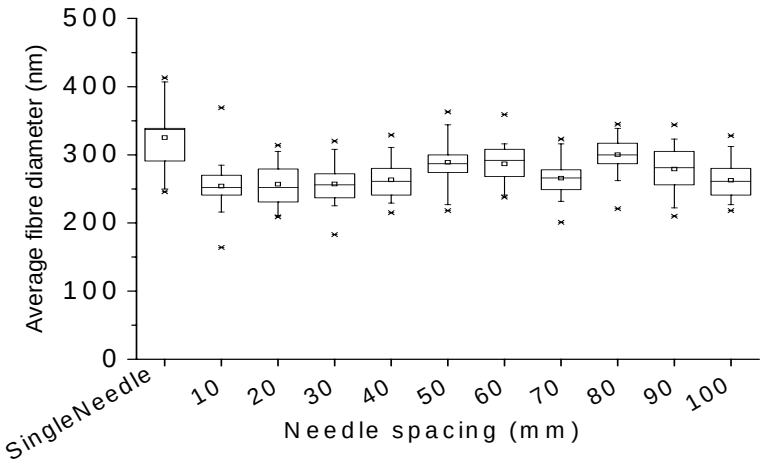


Fig. 5.21: Variation in the average fibre diameter of the electrospun fibres for different needle spacing of 2-Needle arrangement at 15kV. For comparison, the test data for a single-needle arrangement is also shown. The average fibre diameter is represented by the cross inside the box; the median is represented by the horizontal line inside the box; the 25$^{th}$ and 75$^{th}$ percentiles are represented by the horizontal lines of the box. Error bars above and below the box indicate the 90$^{th}$ and 10$^{th}$ percentiles. The crosses above and below the box represent the maximum and the minimum of the sample respectively.

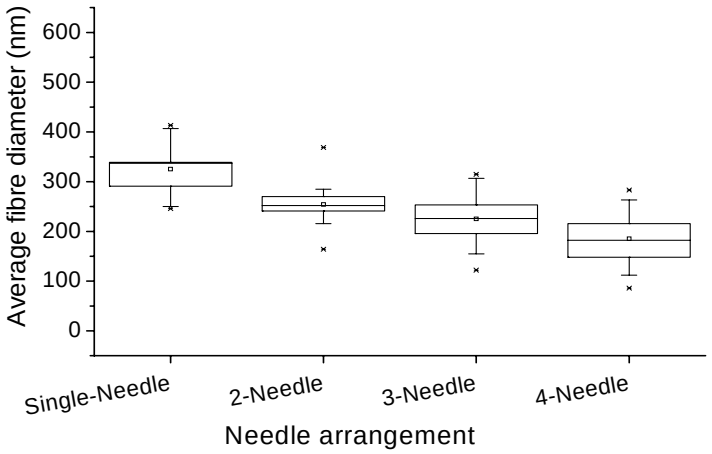


Fig. 5.22: Variation in the average fibre diameter of electrospun fibres for a range of needle arrangements at 15 kV. The average fibre diameter is represented by the cross inside the box; the median is represented by the horizontal line inside the box; the 25$^{th}$ and 75$^{th}$ percentiles are represented by the horizontal lines of the box. Error bars above and below the box indicate the 90$^{th}$ and 10$^{th}$ percentiles. The crosses above and below the box represent the maximum and the minimum of the sample respectively.

# Chapter 6

# Effects of Conductivity and Ionic Carriers

## 6.1 Introduction

As discussed in Chapter 2, the parameters affecting the electrospinning process and the fibre morphology can be broadly classified into three main categories, namely (1) solution properties, (2) processing conditions, and (3) ambient conditions [1]. Previous studies have revealed that the properties of polymer solution play a major role affecting the process of electrospinning and morphology of nanofibres. The effects of some of these parameters on the process of electrospinning and morphology of nanofibres have been investigated and reported in recent past [1-50]. This includes molecular weight of the polymer, viscosity of the solution, and polymer concentration in the solution. However, a little research has been done to investigate and understand the effects of conductivity and ionic carries in the solution on the electrospinning process and fibre morphology. Thus, in this chapter, a detailed investigation is done to examine the effects of conductivity and ionic carriers in the solution on the electrospinning process and hence, nanofibre morphology.

## 6.2 Effects of Conductivity

### 6.2.1 Preparation of Materials

PEO with an average molecular weight of 600,000Da purchased from Aldrich® was chosen to prepare the solutions. PEO fibres were electrospun using 5 % (w/w) concentrations of PEO in de-ionized water. Sodium chloride (NaCl) purchased from Aldrich® was added to the prepared PEO solutions to change the conductivity. The composition of prepared samples is tabulated in Table 6.1. All samples were stored at room temperature, and electrospinning experiments were conducted at room temperature and ambient air.

Table 6.1: The characterization of solutions.

| Sample number | $S_0$ | $S_1$ | $S_2$ | $S_3$ | $S_4$ | $S_5$ | $S_6$ | $S_7$ | $S_8$ | $S_9$ | $S_{10}$ | $S_{11}$ | $S_{12}$ |
|---|---|---|---|---|---|---|---|---|---|---|---|---|---|
| PEO (g) | 5 | 5 | 5 | 5 | 5 | 5 | 5 | 5 | 5 | 5 | 5 | 5 | 5 |
| Water (g) | 95 | 95 | 95 | 95 | 95 | 95 | 95 | 95 | 95 | 95 | 95 | 95 | 95 |
| NaCl (g) | 0.00 | 0.05 | 0.10 | 0.15 | 0.20 | 0.25 | 0.50 | 0.75 | 1.00 | 1.25 | 1.75 | 2.00 | 2.50 |

### 6.2.2 Characteristics of Solution Parameters

Fig. 6.1 shows how the conductivity of the solution varies with increase in salt concentration. As expected, the conductivity of the samples shows a linear increase that corresponds to the levels of salt concentration. A 5 % (w/w) PEO/water solution has an initial conductivity of 7.68 μS/mm, which is increased up to 300 times with the addition of 2.5 g of salt.

PEO is a polymer that has shear-thinning characteristics. As explained in Chapter 4, a rheometer was therefore used in order to determine its specific shear-thinning characteristics, and the results are shown in Fig 6.2. The behavior of the dynamic viscosities of the samples closely matches the power law relationship $\left(y = ax^{P}\right)$, with the value of $R^2$ being between 0.9992 and 1. The values of parameters *a* and *P* lie between (4.406) – (5.555) and (-0.5541) – (-0.585), respectively. Therefore, the variation within the viscosities of the samples is negligible.

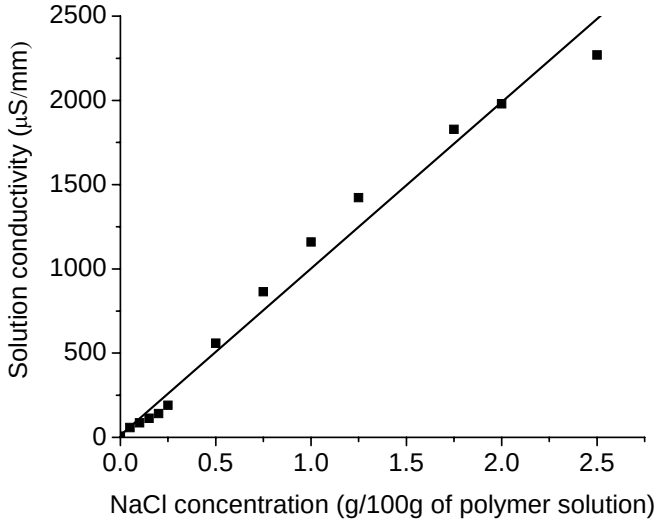


Fig. 6.1: Variation in the conductivity of the solutions with increase in salt concentration.

Fig. 6.3 illustrates how the surface tension and viscosity of the solution change when the conductivity is increased. The speed of the electrospun jet is several times the speed of sound [18], so the viscosity values presented here have therefore been calculated using a shear rate corresponding to 10 times the speed of sound (340.29m/s). As shown in Fig. 6.3, the variations that occur in the surface tension and viscosity when the conductivity of the solution is increased are negligible. It can therefore be concluded that the effects of viscosity and surface tension of the solution on the electrospinning process and fibre morphology can be ignored in our experiments when the conductivity is varied.

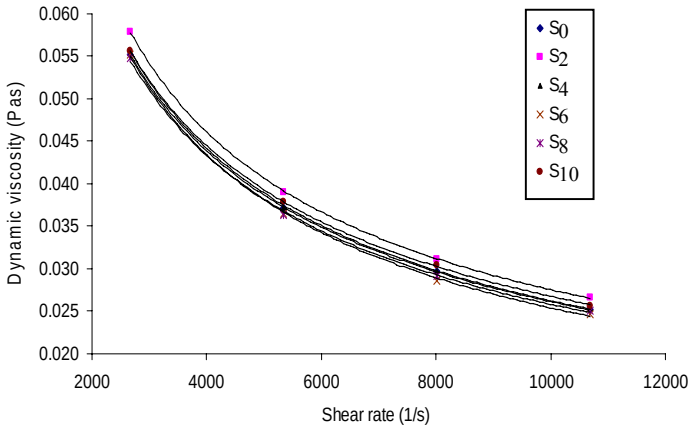


Fig. 6.2: Representation of the shear-thinning characteristics of different polymer samples.

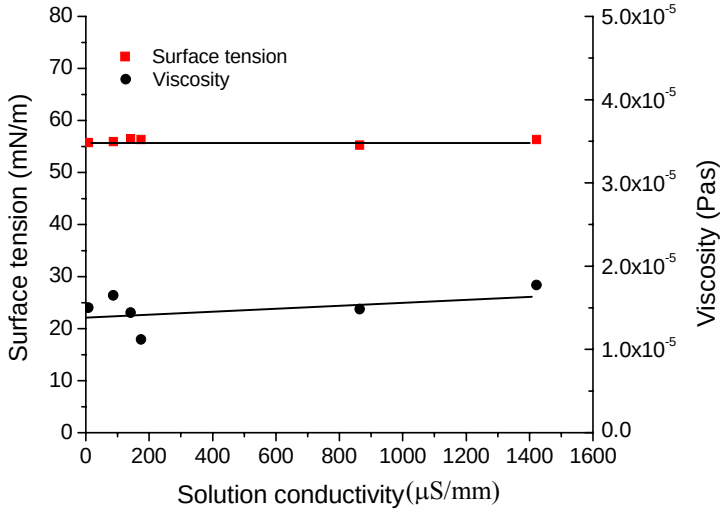


Fig. 6.3: Variation in surface tension and viscosity with increase in the conductivity of polymer solutions.

### 6.2.3 Experimental Results

#### 6.2.3.1 Behavior of the Average Jet Current

Fig. 6.4 shows how the average jet current varies with the conductivity of the solution. The jet current is directly proportional to the charge carried by the jet, and the volume charge density ($\rho_{vc}$) can be

calculated using Equation 6.1 [82];

$$\rho_{vc} = \frac{I}{Q} \tag{6.1}$$

where $I$ is the jet current, and $Q$ is the volumetric flow rate. In most of the studies reported in the literature, the electrospinning process has been characterized according to Saville's leaky dielectric model, which considers fluid motion in electric fields to be due to the charges on the surface of the fluid [12, 13, 18, 93, 94, and 104]. However, the fluid jet evaporates, stretches, bends, and sometimes branches during electrospinning, and therefore, the density of the surface charge varies along the jet. As a result, the density of the surface charge of the jet is more dependent on the position of geometry and the specific case than on the initial volume charge density. Nonetheless, the surface charge density ($\sigma$) can be determined approximately using Equation 6.2 [82].

$$\sigma = \frac{\rho_{vc} d}{4} \tag{6.2}$$

where $d$ is the measured diameter of the electrospinning jet close to the tip of the Taylor cone.

As shown in Fig. 6.4, irrespective of the applied voltage, the jet current increases exponentially $\left(I = ae^{bK}\right)$ with increase in the conductivity of the solution until a maximum value is reached. However, the rate of increase in the jet current rises when the applied voltage between the needle tip and the target

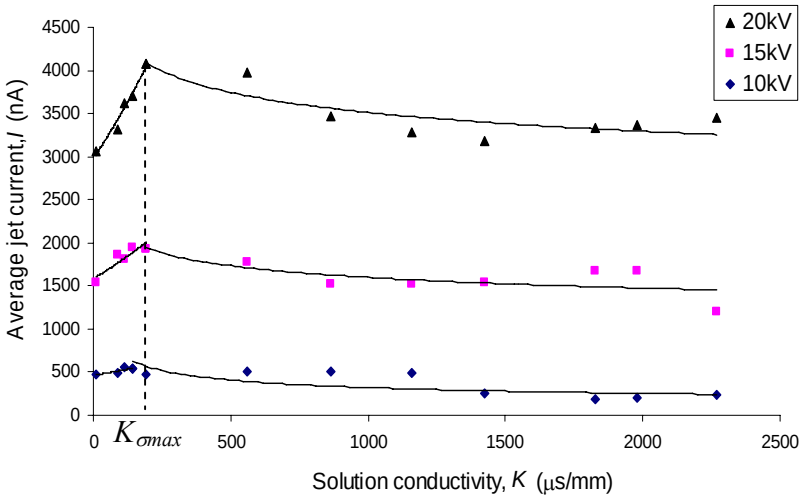


Fig. 6.4: Variation in the average jet current with the conductivity of the solution, for a range of voltages applied with a 200 mm electrode spacing.

is augmented. The maximum current occurs at a conductivity value of $K_{\sigma max}(K_{\sigma \max} \approx 191.5 \mu S/mm)$, which induces the maximum surface charge density ($\sigma_{max}$) at the jet surface. After reaching its maximum value, the jet current begins to decrease slightly with an increase in the conductivity of the solution.

### 6.2.3.2 Behaviour of the Average Fibre Diameter

Fig. 6.5 shows how the average diameter of the fibre varies with increase in the conductivity of the solution. The base PEO/water solution ($S_0$) results in the largest average fibre diameter during the experiments. Thereafter, the diameter of the fibre decreases with an increase in the conductivity of the solution. Table 6.2 shows the coefficient of variation (CV %) of fibre diameter on a relatively large number of measurements (~50). It also reveals that the uniformity of the fibre increases significantly with increase in the conductivity of the solution.

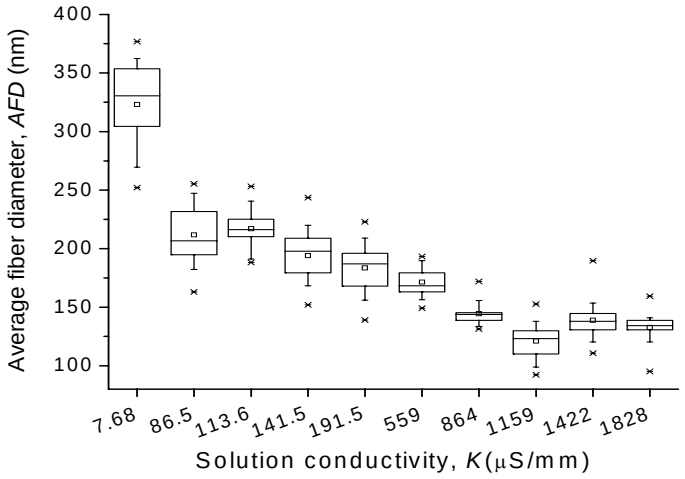


Fig. 6.5: Variation in the average diameter of the fibre with increase in the conductivity of the solution for a 15 kV voltage applied with a 200 mm electrode spacing. The average fibre diameter is represented by the cross inside the box; the median is represented by the horizontal line inside the box; the 25$^{th}$ and 75$^{th}$ percentiles are represented by the horizontal lines of the box. Error bars above and below the box indicate the 90$^{th}$ and 10$^{th}$ percentiles. The crosses above and below the box represent the maximum and the minimum of the sample respectively.

Fig. 6.6 shows a comparison of the variation in the jet current and the variation in the average diameter of the fibre (*AFD*) when the conductivity is increased. As shown in the figure, three distinct regions can be observed with respect to the variation in the jet current. In Region 1, the average electrospun jet current increases with the rise in conductivity. Fig. 6.7 (a) shows how the average

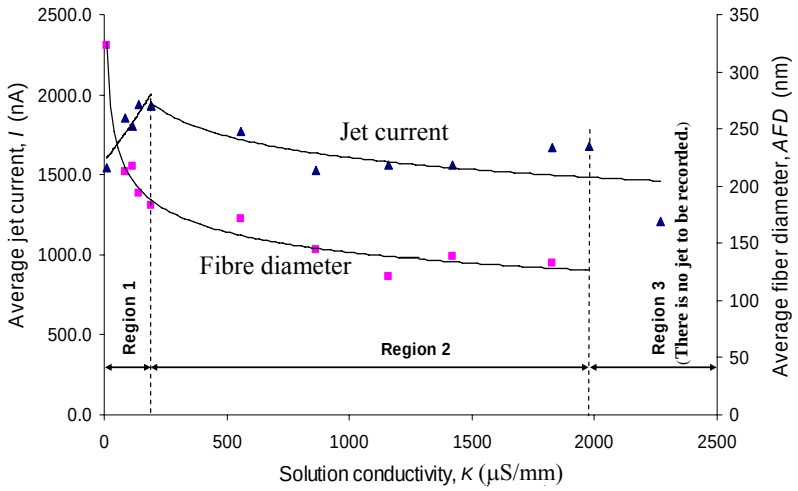


Fig. 6.6: A comparison of the behavior of the average jet current and the average diameter of the fibre with increase in the conductivity of the solution for a 15 kV voltage applied with a 200 mm electrode spacing.

Table 6.2: The coefficient of variation (CV) of fibre diameter.

| Conductivity (μS/mm) | CV % | Conductivity (μS/mm) | CV % |
|---|---|---|---|
| 7.68 | 11.27 | 559 | 7.41 |
| 86.5 | 11.04 | 864 | 7.18 |
| 113.6 | 8.31 | 1159 | 7.57 |
| 141.5 | 10.19 | 1422 | 7.11 |
| 191.5 | 9.76 | 1828 | 5.85 |

diameter of the fibre varies with the changing average jet current in Region 1. In this region, the average diameter of the fibre decreases with the increase in the jet current, which corresponds to the power law behavior $\left(AFD = 10^{10} I^{-2.3743}\right)$. As can be seen in Region 2 in Fig. 6.6, after reaching a maximum value, the average jet current decreases gradually with increase in the conductivity. Fig. 6.7 (b) indicates how the average diameter of the fibre varies with changes in the average jet current in Region 2. The relationship is linear: the average diameter of the fibre becomes thicker with increase in the average jet current. In the range of the conductivity values tested (i.e. in Regions 1 and 2 in Fig. 6.6), the average diameter of the fibre decreases when the conductivity is increased, and it matches the

power law behavior $\left(AFD = 459.3K^{-0.1699}\right)$ with an $R^2$ value of 0.9572. Finally, it can be observed that at high values of conductivity in Region 3, there is no jet or intermittent jet. Fibres can therefore not be formed at higher levels of conductivity.

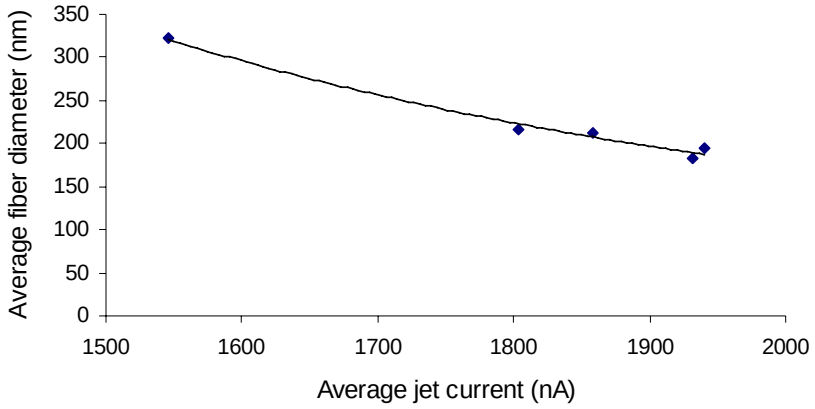


(a)

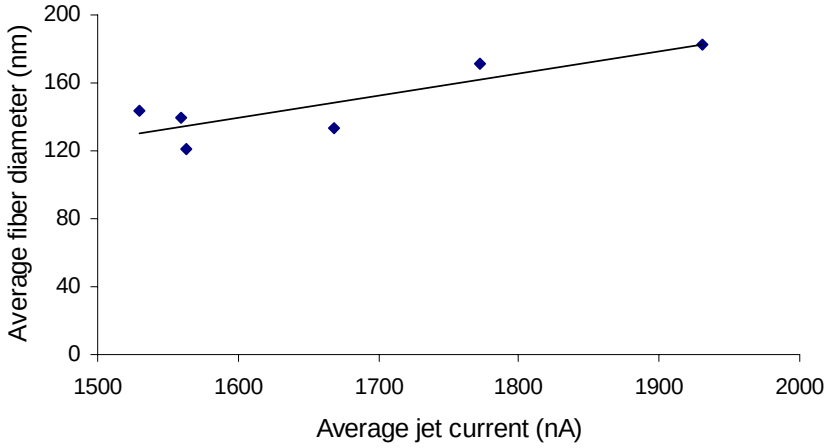


(b)

Fig. 6.7: Variation in the average diameter of the fibre plotted against the average jet current: (a) in Region 1 and (b) in Region 2.

#### 6.2.3.3 Effects on Fibre Morphology

In addition to changes in the diameter of the fibre, alterations in the morphology of the fibre can also be observed when the conductivity of the solution is increased. The addition of NaCl to the solution results

in the formation of protrusion-like objects on the surface of the fibre, as shown in Fig. 6.8. Both their size and numbers expand when the concentration of NaCl is increased. Enlarged pictures of the fibres that show the protrusions are shown in Fig. 6.9.

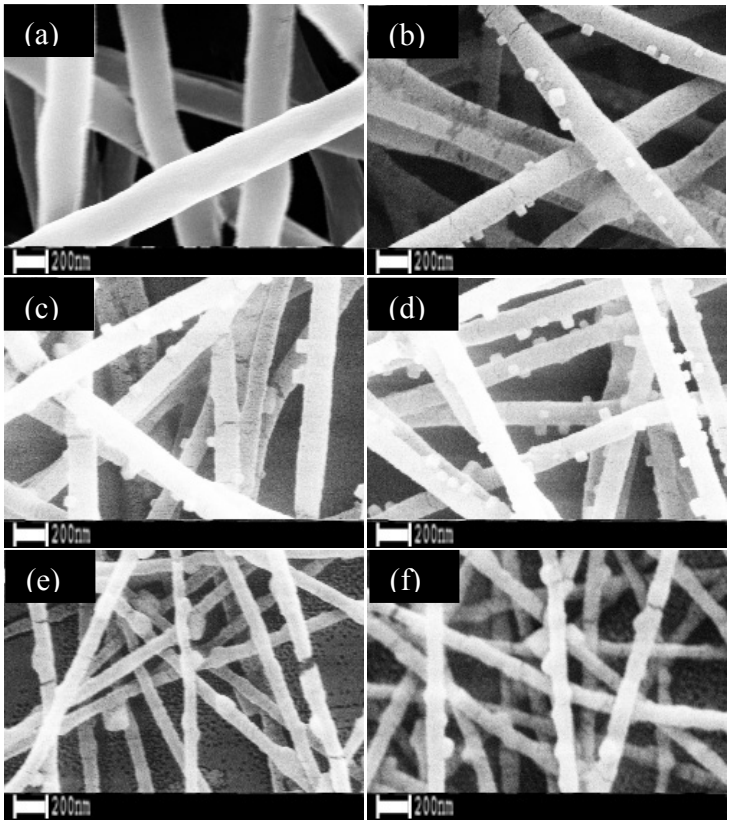


Fig. 6.8: SEM images of samples of electrospun PEO fibres for a selected range of conductivities: (a) $S_0$, (b) $S_2$, (c) $S_4$, (d) $S_6$, (e) $S_9$, and (f) $S_{11}$.

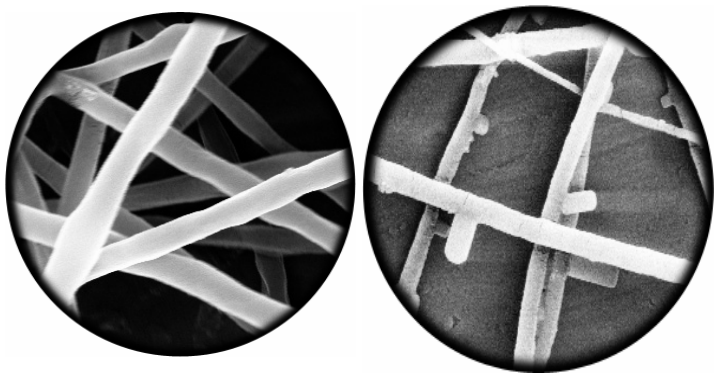

(a) (b)

Fig. 6.9: Comparison of fibre morphologies: (a) sample without NaCl and (b) sample with NaCl.

#### 6.2.3.4 Effects on the Electrospinning Process

The formation of multi-jets at the droplet with increase in the conductivity of the solution is shown in Fig. 6.10. The probability of ejecting multi-jets increases with increase in the conductivity. A similar observation was made by Koombhongse et al. when they attempted to electrospin 20% Poly(2-hydroxyethyl methacrylate) in a 50:50 mixture of ethanol and formic acid [36].

Fig. 6.11 provides a comparison of the formation of the Taylor cone for two samples: one with low conductivity ($S_0$) and the other with very high conductivity ($S_{12}$). As shown in Fig. 6.11 (a), the fluid droplet at the tip of the needle of sample $S_0$ forms a Taylor cone with a semi-vertical angle of $49.3^0$ and the ejection of a fluid jet from the apex of the cone. However, the sample that has a very high conductivity fails to form a Taylor cone. Instead, it makes a sharper cone with a semi-vertical angle less than $40^0$, and no fluid jet is produced from its apex. When large-diameter needles are used for electrospinning, similar behavior can be observed for even moderate conductivities, such as 500μs/mm.

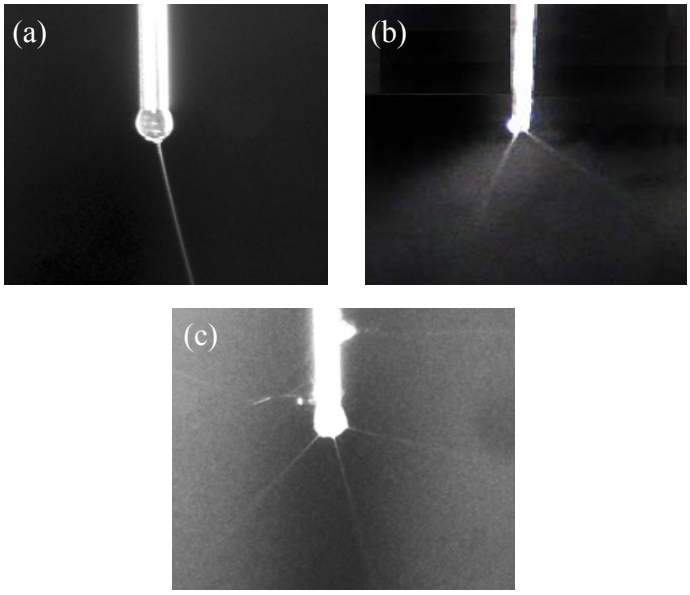


Fig. 6.10: Photographs of multi-jets produced at the fluid droplet with increase in the conductivity of the solution: (a) sample $S_0$, (b) sample $S_6$, and (c) sample $S_9$.

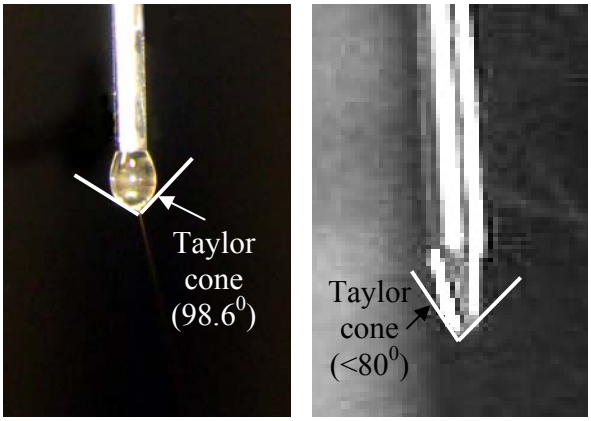


Fig. 6.11: Behavior of the fluid droplet at the tip of the needle: (a) sample $S_0$ and (b) sample $S_{12}$.

## 6.3 Effects of Ionic Carriers

The presence of surface charge on the fluid surface is essential for formation of Taylor cone, ejection of the jet from the Taylor cone, initiation of the instability, and stretching of the polymer jet during electrospinning. It ultimately determines the fibre morphology and diameter. The charge density at the fluid surface is greatly influenced by the amount and size of ionic carriers that present in the polymer solution. This section discusses the effects of ionic carriers on the electrospinning process and hence the fibre morphology by changing the type of ions and their concentration using PEO and polyacrylic acid (PAA) solutions.

### 6.3.1 Preparation of Materials

PAA with an average molecular weight of 450,000Da and PEO with an average molecular weight of 600,000Da purchased from Aldrich® were chosen to prepare the solutions. PAA fibres were electrospun using 5% (w/w) concentrations of PAA in de-ionized water. Similarly, PEO fibres were formed using 2.5% (w/w) concentrations of PEO in de-ionized water. Different salts (LiCl, NaCl, NaF, $NaHCO_3$, KCl, and CsCl) were used to investigate the effects of type of ion on the electrospinning process and fibre morphology. Three different concentrations (0.01mol, 0.001mol, and 0.0001mol) of above mentioned salts were added to the prepared PAA and PEO solutions and those ionic solutions were electrospun at room temperature and ambient air.

### 6.3.2 Characteristics of Polymer Solutions

Table 6.3 and 6.4 show how the conductivity of the solution varies with increasing concentrations of different salts. The conductivity of the solutions increases with the increase of level of salt concentration. A similar trend is observed in all the different salts. It is also observed that there is not much effect of type of salt on the conductivity of the solution.

Table 6.3: Variation in the conductivity of PEO solutions with varying salt concentrations for different types of salts.

| Type of salt | Conductivity of PEO solutions with the addition of different molar concentrations of salt ( μS/mm) | | |
|---|---|---|---|
| | 0.0001mol | 0.001mol | 0.01mol |
| LiCl | 15.0 | 66.2 | 683.0 |
| NaF | 19.7 | 66.9 | 650.0 |
| $NaHCO_3$ | 25.2 | 69.1 | 575.0 |
| NaCl | 19.7 | 82.8 | 707.0 |
| KCl | 17.4 | 74.7 | 690.2 |
| CsCl | 16.8 | 83.4 | 684.3 |

Table 6.4: Variation in the conductivity of PAA solutions with varying salt concentrations for different types of salts.

| Type of salt | Conductivity of PAA solutions with the addition of different molar concentrations of salt ( μS/mm) | | |
|---|---|---|---|
| | 0.0001mol | 0.001mol | 0.01mol |
| LiCl | 108.1 | 278.0 | 868.0 |
| NaF | 114.6 | 116.3 | 654.0 |
| $NaHCO_3$ | 116.3 | 91.2 | 712.0 |
| NaCl | 130.8 | 184.1 | 815.0 |
| KCl | 126.6 | 180.1 | 835.1 |
| CsCl | 131.2 | 187.1 | 782.4 |

Fourier transform infrared (FTIR) spectroscopy is used to characterize the molecular structure of polymer solutions with the addition of different types of salts. As shown in Fig. 6.12 and Fig. 6.13, the infrared absorption bands are dominant by $H_2O$ molecules in the regions from 3200 – 3800 $cm^{-1}$, which is mainly attributed to the asymmetric valence vibration $\nu_3$ of the monomer but it also involves $2\nu_2$ and the infra-red inactive symmetric valence vibration $\nu_1$ [105], and from 1600 – 1700 $cm^{-1}$, which is attributed to the $\nu_2$ bending mode of the water monomer [105], since the solution has more than 90% of water. Comparing with a FTIR spectrum of pure water, it is observed that the only dominant groups of

PAA/salt solutions are carbonyl group C=O (1718cm$^{-1}$) and coupling between in-plane O-H bending and neighboring carboxyl groups. Similarly, in PEO/salt solutions, the only dominant group is C-O (1000 – 1150 cm$^{-1}$) [106].

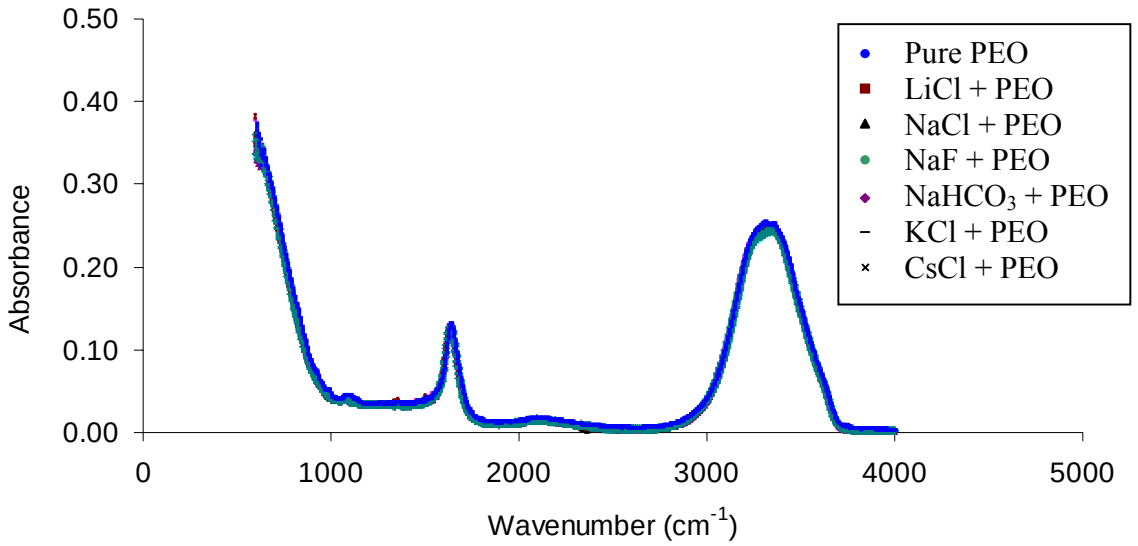


Fig. 6.12: FTIR spectrum of PEO solutions with the addition of different salts.

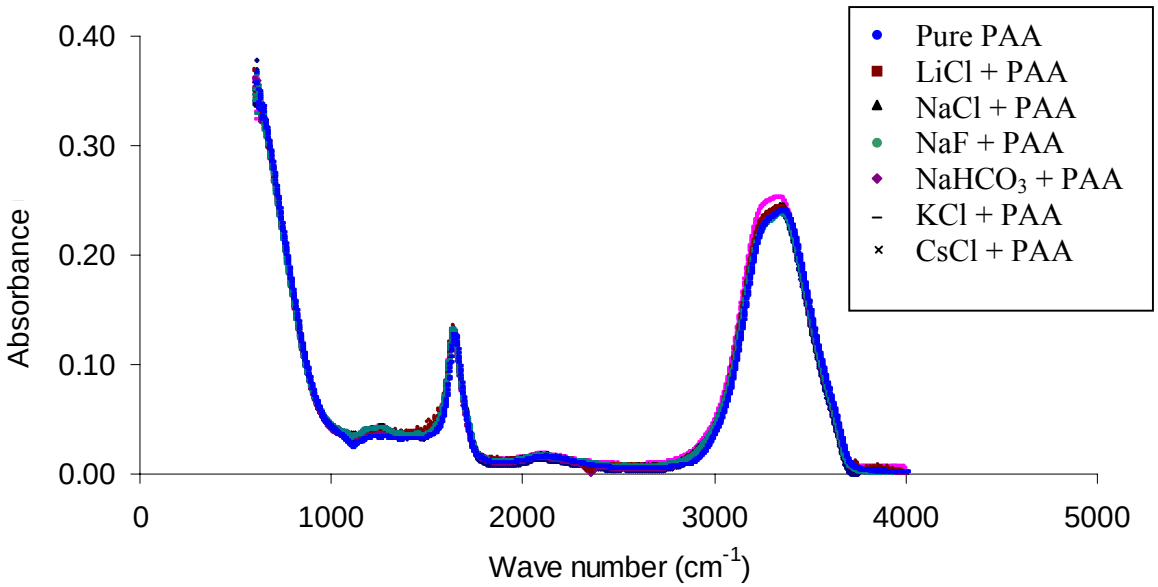


Fig. 6.13: FTIR spectrum of PAA solutions with the addition of different salts.

### 6.3.3 Experimental Results

#### 6.3.3.1 Effects on the Electrospinning Process

Different salts were used to inject ionic carriers of different sizes into aqueous polymer solutions. The salts including LiCl, NaCl, KCl, and CsCl form a chloride ion ($Cl^-$) and a positive ion ($Li^+$, $Na^+$, $K^+$, or $Cs^+$) when they dissolve in the solution. The size of these positive ions increases from $Li^+$ to $Cs^+$ respectively. On the other hand salts including NaF, $NaHCO_3$, and NaCl form a sodium ion ($Na^+$) and a negative ion ($F^-$, $HCO_3^-$, or $Cl^-$) in the solution. In this case, the size of the negative ions increases from $F^-$ to $Cl^-$ respectively. In addition, the experiments were conducted by increasing the salt concentration from 0.0001mol to 0.01mol. If the salt concentration is increased further up to 0.1mol, the electrospinning of the polymer solution was not possible.

Fig. 6.14 (a) and (b) illustrate the measured electrospun jet current of PAA and PEO solutions with the variation of type of salt and salt concentration. As expected, the jet current increases with the increase of salt concentration from 0.0001mol to 0.01mol. However, there is no noticeable difference among the jet currents of PEO solutions with the variation of type of salt. On the other hand, the electrospun jet current of PAA solutions vary with different salts. PAA solutions with higher concentration of NaF and $NaHCO_3$ decrease the jet current significantly compared to the other PAA solutions. This may be due to the reduced size of negative ions ($F^-$ and $HCO_3^-$) that ultimately decrease the total surface charge density on the fluid surface.

Fig. 6.15 illustrates the variation of the shape of the Taylor cone and straight jet portion of PEO and PAA solutions with the addition of different salt concentrations. A similar behaviour was observed with all the types of slat that were used in the experiment. As shown in the figure, a perfect Taylor cone can be observed at a low concentration of salt. However, the droplet size gets larger with the increase of salt concentration. In addition, polymer droplets were formed during the electrospinning process with the use of higher salt concentration. The increased salt concentration increases the conductivity of polymer solution that affects the tangential electric field along the surface of the fluid resulting in larger fluid droplets at the spinneret and fluid drops during the electrospinning process. If the salt concentration is increased further, multi-jets can be observed at the droplet. Finally, the electrospinning process stops at very high salt concentrations. In addition, the length of the straight jet portion of the electrospun jet significantly decreases with the increase of level of salt concentration as presented in Table 6.5 and 6.6. Furthermore, discontinues electrospinning could be observed at the higher salt concentrations in PAA solutions.

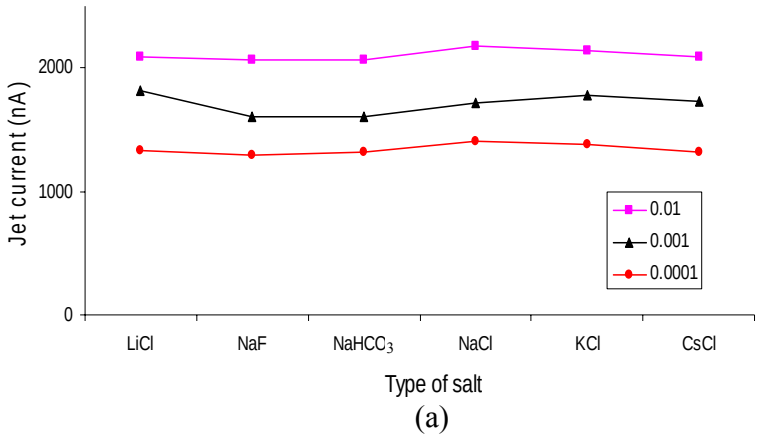


(a)

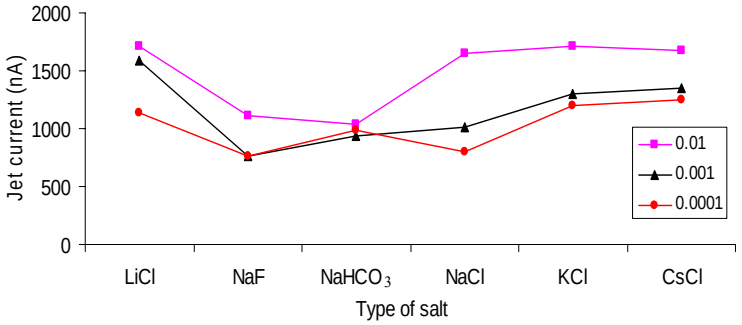


(b)

Fig. 6.14: Variation of jet current with the addition of different slats in different molar concentrations: (a) PEO solutions and (b) PAA solutions.

Table 6.5: Variation in the length of the straight jet portion of PEO solutions with varying salt concentrations for different types of salts.

| Type of salt | Length of the straight jet portion of PEO solutions with varying concentrations of salt (mm) | | |
|---|---|---|---|
| | 0.0001mol | 0.001mol | 0.01mol |
| LiCl | 21.81 | 23.93 | 1.18 |
| NaF | 20.33 | 21.68 | 0.44 |
| $NaHCO_3$ | 21.44 | 18.01 | 0.79 |
| NaCl | 19.56 | 17.59 | 0.48 |
| KCl | 21.43 | 22.01 | 1.68 |
| CsCl | 20.05 | 19.14 | 0.36 |

Table 6.6: Variation in the length of the straight jet portion of PAA solutions with varying salt concentrations for different types of salts.

| Type of salt | Length of the straight jet portion of PAA solutions with varying concentrations of salt (mm) | | |
|---|---|---|---|
| | 0.0001mol | 0.001mol | 0.01mol |
| LiCl | 7.14 | 5.58 | 3.94 |
| NaF | 6.92 | 7.84 | 6.99 |
| $NaHCO_3$ | 6.76 | 8.16 | 6.50 |
| NaCl | 6.93 | 6.47 | 4.52 |
| KCl | 4.89 | 5.48 | 2.90 |
| CsCl | 4.72 | 5.37 | 3.12 |

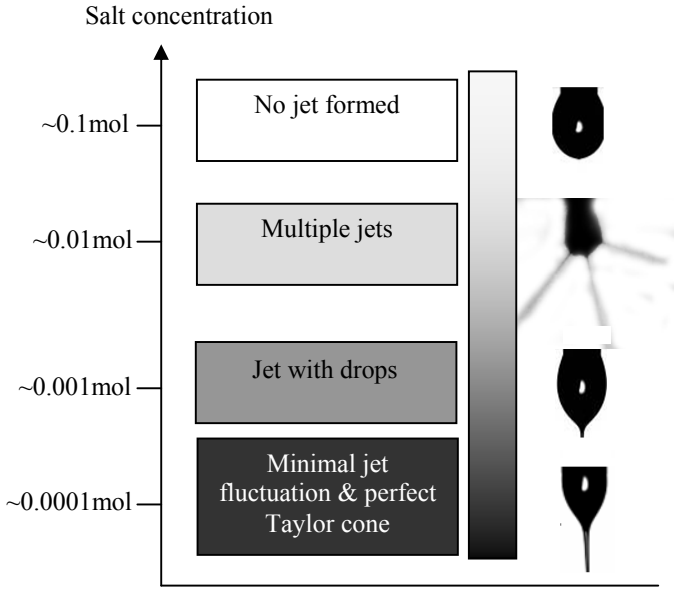


Fig. 6.15: A typical behaviour of the Taylor cone and the straight jet of the electrospun polymer solution for different salt concentrations.

The behaviour of the electrospun jet in the whipping region is investigated by measuring the diameter of the collected area. Fig. 6.16 (a) and (b) illustrate the variation of diameter of the collected area with the variation of type of salt and salt concentration. As shown in Fig. 6.16 (a), the diameter of the collected area does not show a considerable variation with the variation of type of salt and salt concentration of PEO solutions. However, PAA solutions with NaF, NaCl, and $NaHCO_3$ demonstrate larger collected areas due to the increased stretching during the electrospinning process. In contrast, multiple jets were observed at the salt concentration of 0.01mol of PEO solutions for all the types of salts; hence, multiple envelope cones could be observed.

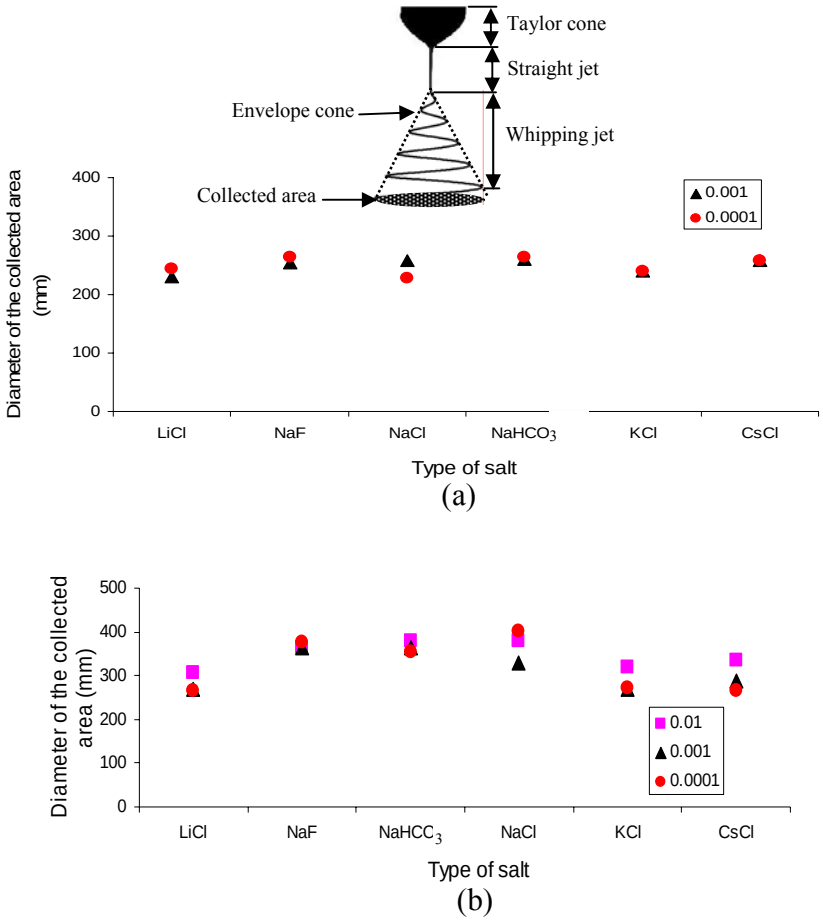


Fig. 6.16: Variation of the diameter of collected area with the addition of different slats in different molar concentrations: (a) PEO solutions and (b) PAA solutions.

### 6.3.3.2 Effects on Fibre Morphology

Fig. 6.17 illustrates the SEM images of electrospun PEO and PAA fibres for different types of salt and concentrations. As shown, the shape of the beads changes from spherical to spindle like shape with the increase of salt concentration. In addition, it can be observed that the bead density decreases and fibre uniformity increases with the increase of salt concentration. It was also observed that the lower diameter ions such as $Li^+$ form spindle like beads compared to the ions with larger diameters such as $K^+$ and $Cs^+$. The increase of salt concentration increases the number of ionic carriers in the solution. Therefore, the surface charge density increases at the fluid surface and that results greater stretching of the electrospun polymer jet converting the shape of the beads from spherical to spindle like transformation. Similarly, it can be observed that the smaller sized ions help for greater stretching of the electrospun polymer jet.

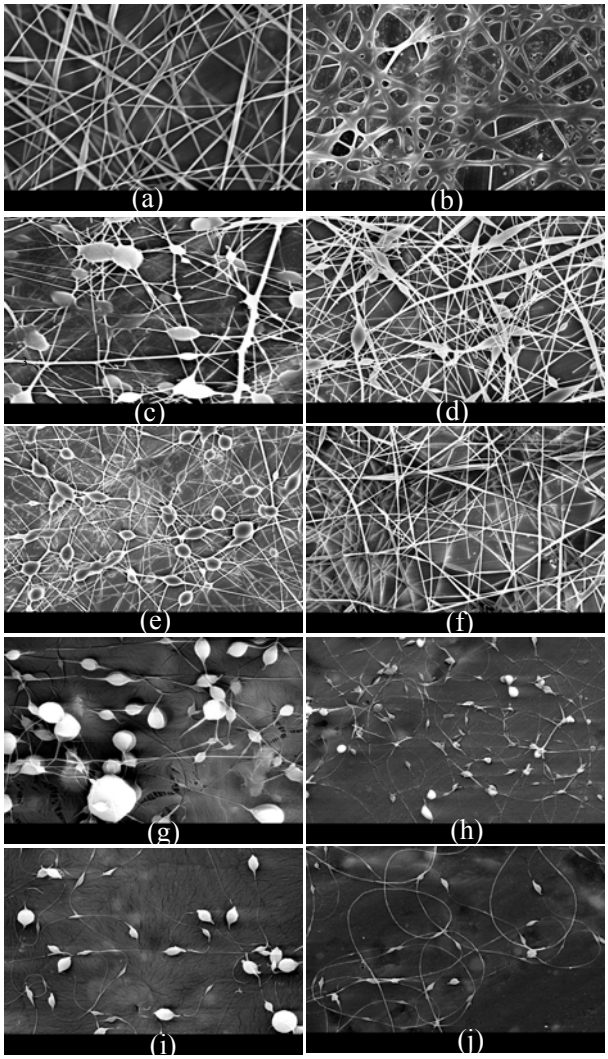


Fig. 6.17: Variation in the shape of the beads with increased salt concentration; with different salts: (a) 0.0001mol of LiCl in PAA, (b) 0.01mol of LiCl in PAA, (c) 0.0001mol of NaF in PAA, (d) 0.01mol of NaF in PAA, (e) 0.0001mol of NaCl in PAA, (f) 0.01mol of NaCl in PAA, (g) 0.0001mol of CsCl in PEO, (h) 0.01mol of CsCl in PEO, (i) 0.0001mol of NaF in PEO, and (j) 0.01mol of NaF in PEO.

Fig. 6.18 illustrates the different fibre morphologies that were obtained with the addition of different types of salt to the electrospinning polymer solutions. As shown in Fig. 6.18 (a), the addition of higher concentration of NaCl results in the formation of protrusions like objects on the fibre wall. On the other hand, as shown in Fig. 6.18 (c), the addition of 0.01mol of LiCl to PEO solutions forms fibres that have pores in the fibre. Furthermore, the addition of larger diameter ions such as $Cs^+$ and $K^+$ make segmented fibres during the electrospinning process. Fig. 6.18 (b) and (c) illustrate the fibres that were segmented during the electrospinning.

The average fibre diameters of electrospun PEO solutions are shown in Table 6.7 and 6.9. Similarly, Table 6.8 and 6.10 present the average fibre diameters of PAA solutions. The electrospun average fibre diameters of PEO solutions increase with the increase of salt concentration for salts including LiCl, NaCl, NaF, $NaHCO_3$, KCl, and CsCl. Similarly, the average fibre diameter of PAA solutions with salts of LiCl, NaCl, KCl, and CsCl increases with the increase of salt concentration. In contrast, the average fibre diameter of PAA solutions with salts of NaF and $NaHCO_3$ decreases with the increase of salt concentration. As shown in Table 6.7 and 6.8, it can be observed that the fibre diameter decreases with the use of salts of LiCl, NaCl, KCl, and CsCl respectively for both PEO and PAA solutions. Since all the experiments were conducted at similar conditions and the other major solution parameters such as viscosity and surface tension did not change significantly, this concludes that the higher salt concentrations and lower diameter positive ions form larger diameter fibres due to the increased stretching of the polymer jet. The increased stretching distributes the polymer material uniformly along the fibre avoiding bead formation, which finally results in larger diameter fibres. However, if the salt concentration increases further after reaching the uniform fibres, then the fibre diameter decreases with the increase of salt concentration. A contrast observation was done with increasing size of negative ions in the polymer solution. Table 6.9 and 6.10 present the average fibre diameter of PEO and PAA solutions with the addition of different types of slat that include NaF, $NaHCO_3$, and NaCl. It shows that

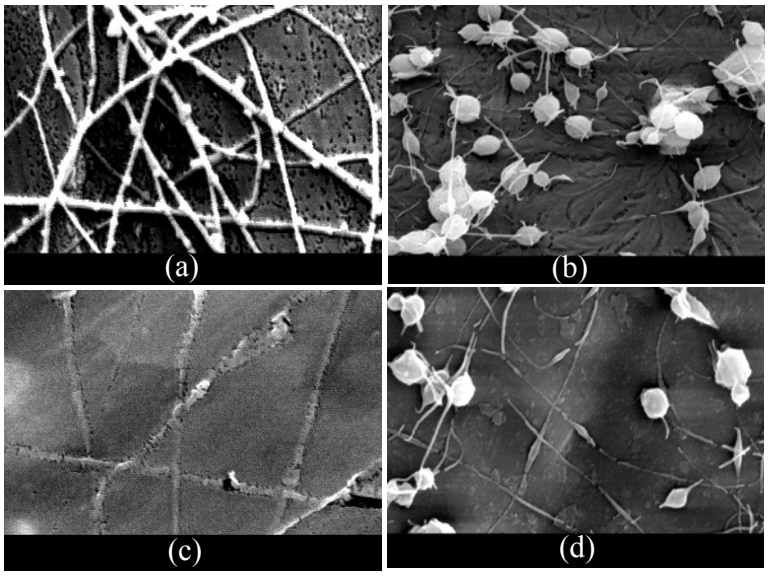


Fig. 6.18: SEM images of electrospun fibre morphologies: (a) 0.01mol of NaCl in PEO, (b) 0.001mol of CsCl in PEO, (c) 0.01mol of LiCl in PEO, and (d) 0.001mol of KCl in PEO.

the larger diameter negative ions such as $Cl^-$ help stretching of the electrospun fibre with compared to

the smaller negative ions such as $F^-$.

Table 6.7: Average fibre diameter of PEO solutions with the addition of different salt (LiCl, NaCl, KCl, and CsCl) concentrations.

| Type of salt | Average fibre diameter in different salt concentrations (nm) | | |
|---|---|---|---|
| | 0.0001mol | 0.001mol | 0.01mol |
| LiCl | 66±18 | 74±23 | 106±37 |
| NaCl | 77±17 | 95±22 | 98±24 |
| KCl | 45±15 | 49±9 | 104±13 |
| CsCl | 50±14 | 48±8 | 59±16 |

Table 6.8: Average fibre diameter of PAA solutions with the addition of different salt (LiCl, NaCl, KCl, and CsCl) concentrations.

| Type of salt | Average Fibre diameter in different salt concentrations (nm) | | |
|---|---|---|---|
| | 0.0001mol | 0.001mol | 0.01mol |
| LiCl | 161±90 | 192±50 | 221±93 |
| NaCl | 101±12 | 115±31 | 108±25 |
| KCl | 98±25 | 121±34 | 104±13 |
| CsCl | 72±17 | 108±13 | 99±18 |

Table 6.9: Average fibre diameter of PEO solutions with the addition of different salt (NaF, $NaHCO_3$, and NaCl) concentrations.

| Type of salt | Average fibre diameter in different salt concentrations (nm) | | |
|---|---|---|---|
| | 0.0001mol | 0.001mol | 0.01mol |
| NaF | 62±20 | 58±10 | 70±7 |
| $NaHCO_3$ | 54±7 | 55±12 | 60±15 |
| NaCl | 77±17 | 95±22 | 98±24 |

Table 6.10: Average fibre diameter of PAA solutions with the addition of different salt (NaF, $NaHCO_3$, and NaCl) concentrations.

| Type of salt | Average Fibre diameter in different salt concentrations (nm) | | |
|---|---|---|---|
| | 0.0001mol | 0.001mol | 0.01mol |
| NaF | 93±32 | 81±20 | 62±8 |
| $NaHCO_3$ | 103±23 | 85±30 | 60±15 |
| NaCl | 101±12 | 115±31 | 108±25 |

## 6.4 Charge Modifier

As presented in the above sections, leaky dielectric polymer solutions have the characteristics of quickly conducting the charges to the surface from the interior and the ability to sustain the electric field tangential to the jet surface. Therefore, it is relatively easier to electrospin those polymer solutions. However, perfect dielectric solutions, which have no ability to conduct the charges from inside to the fluid surface, or highly conductive polymer solutions, which do not have the ability to sustain the electric field tangential to the fluid surface, are very difficult to electrospin. This section describes a novel method of electrospinning for conductive polymer solutions without adding a supportive polymer to make polymer blends. The method is demonstrated by using sodium alginate which is a biopolymer that cannot electrospin alone due to its high electrical conductivity. Furthermore, the method can be applicable to polymers with low conductivity, like silicone rubber. Appendix D illustrates the molecular structures of sodium alginate (SA) and silicone rubber that were used in the experiments.

Fig. 6.19 illustrates the modified experimental setup that was used to perform the electrospinning experiments using insulating and highly conductive polymer solutions. Polymer solutions were fed through a syringe needle arrangement at a constant rate of 0.05 ml/min from a syringe pump, resulting in the formation of a drop of polymer solution at the needle tip. A needle of AWG of 19 inner diameter was used and Spellman high voltage DC power supply was used to apply the high voltage between the needle and the collector plate. The plate was heated during the electrospinning of silicone rubber for faster curing.

The needle was mounted vertically above the collector plate. A container filled with a solvent, which is named as the “charge modifier”, was used to hold the solvent that surrounds the needle tip during the electrospinning as shown in Fig. 6.19. A suitable solvent, which possesses leaky dielectric characteristics, must be selected based on the polymer solution that is used in the electrospinning. The co-axial outer layer of the filled solvent helps to induce enough surface charges and maintains the

electric field tangential to the fluid surface during the electrospinning process compared to the electrospun polymer solution for a wide range of conductivity values.

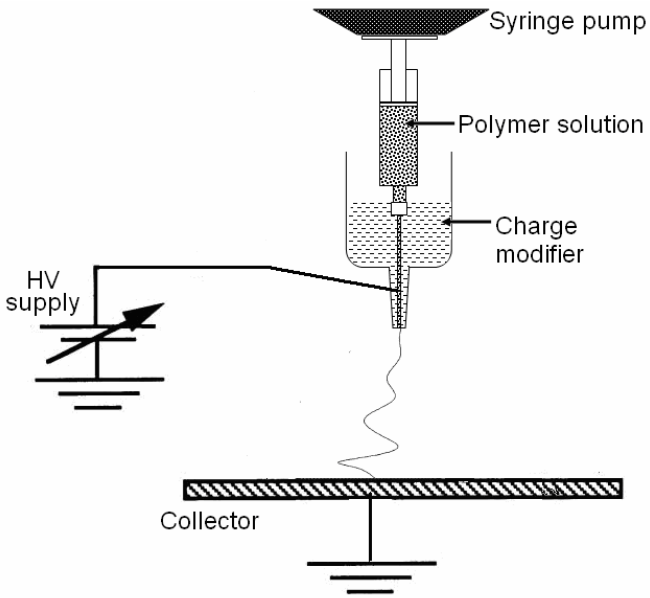


Fig. 6.19: A schematic of the modified experimental setup used in the electrospinning process.

### 6.4.1 Preparation of Materials

Two different solutions were prepared to investigate the modified electrospinning system. SA with a viscosity of 0.25 Pas purchased from Aldrich® was chosen to prepare the solution with high conductivity. In addition, RTV615 silicone rubber manufactured by GE Silicones® was used to electrospin as it is a liquid at room temperature with high insulating properties. SA was electrospun using 3% and 4% (w/w) concentrations of SA in de-ionized water. Additionally, water was used as a solvent in the charge modifier for electrospinning of SA. Alternatively, RTV615 was prepared for electrospinning by mixing RTV615 part A and B in 10:1 ratio where RTV615 part B is a curing agent. Furthermore, ethanol was used in the charge modifier with RTV615. All solutions were stored at room temperature and all electrospinning experiments were done at room temperature and atmospheric air.

In addition, Zein (a class of prolamine protein found in maize)/ethanol/water solutions were investigated using the charge modifier. Zein powder purchased from Aldrich® was chosen to prepare the solutions. Zein was dissolved in aqueous ethanol with a weight ratio of ethanol/water of 60:40. Thereafter, Zein fibres were electrospun using a 25% (w/w) concentration of Zein in prepared aqueous ethanol solution.

### 6.4.2 Experimental Results

#### 6.4.2.1 Behavior of Electrospun Jet

As illustrated in Fig. 6.20 (a), prior to the application of external electric field, the fluid droplet remains as it is, since there is no induced surface charges to form the Taylor cone and force a jet ejection. Fig. 6.20 (b) shows the behaviour of a droplet of RTV615 silicone rubber during the electrospinning using a conventional electrospinning setup. It was difficult to observe ejection of any thin jet since there were not enough charges at the fluid surface. Since, RTV615 is a liquid with very low conductivity ($8.46 \times 10^{-10}$ S/m); it does not have the ability to transfer the charges in the fluid to the surface. However, as shown in Fig. 6.20 (c), with the use of a charge modifier, RTV615 could be electrospun because of the surrounding ethanol at the fluid surface, form enough surface charges to pull out a thin jet from the Taylor cone.

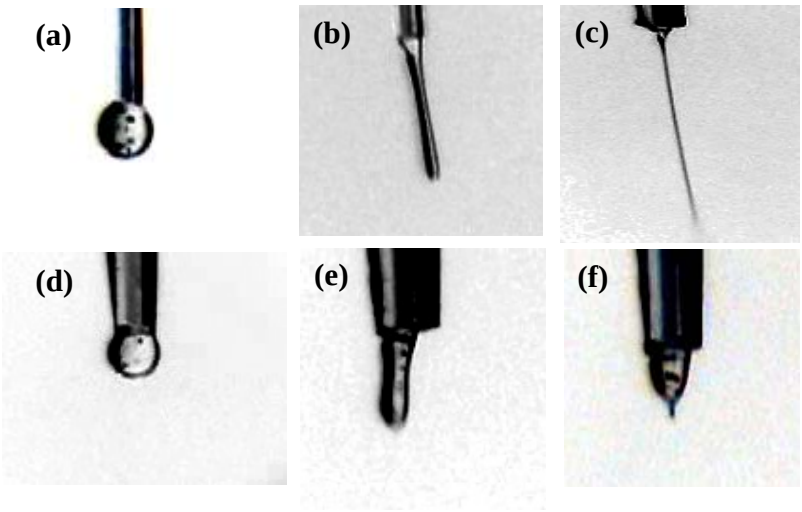


Fig. 6.20: Electrospun jet behavior of different polymer solutions: (a) RTV615 without external electric field; (b) RTV615, using the conventional system; (c) RTV615, using the charge modifier and ethanol as a surrounding solvent; (d) SA without external electric field; (e) SA, using the conventional system; (f) SA, using the charge modifier and water as a surrounding solvent.

In the case of high conductivity solutions, as illustrated in Fig. 6.20 (d), prior to the application of an external electric field, SA droplet also remains at the tip of the needle without forming a Taylor cone. Similar to the behaviour of RTV615, after the application of an external electric field with the conventional system, a jet of polymer solution was not ejected from the SA droplet. However, the ejection of a thin jet from its Taylor cone could be achieved by using the charge modifier to release

sufficient carriers to help form the Taylor cone. The differences in the jet shape with silicone rubber and SA could be related to the net charge on the surface of the cone, and the conductivity of the solution forming the cone.

#### 6.4.2.2 Characteristics of Fibre Morphology

Eventhough, the Taylor cone and jet formation were observed with the use of charge modifier, SA and RTV615 produce nano and micro sized droplets during the electrospinning process, as opposed to long fibres. Fig. 6.21 shows the formed droplets of SA during the electrospinning process. The detailed results of electrospinning of RTV615 have been published in [107]. The main cause that hinders the fibre formation of SA may be the lack of chain entanglements because of the rigid and extended SA chain conformations in the aqueous solution. Additionally, low molecular weight and reduced chain entanglements may restrict the fibre formation of RTV615. Fig. 6.22 illustrates the obtained electrospun fibres using a partly cured RTV615 blend.

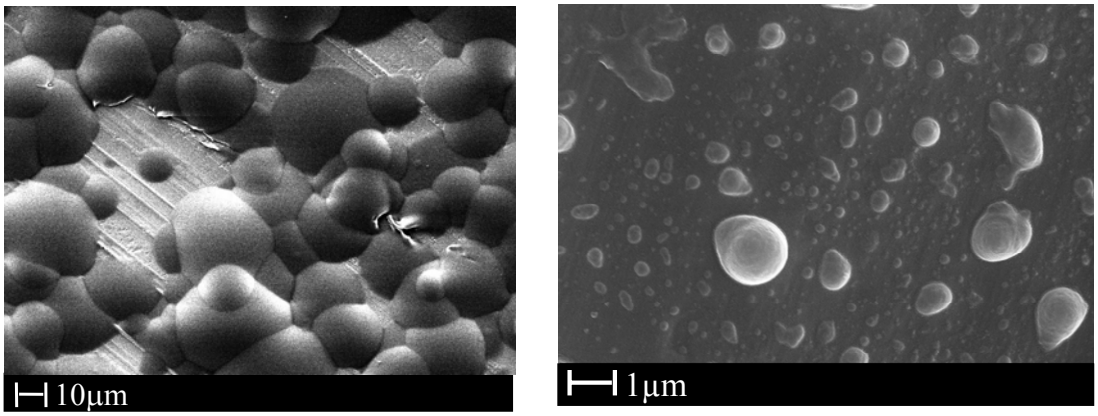


Fig. 6.21: SEM images of electrospun droplets: (a) RTV615 and (b) SA.

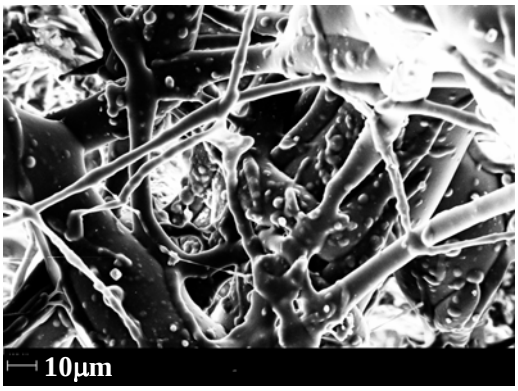


6.22: Electrospun RTV615 fibres.

On the other hand, zein/ethanol aqueous solutions are difficult to electrospin using the conventional electrospinning setup due to the rapid evaporation of the solvent at the surface of the droplet. As a result, the droplet quickly dries and no jet or fibre formation is possible. However, the use of the proposed charge modifier with aqueous ethanol as a filled solvent can overcome this difficulty; thus, helps for continuous electrospinning of zein/ethanol aqueous solutions. The electrospun zein nanofibres are shown in Fig. 6.23. Uniform fibres of 200 to 300 nm in diameter were successfully spun.

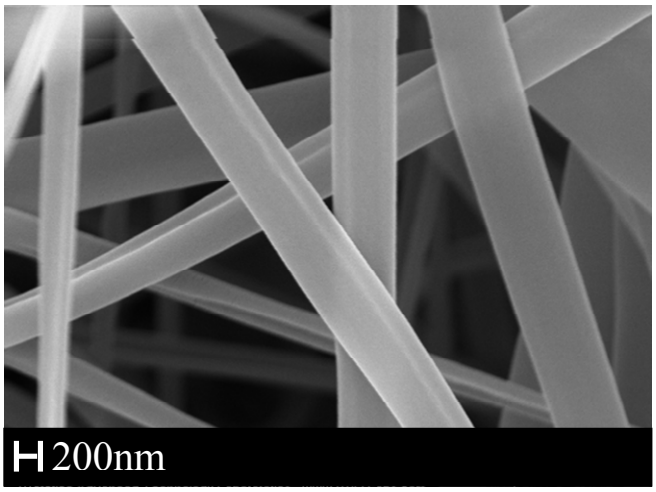


Fig. 6.23: SEM image of electrospun zein fibres.

# Chapter 7
# Discussion

## 7.1 Introduction

In this chapter the effects of electric field on the process of electrospinning and hence on the morphology of nanofibres presented in Chapter 5 are analyzed. In addition, field dependence on the applied voltage, polarity, distance between the needle and the collector plate, and multi-needle arrangements are discussed. Similarly, the characteristics of conductivity and ionic carriers in the polymer solution presented in Chapter 6 are investigated and their effects on the electrospinning process and fibre morphology are discussed by means of experimental and computational results.

## 7.2 Analysis of the Effects of Electric Field

As presented in Chapter 3, the basic principles for dealing with electrified fluids were developed in a series of papers written by Taylor in the early 1960s [12, 13]. It was shown that the electrospinning process is governed by a variety of forces which include Coulomb force between the charges on the jet surface, the electrostatistic force due to the external electric field, viscoelastic force due to the viscosity of the solution, surface tension force, gravitational force, and air drag force due to air friction. The entire electrospinning process including Taylor cone formation, the straight jet portion, and the whipping jet region is highly dependent on the Coulomb force between the charges on the surface of the fluid and the force due to the external electric field. However, the formation of the Taylor cone is mainly governed by the electrostatic force created by the surface charges with the application of an external electric field that can be divided into two components namely tangential field ($E_t$) which is tangential to the fluid surface and normal field ($E_n$) which is normal to the fluid surface as shown in Fig. 7.1. On the other hand, both the Coulomb force between the charges and the electrostatic force due to the external electric field influence the elongating and thinning of the straight jet portion. In a different way, the Coulomb force between charges is the main factor in the whipping instability of the jet [18].

In an uncharged ionic solution, there are same numbers of positive and negative carriers in each volume segment of the solution [18]. If the liquid has a sufficiently high electrical conductivity, the positive and negative ions in the polymer solution have a tendency to move in opposite directions with the application of an external electric field. Therefore, the excess charge, which is the difference in the number of positive and negative ions in a particular volume segment, is simply considered as its charge [18]. This would form a charged layer at the liquid-gas interface and the electrochemical equilibrium of the charge carriers is achieved by making the charge distribution such that the field is normal to the liquid surface [108].

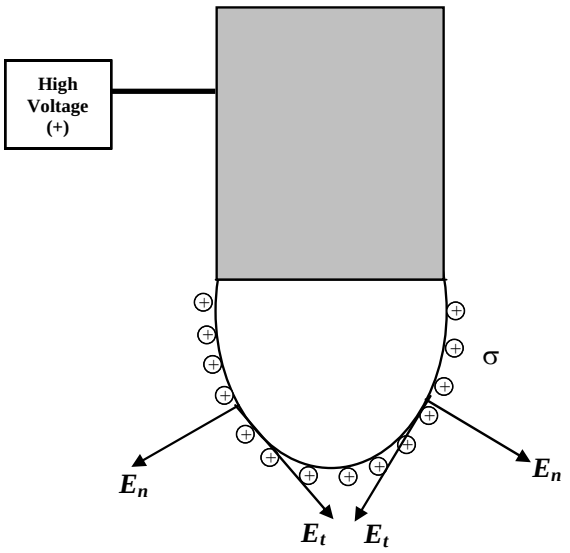


Fig. 7.1: Representation of tangential and normal electric fields at the fluid surface with the application of high voltage.

As shown in Fig. 7.1, if the surface charge density at the fluid surface is σ, simply the tangential electric stress ( $\tau_{es}$ ) can be calculated as follows.

$$\tau_{es} = \sigma E_t \tag{7.1}$$

It is this tangential electric field together with gravity disturbs the equilibrium state of a fluid droplet or jet. As a result, a liquid jet, which is pulled down under the action of above forces, accelerates and decreases the jet radius. However, the influence of gravity is negligible [18]. Therefore, the influential parameters for jet formation are the tangential electric field and the surface charge density at the fluid surface. Thus, the variation in the applied electric field, the conductivity, and ionic carriers in the solution affect significantly the value of $\tau_{es}$.

### 7.2.1 Single-Needle Arrangement

As reported in the above section, the interaction between the charges on the surface of the fluid droplet and the external electric field forms the Taylor cone with the application of high voltage. The surface charge density ($\sigma$) and the tangential electric field ($E_t$) at the fluid surface increase with the enhancement of electric field. Therefore, $\tau_{es}$ increases, altering the behaviour of the Taylor cone. A

very high $\tau_{es}$ causes the Taylor cone to reside in the needle. Similarly, the magnitude of $\tau_{es}$ directly relates to the length of the straight jet portion and the stretching of the jet in the straight jet region. On the other hand, the stretching in the whipping jet region not only influence by $\tau_{es}$ but also the force created by Coulomb repulsion. The diameter and uniformity of nanofibres are significantly influenced by the behaviour of all three regions in the electrospinning process. Therefore, the determination of fibre diameter with varying applied electric field is not straightforward due to the different behaviour of the electrospun jet in different regions. However, by comparing the fibre diameters with the applied electric field and the distance between the needle tip and the collector plate, it can be concluded that the fibre diameter decreases with increasing electric field if there is enough space for whipping region as the fibre diameter can be decreased with the increased stretching of the electrospun jet. The stretching of the electrospun jet increases with the increase of charges on the jet surface and flying time of the jet. The charges on the fluid surface increases with the increase of applied electric field. Equally, the length of the straight jet portion increases with the increase of applied electric field. On the other hand, whipping time decreases with the increase of applied electric field. Therefore, if the distance between the needle tip and the collector plate is not large enough, there is not enough time for the electrospun jet to decrease its diameter even at higher electric fields; hence, increases the fibre diameter with increasing electric field. Furthermore, it was observed that the fibre diameter cannot be varied significantly by changing the applied electric field. It was observed that the fibre diameter can be varied considerably by changing the material parameters such as conductivity and viscosity.

The shape of the beads depends on the degree of stretching during the electrospinning process. The stretching into nano-scale mainly occurs during the whipping region. The whipping region is increased significantly with increasing the distance between the needle tip and the collector plate. This results in the transformation of beads from spherical to spindle like shape due to the increased stretching. The viscosity and conductivity of the solution change considerably with the increase of polymer concentration producing beads free nanofibres during the electrospinning process.

### 7.2.2 Multi-Needle Arrangement

With the distortion in the local electric field at the needle tip due to the presence of the additional needle, the electrospun jet moves away from the vertical line, creating the angle $\theta$ (as shown in Fig. 4.13). As shown in Fig. 7.2, when the spacing between needles is increased, the local field distortion at each needle tips decreases which results in lower $\theta$. The experimental results show that $\theta$ increases with an increase in the number of needles in the needle arrangement. This correlation can easily be explained using the field simulation discussed in Chapter 4: Figures 4.7, 4.8, 4.9, and 4.10 illustrate the

local field distortion at the tip of each needle and show that the field distortion at each needle tip increases with the increase in the number of needles in the arrangement due to the increased influence of the other needles in the arrangement, which results in a larger $\theta$.

The initiation of the electrospun jet can be determined by the observed jet current data. The minimum required voltage is the initial point where a jet current was observed (greater than 0 μA). As shown in Figures 5.17 and 5.18, the jet current results reveal that the minimum required voltage to start the electrospinning increases considerably with the addition of more needles to the needle arrangement. This is due to the distortion in the local electric field at the tip of each needle. On the other hand, the jet currents of individual jets of multi jet schemes are considerably lower than the jet current of the single-jet scheme due to the field distortion at the tip of each needle in a multi-jet arrangement. These results mean that the total charge carried by multi-jets is less than the charge carried by a single jet in a single-jet scheme resulting in the variation of the fiber diameter and morphology.

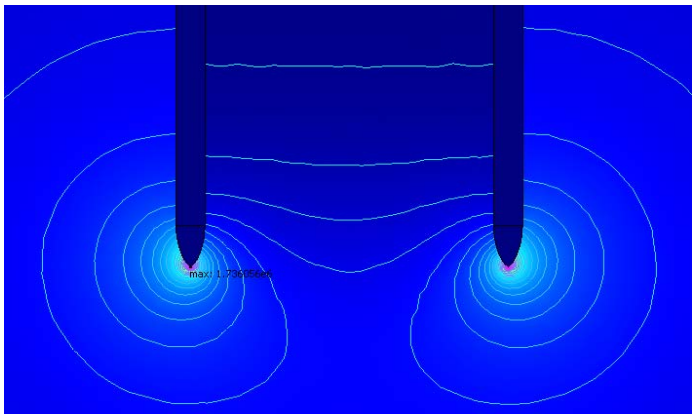

Fig. 7.2. Local electric field distribution at the needle tips of a 2-Needle arrangement.

The fibre diameter has been greatly affected by the local field distortion due to the multiple needles in multi-needle schemes as shown in Fig. 5.22. The diameter of nanofibres decreases with the increase of field distortion. In addition, obtaining uniform fibres in multi-jet schemes was difficult due to the deterioration of the local electric field. However, the average fibre diameter does not change greatly with an increase in needle spacing. There exists a controversy with respect to the electrospinning process as some researchers have observed that a higher electric field leads to greater stretching of the jet, resulting in thinner fibres [37, 49, 50]. It is verified in Section 7.2.1, a weaker electric field strength reduces the acceleration of the jet and hence increases the flight time of the electrospinning jet resulting in thinner fibres if it has enough distance between the needle tip and the collector plate. The observations agree with the latter conclusion, the thinner fibres might be due to the relatively large

distance (250 mm) between the needles and the target, providing enough travel time for the electrospun jet.

The jet path of a single-needle arrangement is mainly governed by the Coulomb charges that carried by the electrospinning jet. The lateral perturbation grew in response to the repulsive forces of Coulomb charges carried by the jet that at last create the electrically driven bending instability. For a single-jet, both lateral movements (in X and Y directions) are similar in magnitude. Therefore the jet path will be a circular one. However, as shown in Fig. 5.20 (c), the jet path is more elliptical in multi-jet schemes. The main reason for this behavior is the influence of the mutual Coulomb interactions between the paths of the individual electrified jets during the electrospinning process. This variation also influence on the diameter and the uniformity of nanofibers during multi-jet electrospinning.

### 7.2.3 Electrode Polarity

The distribution of the electric field between the needle tip and the collector plate for both positive and negative polarities was simulated using conductive media DC application mode in COMSOL Multiphysics. The results are shown in Fig. 7.3 and Fig. 7.4. Fig. 7.3 illustrates the potential distribution between the needle tip and the collector plate for both polarities whereas; Fig. 7.4 shows the variation of electric field between the needle tip and the collector plate along the line AB in Fig. 7.3 (a). The potential and field simulations reveal that there is no difference of the magnitude and the distribution of the electric field between the needle tip and the collector plate for both positive and negative polarities. Using the experimental setup that is shown in Fig. 4.15, the electric current through Milli-Q water, PEO, and glycerol solutions were measured. Number of ions presence in the solution is varied with the alteration of the applied voltage and it directly relates to the current through the solution. The obtained current versus applied voltage data is illustrated in Fig 7.5 (a) and (b). It reveals that the ionization in the solution is higher with the application of negative voltage to the needle electrode with compared to the application of positive voltage to the needle. This increases the surface charge density of a negatively charged fluid droplet. Therefore, it can be observed that a higher jet current and a greater stretching of the electrospun jet with the application of a negative voltage to the needle electrode. As a result, negative voltages produce thinner fibres with compared to positive voltages. When the magnitude of the applied voltage is increased, the concentration of ions in the solution also increases at a much higher rate resulting an unstable straight jet. This is noticeable with the application of negative voltage of higher magnitude to the needle electrode. This can be confirmed that investigating an electrospun jet of glycerol droplet as shown in Fig. 7.6. Fig. 7.5 (b) shows the variation in the current through a glycerol sample and it shows an identical behaviour to both positive and negative voltages.

Similarly, as illustrated in Fig. 7.6, the electrospun jet of glycerol does not depend on the polarity of applied voltage.

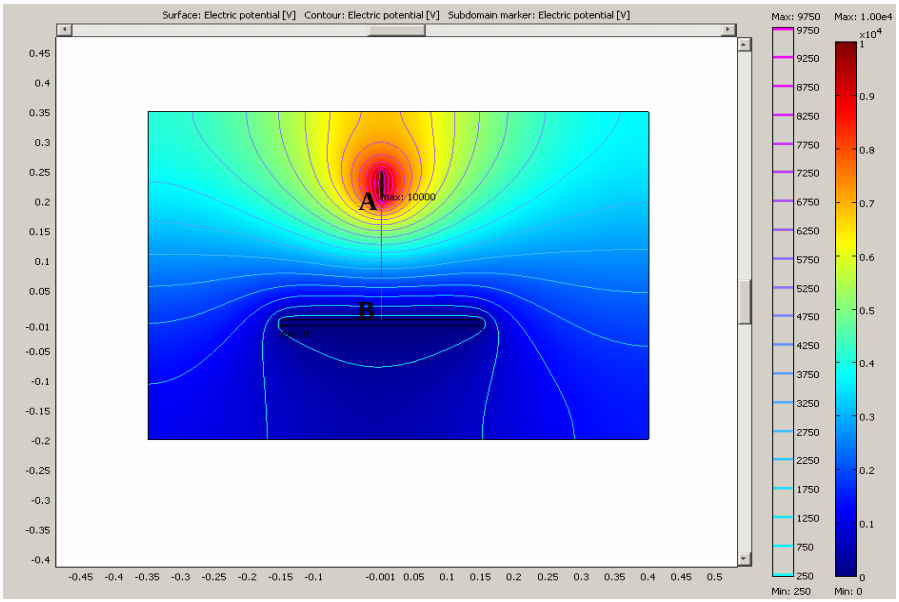


(a)

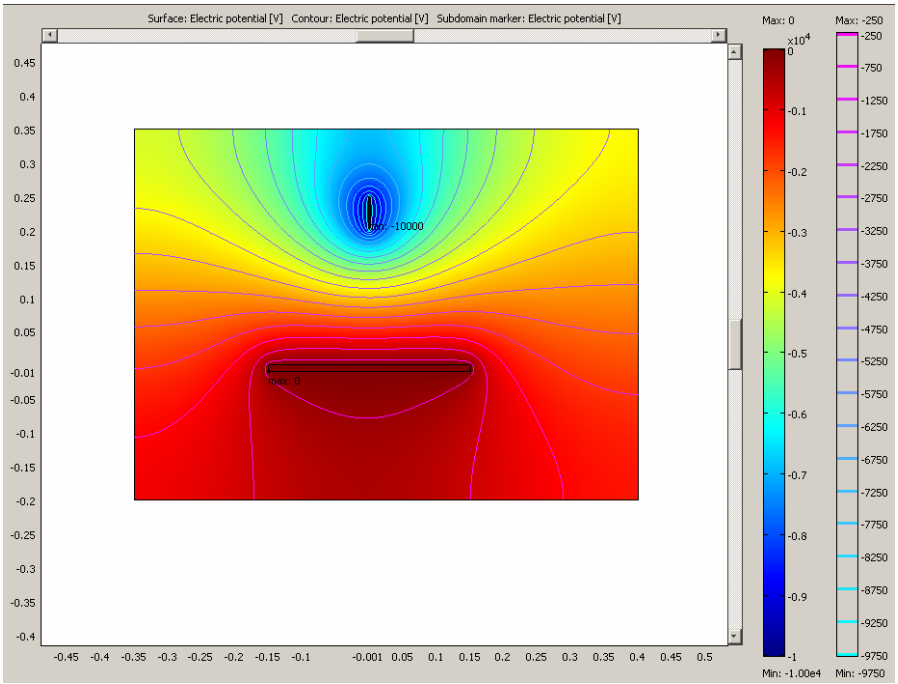


(b)

Fig. 7.3: Potential distribution between the needle tip and the collector plate with the application of high voltage to the needle: (a) positive and (b) negative.

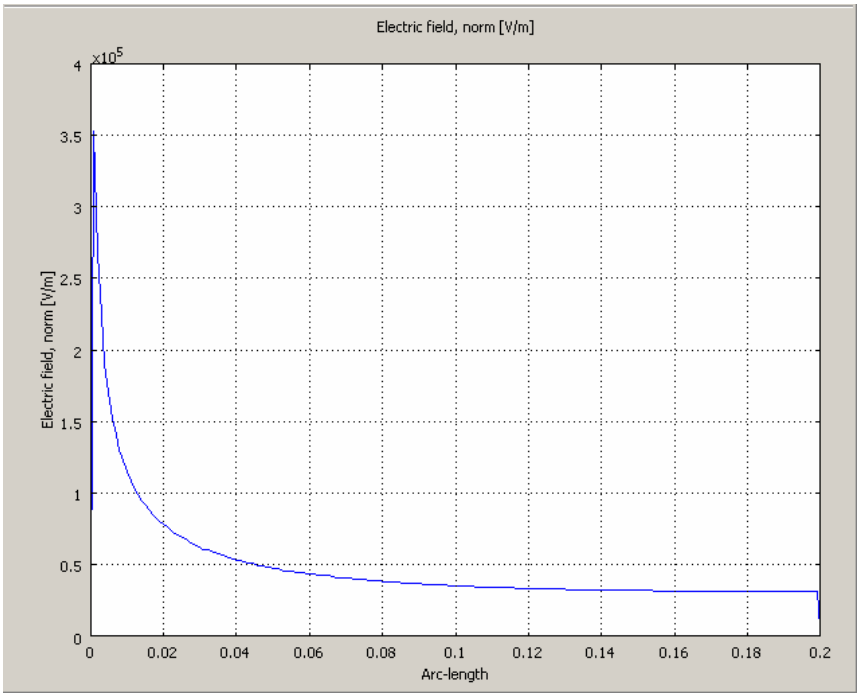


(a)

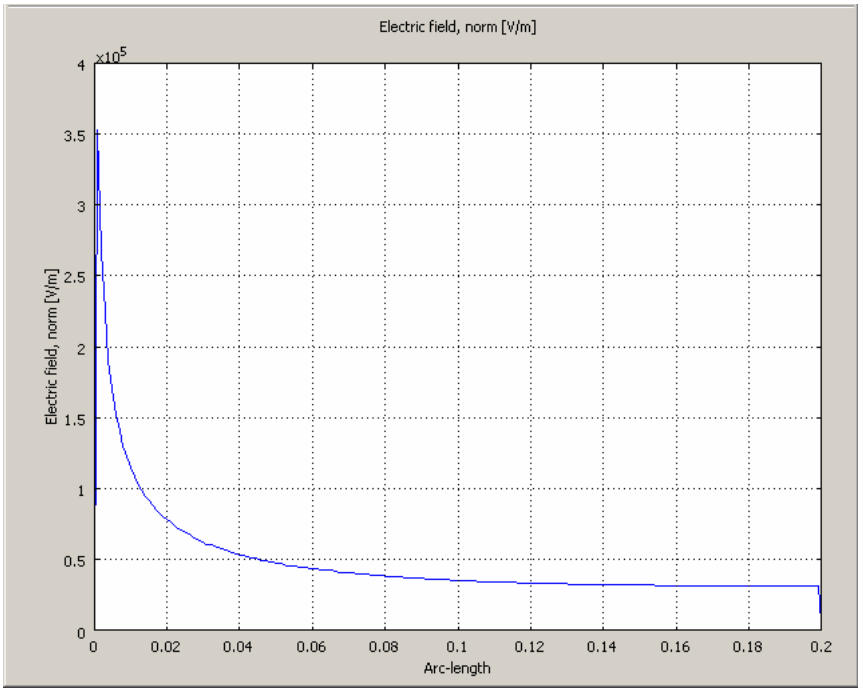


(b)

Fig. 7.4: Distribution of the electric field along the line AB in Fig. 7.3 (a) with the application of high voltage to the needle: (a) positive and (b) negative.

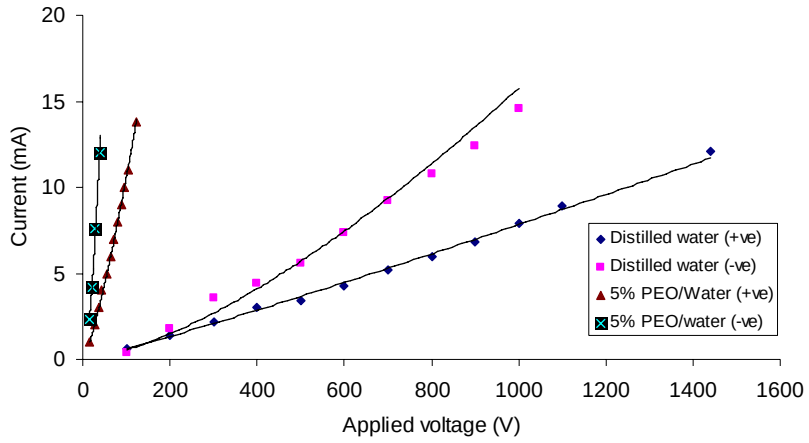


(a)

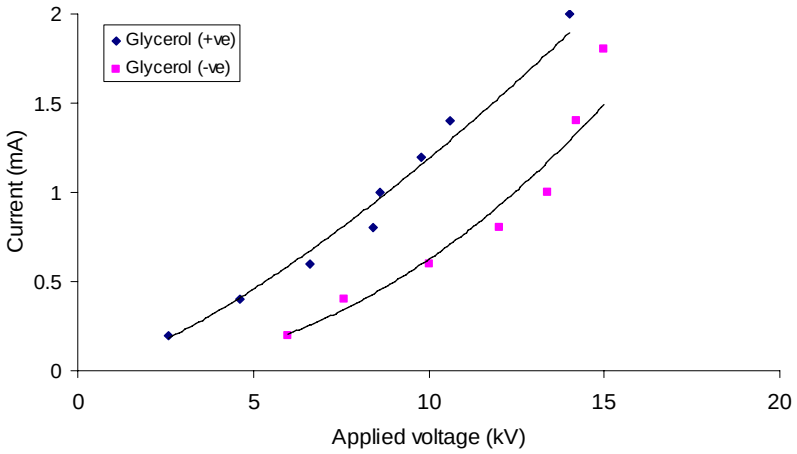


(b)

Fig. 7.5: Variation in the current through different solutions with the application of voltage: (a) aqueous PEO and Milli-Q water and (b) glycerol.

(a) (b)

Fig. 7.6: Behaviour of the electrospun jet from a glycerol droplet with the application of high voltage to the needle electrode: (a) positive and (b) negative.

### 7.2.4 Optimum Range

By considering the above analysis, authors introduced a working range of the applied electric field for a stable operation of the electrospinning jet and to obtain the uniform fibres over a range of distances between the needle tip and the collector plate. As shown in Fig. 7.7, there are unstable and partially stable regions above and below the threshold values of applied electric field. These are mainly due to the instability of the Taylor cone and straight jet portion. The partially stable region can be instituted, where, even though the stable electrospinning takes place; there is no visible Taylor cone at the tip of the needle. As shown in Fig. 7.7 and 7.8, the lower threshold value of the electric field (~0.9kV/mm)

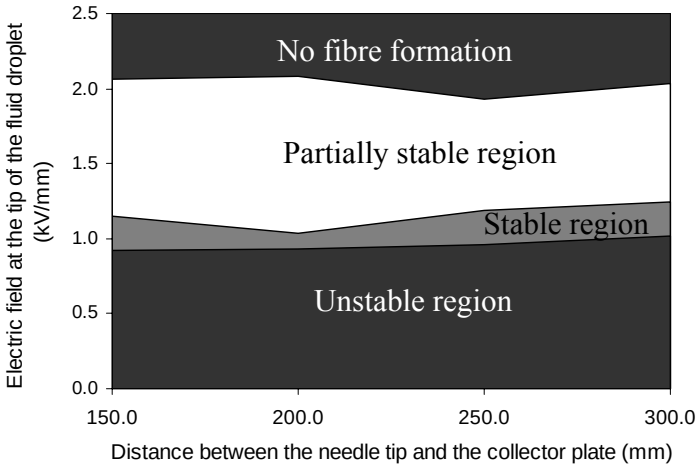


Fig. 7.7: Operation regime of the applied electric field over a range of distances between the needle tip and the collector plate.

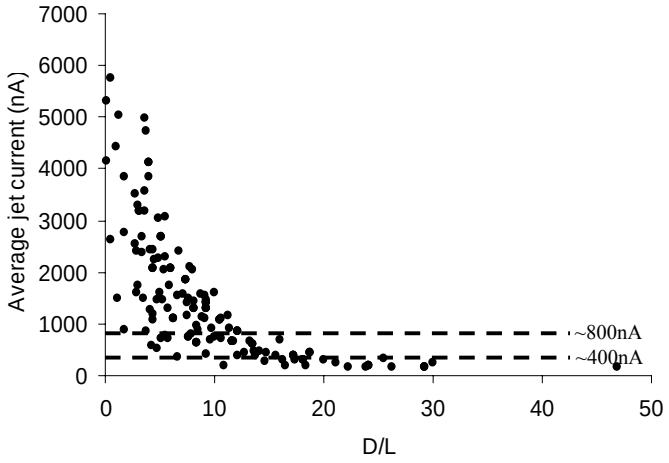


Fig. 7.8: The variation of average jet current versus D/L.

corresponds to the jet current of about 400nA and the upper threshold value (~1.1kV/mm) corresponds to the jet current of about 800nA. However, the stable operating region will be altered slightly with the variation of other fluid parameters such as conductivity and viscosity.

## 7.3 Conductivity and Tangential Electric Field

Repulsion of the charges at the surface of the electrospinning jet causes the solution to stretch and form the nanofibres, the stretching of the electrospun jet and the bending instability are mainly controlled by the Coulomb force between charges and the force due to the external electric field. Both these forces emerge due to the surface charge on the jet; hence, it can be varied by changing the conductivity and charge concentration in the solution.

Equations (7.2), (7.3), (7.4), and (7.5) represent four simplified steady-state equations that govern the electrospinning jet including the conservation of mass and electric charges, the linear momentum balance, and Coulomb's law for the electric field [93, 94]. The meanings of the symbols are presented in Appendix E.

$$\pi R^2 v = Q \tag{7.2}$$

$$\pi R^2 KE + 2\pi R v \sigma^{\alpha} = I \tag{7.3}$$

$$\rho v v' = \rho g + \frac{3}{R^2}\frac{d}{dz}\left(\eta R^2 v'\right) + \frac{\gamma R'}{R^2} + \frac{\sigma\sigma'}{\bar{\varepsilon}} + \left(\varepsilon - \bar{\varepsilon}\right)EE' + \frac{2\sigma E}{R} \tag{7.4}$$

$$E(z) = E_{\infty}(z) - \ln\chi\left(\frac{1}{\bar{\varepsilon}}\frac{d(\sigma R)}{dz} - \frac{\beta}{2}\frac{d^2\left(ER^2\right)}{dz^2}\right) \tag{7.5}$$

In the electrospinning process, the current ($I$) was considered to consist of the Ohmic bulk conduction current and the surface convection current as described in Equation (7.3). Where $\alpha$ is a surface charge parameter, and in most of the literature it has been valued at 1, as shown in Fig. 7.9 (a). However α can be varied between 0 and 1 according to the charge distribution around the surface of the nanofibre as in Fig. 7.9 (b) [109]. When $\alpha$=0, the total current is caused by the bulk conduction. The value of $\alpha$ depends on the conductivity and dielectric constant of the polymer solution [109]. Therefore the value of $\alpha$ can be changed by varying the salt concentration in the solution.

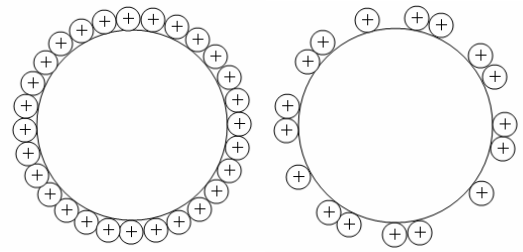

Fig. 7.9: Charge distribution around the fibre surface with application of positive DC voltage. (a) $\alpha$=1, (b) 0< $\alpha$<1.

Equation (7.5) represents the total axial electric field of a typical electrospinning setup due to the external field (as a result of the applied voltage) and induced field (as a result of the charged jet) [94]. As stated in Equation (7.4), in electrospinning, the ejected fibre jet is elongated mainly by the electrostatic forces which include Coulomb force and the electrostatic force due to the external electric field since the force due to gravity is negligible. In contrast, the forces of surface tension and viscosity resist the pulling force. In 1997 Saville introduced the "leaky dielectric model," where the liquid was considered as a weakly conducting fluid that has the characteristics of quickly conducting the charges to the surface from its interior and the ability to sustain the electric field tangential to the jet surface [94, 104]. It was reported that when the jet flows away from the needle tip, the jet gets thin and the surface charge density varies by affecting the pulling force [94].

As discussed in Section 7.2, the formation of the Taylor cone is governed mainly by the electrostatic force created by the surface charges created by the application of an external electric field. Most importantly, the component of the field that is tangential to the surface of the fluid induces this electrostatic force. If the polymer solution is a perfect dielectric ($K < 10^{-8}$), there are not enough charges in the solution to move onto the surface of the fluid, so the electrostatic force generated by the application of an external electric field is insufficient to form a Taylor cone. The electrospinning process will therefore not initiate, and nanofibers will not be formed. In contrast, leaky dielectrics that have enough free charges to move onto the surface of the fluid form a Taylor cone at the tip of the fluid droplet, and the electrospinning process will then start making nanofibers. Fig. 7.9 (b) shows the distribution of the corresponding surface charge on a jet surface that has a value of the parameter $\alpha$ between 0 and 1.

The addition of NaCl affects the electrospinning process in two ways. First, the addition of NaCl increases the number of ions in the polymer solution, which causes the surface charge density at the surface of the fluid to increase. The electrostatic force induced on the fluid surface therefore increases significantly due to the external electric field [74-77]. The increased electrostatic force facilitates the

formation of a Taylor cone. On the other hand, NaCl increases the conductivity of the solution, which causes a decrease in the tangential electric field along the surface of the fluid. Fig. 7.10 shows the distribution of the normal and tangential electric fields along the surface of the fluid for samples $S_0$, $S_5$, and $S_9$ that were discussed in Chapter 6. As shown in Fig. 7.10 (a), the normal stress does not change at

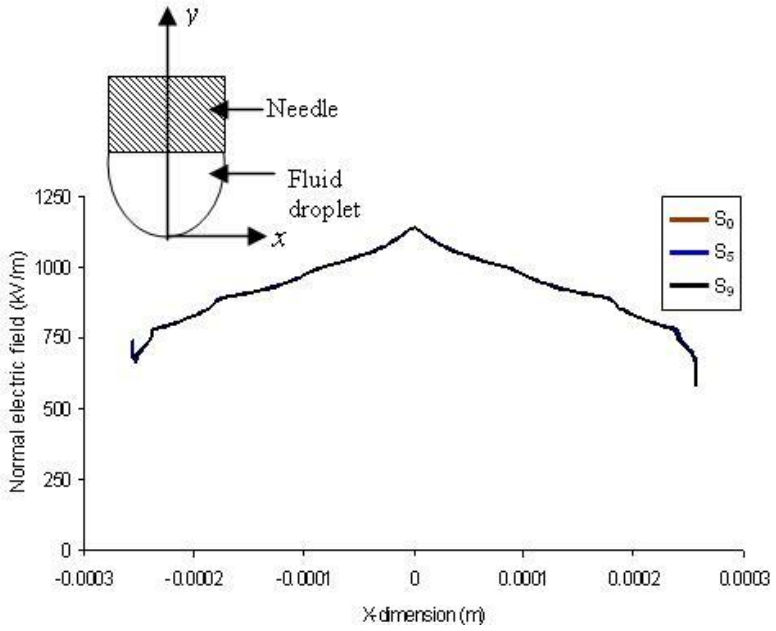


(a)

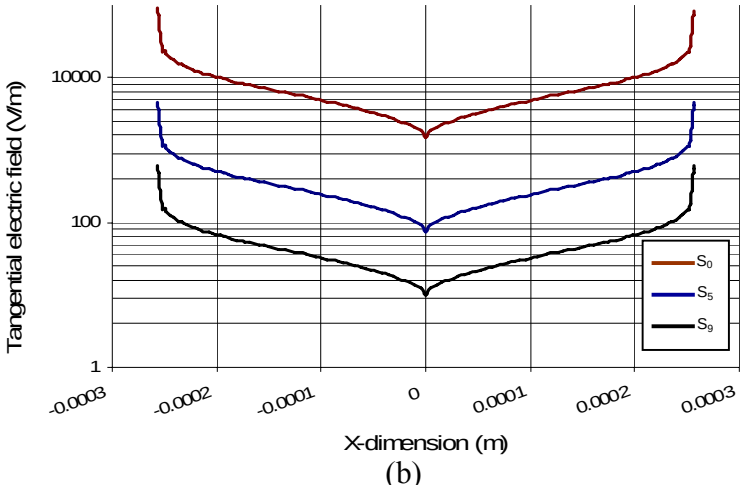


(b)

Fig. 7.10: Simulated electric field distribution along the surface of the fluid droplet: (a) normal field distribution and (b) tangential field distribution.

all with increase in the conductivity. However, the tangential electric field decreases extensively with an increase in the conductivity of the solution, as illustrated in Fig. 7.10 (b). This behaviour causes the electrostatic force along the surface of the fluid to diminish considerably. The total effect of these two parameters that are the surface charge density and the tangential electric field determine the behaviour of both the Taylor cone formation and the straight jet portion of the conductive fluids. As shown in Fig. 6.11 (b), at very high conductivities, the dominant factor is the reduction in the tangential electric field, which has a negative effect on the formation of the Taylor cone [77].

The length of the straight jet portion and the behavior of the whipping jet region have a significant influence on the diameter of the nanofibres. Most importantly, the stretching in the whipping region due to the surface charges draws the fluid jet into the nano scale. The number of ions in the polymer solution increases gradually with the addition of greater amounts of NaCl, which means that the surface charge distribution increasingly approaches $\alpha$=1, as shown in Fig. 7.9 (a). As a result, with the increase in the conductivity of the solution, the diameter of the fiber decreases extensively at first. After $\alpha$=1 is reached, the dominant effect is a decrease in the tangential electric field at the surface of the fluid. The reduction in the tangential electric field decreases the length of the straight jet portion, which results in an increase in the flying time of the electrospun jet. A linear decrease of the fiber diameter can therefore accompany a further increase in the conductivity of the solution. In addition, when $\alpha$ reaches a value of 1, the drawing of the fiber becomes more uniform, thus resulting in highly uniform fibers at a higher conductivity. The formation of multi-jets from the fluid droplet can also be observed when the NaCl concentration in the solution is increased, mainly because of the enhancement of the local field at the surface of the fluid caused by the presence of additional ions. A similar observation can be made when the electric field around the fluid droplet is altered through the use of external electrodes with sharp edges.

## 7.4 Ionic Carriers and Surface Charge Density

As presented in the above sections, leaky dielectric solutions have the characteristics of quickly conducting the charges to the surface from the interior and the ability to sustain the electric field tangential to the jet surface. Therefore, perfect dielectric solutions which have no ability to conduct the charges from inside to the fluid surface or highly conductive polymer solutions which do not have the ability to sustain the electric field tangential to the fluid surface are very difficult to electrospin. Fig. 7.10 (b) shows the tangential electric field at the fluid surface of a solution with the increase in solution conductivity from 8 µS/mm ($S_0$) to 1160 µS/mm ($S_9$). It can be observed that the tangential electric field decreases appreciably when the conductivity of the solution increases by several orders. This finally results in the reduction of tangential electric stress, influencing the jet formation from the Taylor

cone. As shown in Fig 6.20 (e), this is the main difficulty of electrospinning sodium alginate as it significantly decreases the tangential electric field at the fluid surface as a result of its high conductivity ($5.41 \times 10^{-1}$ S/m). On the other hand, as shown in Fig. 7.11 (b), if it is a highly insulating liquid, there are not enough free carriers at the fluid surface since it is very difficult to separate the charges. This would result in the reduction of surface charge density at the fluid surface; hence, $\tau_{es}$ as in RTV615. Therefore, for a jet ejection from the Taylor cone, the solution must be a leaky dielectric solution which has the ability to quickly conduct the charges to the surface from its interior and sustain the electric field tangential to the fluid surface.

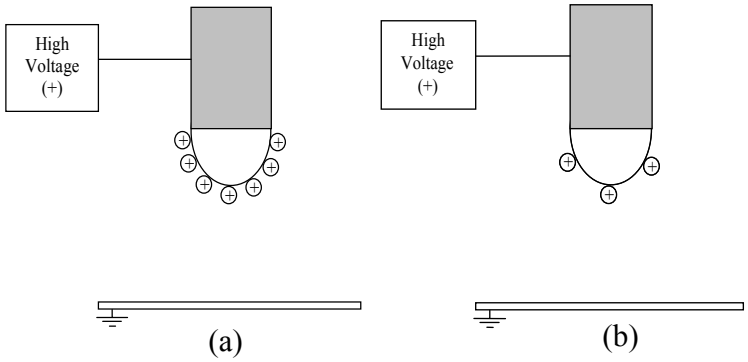


Fig. 7.11: Representation of the presence of surface charge at the fluid surface: (a) semi-insulating liquid and (b) insulating liquid.

As discussed in Chapter 3, the presence of surface charge on the fluid surface is also essential for the initiation of the instability and stretching of the polymer jet during the electrospinning. It ultimately determines the morphology of nanofibres. The charge density at the fluid surface is greatly influenced by the amount and size of ionic carriers that present in the polymer solution. As explained in Section 7.3, the stretching of the electrospun nanofibres increases with the increase of charge concentration in the polymer solution. The increase of concentration of ionic carriers in the solution increases the amount of available surface charge at the fluid surface during electrospinning. This results in increasing the electrical forces on the fluid surface making greater stretching of the fluid jet.

It is presented in Chapter 6 that the stretching of the electrospun jet also decreases with increasing the size of positive ions in the solution. Equation 7.6 shows the conductivity of a solution having positive and negative ions.

$$K = e\mu_n n + e\mu_p p \tag{7.6}$$

where $K$ is the conductivity of the medium, $e$ is the charge per ion, $\mu_n$ is the mobility of the negative ions, $\mu_p$ is the mobility of the positive ions, and $n$ and $p$ are concentrations of the negative and positive

ions respectively. As presented in Table 6.3 and 6.4, the variation in the conductivity of polymer solutions is insignificant with the addition of different types of salt at the same concentration. Therefore, with reference to Equation 7.6, the variation in the mobility of different ions is also minor. Accordingly, as presented in Table 7.1, the main cause for the variation in fibre morphology might be due to the different sizes of positive and negative ions. As shown in Fig. 7.12, the number of ions that can accommodate on the fluid surface decreases with the increase of the size of the ion. It ultimately decreases the electrical forces that stretch of the electrospun fluid jet. The increase of negative ions in the solution decreases the density of surface charge due to recombination that adversely affects the stretching of the electrospun jet. This effect of negative ions enhances with the use of smaller sized ions.

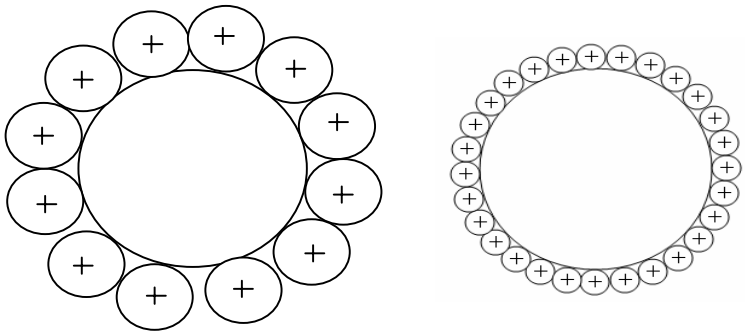


Fig. 7.12: Representation of the presence of positive surface charge at the fluid surface: (a) larger ions such as $Cs^+$ and (b) smaller ions such as ($Li^+$).

Table 7.1: Ionic radii of different positive and negative ions [110].

| Positive ions | | Negative ions | |
|---|---|---|---|
| Type of ion | Ionic radii (pm) | Type of ion | Ionic radii (pm) |
| $Li^+$ | 60 | $F^-$ | 136 |
| $Na^+$ | 95 | $Cl^-$ | 181 |
| $K^+$ | 133 | $HCO_3^-$ | 450 |
| $Cs^+$ | 174 | $CO_3^{-2}$ | 450 |

# Chapter 8
# Conclusions and Suggestions for Future Work

## 8.1 Conclusions

The electrospinning process is influenced by variety of parameters such as viscosity of the solution, conductivity of the solution, polymer concentration in the solution, surface tension, applied voltage, distance between the needle tip and the collector plate, and flow rate. The variation of these parameters alters the electrospun jet and hence the morphology of nanofibres. Based on the review of parametric studies, we can realize that some of these parameters have been investigated to study their effects on the morphology of nanofibres. However, there was less concern over the effects of these parameters on the electrospinning process. In addition, some important parameters such as solution conductivity that can highly influence the electrospinning process and fibre morphology were yet to be investigated. This research has therefore focused on gaining a comprehensive understanding of the effects of most of these parameters on the electrospinning process and hence on morphology of nanofibres. The conclusions of the work are summarized in the following sections.

A basic electrospinning setup has been designed to perform the electrospinning experiments without much difficulty in the vertical and horizontal directions. The necessary modifications were made to obtain the desired results and measure the needed parameters such as jet current. Aqueous PEO solution was used to conduct the electrospinning experiments.

A comprehensive study was carried out by giving a special attention to the effects of electric field that have not been thoroughly investigated in the past. The electric field between the needle and the collector plate was altered by varying the applied voltage, distance between the needle tip and the collector plate, and the inner diameter of the needle. The shape of the Taylor cone varies with the changes of the electric field at the tip of the fluid droplet. Therefore, by considering the stability of the Taylor cone, it can be concluded that the stable operating region of the electrospun jet is a very narrow region and it is between 0.9 –1.1kV/mm for the range of experiments carried out in this studies. The stable operating region can alter slightly with the variation of other fluid parameters such as conductivity and viscosity.

The length of the straight jet portion of the electrospun jet shows a linear relationship to the electric field at the tip of the fluid droplet. On the other hand, the whipping jet region is influenced by both the electric field at the tip of the fluid droplet and the distance between the needle and the collector plate. Therefore, if there is not enough distance between the needle and the collector plate, the drying of the nanofibres can be affected. There must be enough distance between the needle and the collector plate (>200mm) to operate over the complete range of voltages. It can be concluded that the morphology and

diameter of the collected nanofibres depend significantly on both the length of the straight jet portion and size of the whipping region.

The effects of polarity of the applied voltage on the electrospinning process and nanofibre morphology were investigated using the positive, negative, and AC voltages. The effects of polarity depend on the ionization characteristics of the polymer solution with the application of high voltage. It was observed that the ionization is different with the application of different polarities. In the case of aqueous polymer solutions, negative polarity shows a higher jet current, greater stretching of the electrospun jet due to the higher ionization of the polymer solution. Furthermore, it was observed that the electrospinning can not be achieved with the application of 60Hz AC voltage.

The variation in the strength of the electric field at the tip of the needles in multi-needle arrangements was investigated using FEM simulation. The results were compared with a single-needle system, and it was observed that the local electric field strength weakened significantly in the case of multi-needle schemes due to the mutual influence of the electric fields around each needle tip. The spacing between the needles was varied, and the effects of the needle spacing on the electric field were simulated. The experimental results that were obtained using an aqueous PEO solution in the fiber formation matched with an average maximum electric field calculated at each needle tip. The behavior of the vertical angle of the straight jet portion, the average jet current, the average diameter of the fiber, and the collected area of the electrospun fibers in multi-needle schemes were investigated, and the results were compared with those obtained with a single-needle scheme. The degree of field distortion correlates with the variation in the measured vertical angle of the straight jet portion for different needle spacing. However, the influence of needle spacing on the average jet current and the diameter of the fibers are not highly significant. It can be concluded that the local field deterioration at the needle tips in multi-needle schemes degrades the electrospinning process significantly and produces considerable variation in the morphology of the fiber.

An aqueous PEO solution with the addition of NaCl was used to investigate the effects of conductivity in the polymer solution on the behaviour of electrospun jet and nanofibre morphology. The results show that the average jet current at first increases with increase in the conductivity of the solution and, thereafter decreases slightly. On the other hand, the average fiber diameter decreases with increase in the conductivity of the solution, and it shows a power law relationship. These behaviors can be fully accounted for the distribution of the surface charge around the electrospun jet and the variation in the tangential electric field along the surface of the fluid droplet. Polymer solutions that have very low conductivity can not electrospin because there is not enough charges on the surface of the fluid droplet to form a Taylor cone. Similarly, solutions with very high conductivity do not also form a Taylor cone because of the depleted tangential electric field along the surface of the fluid droplet. The

other effects that can be observed when the conductivity of the polymer solution is increased are the formation of multi-jets at the fluid droplet during the electrospinning and protrusions in the morphology of nanofibers.

The charge modifier was introduced to facilitate the electrospinning of insulating and high conductivity polymer solutions. The charge modifier is a special container that is used to hold the solvent surrounds the needle tip during the electrospinning. The filled solvent helps to induce enough surface charges during the electrospinning, in case of insulating liquid. On the other hand, it keeps the electric field tangential to the fluid surface for solutions with high conductivity, above threshold. The developed method was verified by using sodium alginate which is a biopolymer that cannot electrospin alone due to its high electrical conductivity and silicone rubber which is an insulating liquid polymer at room temperature.

The effects of ionic carriers on the electrospinning process and fibre morphology were studied using PEO and PAA polymer soltions. Different salts including LiCl, NaCl, NaF, $NaHCO_3$, KCl, and CsCl were added in different concentrations to the polymer solutions for introducing different ionic carriers into the solution. It was observed that the increase of amount of ionic carries increases the stretching of the polymer jet. In addition, the smaller diameter positive ions enhance the stretching of the electrospun jet. In contrast, it was observed that the lesser diameter negative ions decrease the stretching of the electrospun jet. The morphology of electrospun nanofibres can also be varied by altering the type of salt.

The already existing discrete theoretical model of electrospinning was improved to account the non-uniform characteristics of the electric field at the tip of the needle. The method used for calculating the distribution of the electric field between the needle tip and the collector plate is based on the charge simulation technique. It can make a better representation of the actual electrospinning environment. The modified model will be used to understand the effects of parameters on the electrospinning process, fibre morphology.

## 8.2 Suggestions for Future Work

The accurate measurement of the semi vertical angle of the envelope cone is essential for precise analysis of the whipping region of the electrospun jet. In our investigations, the diameter of the collected area was used to evaluate the semi-vertical angle of the envelope cone. However, a high speed camera such as photron® can be used to capture the electrospun jet precisely with additional details. It will greatly help further analysis of the parameter investigations.

Although many researchers have used single-needle schemes for electrospinning, the low fluid throughput in spinning has limited the industrial use of single-needle schemes. To meet high liquid

throughput requirements, several multi-needle schemes have been tested recently. However, one of the major drawback of these multi-needle schemes is the deterioration of the electric field at the tip of each needle. This decreases the rate of production of nanofibres, increases the required voltage for jet initiation, and creates non-uniform fibre diameters. Therefore, a novel electrode system could be investigated for multi-needle schemes to mitigate above mentioned drawbacks. FEM simulation tools can also be used for the optimization purposes.

The major challenge associated with the electrospinning is its lower production rate compared to the conventional fibre spinning. To meet high liquid throughput requirements, several multi-needle schemes have been tested recently. These schemes are technologically inconvenient due to possible clogging. In addition, it is generally accepted that eletrospinning using needles, which is defined as capillary spinning, leads to low productivity of nanofibres. Alternatively, in principle, it is possible to obtain self-organized, multiple electrically driven jettings from planar and cylindrical surfaces by applying very high electric fields. Recently, experimental and theoretical efforts have been demonstrated to enhance the fibre production rate to an industrial scale by free surface electrospinning using both Newtonian and viscoelastic polymeric liquids. However, a thorough investigation is necessary to optimize the process and control the nanofibre morphology. The new technique can be tested for a wide range of operating conditions and polymer solutions using a prototype.

Several mathematical models have been developed to determine qualitatively the electrospinnng process. Since the model explains the jet behaviuor qualitatively, improvements are needed for a quantitative analysis. The discrete model of the electrospun jet, reported in chapter 3, is used to analyze and study the electrospinning process as it explains the behaviuor of the electrospun jet completely. However, the discrete model can not be used to analyze accurately the straight jet portion. On the other hand, the analytical model, which was developed by Feng [94], can accurately determine the straight jet portion of the electrospun jet. Therefore, a combined model will further improve the predicting capabilities of the real electrospun jet.

In Chapter 6, it was observed that the addition of different types of salt into the polymer solutions leads to different nanofibre morphologies. This can be another interesting research topic as there are many different applications that require different morphologies of nanofibres.

The charge modifier method was introduced in Chapter 6 to facilitate the electrospinning of insulating and high conductivity polymer solutions. However, it was tested only with aqueous sodium alginate, silicone rubber, and zein/ethanol/water solution. The charge modifier method could be tested using other conductive and insulating polymer solutions and this method can be developed as a viable technique to electrospin insulating and high conductivity polymer solutions without blending.

# References


[1] S. Ramakrishna, K. Fujihara, W.E. Teo, T.C. Lim, and Z. Ma, *An Introduction to electrospinning and nanofibers*. Singapore: World Scientific Publishing Co. Pte. Ltd., 2005.

[2] Z. M. Huang, Y.Z. Zhang, M. Kotaki, and S. Ramakrishna, "A review on polymer nanofibers by electrospinning and their applications in nanocomposites," *Composites Science and Technology*, vol. 63, pp. 2223-2253, April 2003.

[3] A. S. Nain, J. C. Wong, C. Amon, and M. Sitti, "Drawing Suspended Polymer Micro/Nanofibers Using Glass Micropipettes," *Applied Physics Letters*, vol. 89, no.18, pp. 183105-7, 2006.

[4] A. S. Nain, C. Amon, and M. Sitti, "Proximal Probes based Nanorobotic Drawing of Polymer Micro/Nanofibers," *IEEE trans. on Nanotechnology*, vol. 5, issue. 5, pp. 499-510, Sep. 2006.

[5] A. Huczko, "Template-based synthesis of nanomaterials," *Applied Physics A: Materials Science & Processing*, vol. 70, No. 4, pp. 365-376, Mar. 2000.

[6] D. Zhang, and Y. Wang, "Synthesis and applications of one-dimensional nano-structured polyaniline: An overview," *Materials Science and Engineering B*, vol. 134, issue. 1, pp. 9-19, Sep. 2006.

[7] S. Zhang, "Fabrication of novel biomaterials through molecular self-assembly," *Nature Biotechnology*, vol. 21, no. 10, pp. 1171-1178, oct. 2003.

[8] Z. Wei, Z. Zhang, and M. Wan, "Formation Mechanism of Self-Assembled Polyaniline Micro/Nanotubes," *Langmuir*, vol. 18, no. 3, pp. 917-921, Jan. 2002.

[9] N. R. Chiou, L. J. Lee, and A. J. Epstein, "Self-Assembled Polyaniline Nanofibers/Nanotubes," *Chem. Mater.*, vol. 19, pp. 3589-3591, June 2007.

[10] J. Zeleny, "Physical review," *Phy. Rev.,* vol. III, No. 2, pp. 69-91, Feb. 1914.

[11] A. Formhals, "Process and apparatus for preparing artificial threads," U.S. Patent No. 1975504.

[12] G. Taylor, "Disintegration of Water Drops in an Electric Field," *Proceedings of the Royal Society of London, Series A, Mathematical and Physical Sciences*, vol. 280, No. 1382, pp. 383-397, Jul. 1964.

[13] G. Taylor, "Electrically Driven Jets," *Proceedings of the Royal Society of London, Series A, Mathematical and Physical Sciences*, vol. 313, No. 1515, pp. 453-475, Dec. 1969.

[14] D.A. Saville, "Electrohydrodynamic Stability: Fluid Cylinders in Longitudinal Electric Fields," *Phy. of Fluids,* vol. 13, No. 12, pp. 2987-2994, Dec. 1970.

[15] D.A. Saville, "Stability of Electrically Charged Viscous Cylinders," *Phy. of Fluids,* vol. 14, No. 6, pp. 1095-1099, Jun. 1971.

[16] M.M. Denn, C.J.S. Petrie, and P. Avenas, "Mechanics of Steady Spinning of a Viscoelastic Liquid," *AlChE Journal*, vol. 21, No. 4, pp. 791-798, Jul. 1975.

[17] O. Jirsák and T.A. Dao, "Production, Properties and End-Uses of Nanofibres," *Nanotechnology in Construction 3*, vol. ISBN 978-3-642-00979-2, pp. 95-99, 2009.

[18] D.H. Reneker, A.L. Yarin, H. Fong, and S. Koombhongse, "Bending instability of electrically charged liquid jets of polymer solutions in electrospinning," *J. Appl. Phys.*, vol. 87, 4531–4547, 2000.

[19] C. Burger, B. S. Hsiao, and B. Chu, "Nanofibrous Materials and Their Applications," *Annu. Rev. Mater. Res.,* vol. 36, pp. 333–368, 2006.

[20] W.J. Li, C. T. Laurencin, E. J. Caterson, R. S. Tuan, and F. K. Ko, "Electrospun nanofibrous structure: A novel scaffold for tissue engineering," *J. Biomed. Mater. Res.,* vol. 60, pp. 613-621, 2001.

[21] R. Luoh, and H. T. Hahn, "Electrospun nanocomposite fiber mats as gas sensors," *Composites Science and Technology,* vol. 66, pp. 2436–2441, May 2006.

[22] D. Li, M. W. Frey, and A. J. Baeumner, "Electrospun polylactic acid nanofiber membranes as substrates for biosensor assemblies," *Journal of Membrane Science,* vol. 279, pp. 354–363, 2006.

[23] F. Dotti, A. Varesano, A. Montarsolo, A. Aluigi, C. Tonin, and G. Mazzuchetti, "Electrospun porous mats for high efficiency filtration," *Journal of Industrial Textiles*, vol. 37, No. 2, pp. 151-162, Oct. 2007.

[24] S.S. Choi, Y. S. Lee, C. W. Joo, S. G. Lee, J. K. Park, and K. S. Han, "Electrospun PVDF nanofiber web as polymer electrolyte or separator," *Electrochimica Acta,* vol. 50, pp. 339–343, 2004.

[25] S. Lee and S. K. Obendorf, "Use of electrospun nanofiber web for protective textile materials as barriers to liquid penetration," *Textile Research Journal,* vol. 77(9), pp. 696–702, 2007.

[26] W.E. Teo, and S. Ramakrishna, "A review on electrospinning design and nanofiber assemblies," *Nanotechnology,* vol. 17, pp. R89–R106, 2006.

[27] F.W. Billmeyer, *Textbook of polymer science*. New York: John Wiley & Sons, Inc., 1984.

[28] J. Xie, and Y.L. Hsieh, "Ultra-high surface fibrous membranes from electrospinning of natural proteins: casein and lipase enzyme," *Journal of Materials Science,* vol. 38, pp. 2125 – 2133, 2003.

[29] M. Wang, H.J. Jin, D.L. Kaplan, and G.C. Rutledge, "Mechanical properties of electrospun silk fibers," *Macromolecules*, vol. 37, pp. 6856-6864, 2004.

[30] W.K. Son, J.H. Youk, and W.H. Park, "Preparation of ultrafine oxidized cellulose mats via electrospinning," *Biomacromolecules,* vol. 5, pp. 197-201, 2004.

[31] Y.Z. Zhang, B. Su, S. Ramakrishna, and C.T. Lim, “Chitosan nanofibers from an easily electrospinnable UHMWPEO-Doped chitosan solution system,” *Biomacromolecules,* vol. 9, pp. 136–141, 2008.

[32] J.A. Matthews, G.E. Wnek, D.G. Simpson, and G.L. Bowlin, “Electrospinning of collagen nanofibers,” *Biomacromolecules,* vol. 3, pp. 232-238, 2002.

[33] Y. Zhang, H. Ouyang, C.T. Lim, S. Ramakrishna, and Z.M. Huang, “Electrospinning of Gelatin fibers and Gelatin/PCL composite fibrous scaffolds,” *J. of Biomedical Mat. Res. Part B: Applied Biomaterials,* vol. 72B, pp. 156-165, Sep. 2004.

[34] D.L. Woerdeman, P. Ye, S. Shenoy, R.S. Parnas, G.E. Wnek, and O. Trofimova, “Electrospun fibers from wheat protein: Investigation of the interplay between molecular structure and the fluid dynamics of the electrospinning process,” *Biomacromolecules,* vol. 6, pp. 707-712, 2005.

[35] D. Li, and Y. Xia, “Electrospinning of nanofibers: Reinventing the wheel?,” *Advanced materials*, vol. 16, No. 14, pp. 1151-1170, Jul. 2004.

[36] S. Koombhongse, W. Liu, and D.H. Reneker, “Flat polymer ribbons and other shapes by electrospinning,” *Journal of Polymer Science: Part B: Polymer Physics*, vol. 39, pp. 2598-2606, 2001.

[37] X.M. Mo, C.Y. Xu, M. Kotaki, and S. Ramakrishna, “Electrospun P(LLA-CL) nanofiber: a biomimetic extracellular matrix for smooth muscle cell and endothelial cell proliferation,” *Biomaterials,* vol. 25, pp. 1883–1890, 2004.

[38] S.A. Theron, A.L. Yarin, E. Zussman, and E. Kroll, “Multiple jets in electrospinning: experiment and modeling,” *Polymer*, vol. 46, issue 9, pp. 2889–2899, Apr. 2005.

[39] Y. Yang, Z. Jia, Q. Li, L. Hou, H. Gao, L. Wang, and Z. Guan, “Multiple jets in electrospinning,” *in Proc. 2006 8th International conference on properties and applications of dielectric materials*, pp. 940-943.

[40] A.L. Yarin, and E. Zussman, “Upward needleless electrospinning of multiple nanofibers,” *Polymer*, vol. 45, issue 9, pp. 2977-2980, Mar. 2004.

[41] J. Kameoka, R. Orth, Y. Yang, D. Czaplewski, R. Mathers, G.W. Coates and H.G. Craighead, ”A scanning tip electrospinning source for deposition of oriented nanofibres,” *Nanotechnology*, vol. 14, pp. 1124–1129, 2003.

[42] T. Miloh, B. Spivak, A.L. Yarin, "Needleless electrospinning: Electrically driven instability and multiple jetting from the free surface of a spherical liquid layer," *Journal of Appl. Phys.*, vol. 106, issue 11, pp. 114910-114910-8, Dec. 2009.

[43] D. Lukas, A. Sarkar, and P. Pokorny, "Self-organization of jets in electrospinning from free liquid surface: A generalized approach," J. Appl. Phys., vol. 103, issue 8, pp. 084309-084309-7, Apr. 2008.

[44] O.O. Dosunmu, G.G. Chase, W. Kataphinan, and D.H. Reneker, "Electrospinning of polymer nanofibres from multiple jets on a porous tubular surface," *Nanotechnology*, vol. 17, pp. 1123–1127, Feb. 2006.

[45] O. Jirsak, F. Sanetrnik, D. Lukas, Z. Na, and V. Koteck, CZ Patent WO2005024101 2005.

[46] F.L. Zhou, R.H. Gong, and I. Porat, "Mass production of nanofibre assemblies by electrostatic spinning," *Polym Int.* vol. 58, pp. 331–342, 2009.

[47] http://www.elmarco.com/nanofiber-equipment/

[48] A.K. Haghi and M. Akbari, "Trends in electrospinning of natural nanofibers," *Phys. Stat. Sol.,* vol. 204, No. 6, pp. 1830–1834, 2007.

[49] Y.M. Shin, M.M. Hohman, M.P. Brenner, and G.C. Rutledge, "Experimental characterization of electrospinning: the electrically forced jet and instabilities," *Polymer,* vol. 42, pp. 9955-9967, 2001.

[50] J.S. Lee, K.H. Choi, H.D. Ghim, S.S. Kim, D.H. Chun, H.Y. Kim, and W.S. Lyoo, "Role of molecular weight of atactic Poly(vinyl alcohol) (PVA) in the structure and properties of PVA nanofabric prepared by electrospinning," *Journal of Applied Polymer Science*, vol. 93, pp.1638–1646, 2004.

[51] S. Megelski, J.S. Stephens, D.B. Chase, and J.F. Rabolt, "Micro and nanostructured surface morphology on electrospun polymer fibers," *Macromolecules*, vol. 35, pp. 8456-8466, 2002.

[52] K.J. Pawlowski, H.L. Belvin, D.L. Raney, J. Su, J.S. Harrison, and E.J. Siochi, "Electrospinning of a micro-air vehicle wing skin," *Polymer*, vol. 44, pp. 1309–1314, 2003.

[53] S. Zhao, X. Wu, L. Wang, and Y. Huang, "Electrospinning of Ethyl–Cyanoethyl Cellulose/Tetrahydrofuran Solutions," *Journal of Applied Polymer Science*, vol. 91, pp. 242–246, 2004.

[54] X. Zong, K. Kim, D. Fang, S. Ran, B.S. Hsiao, and B. Chu, "Structure and process relationship of electrospun bioabsorbable nanofiber membranes," *Polymer,* vol. 43, pp. 4403–4412, 2002.

[55] M.M. Demir, I. Yilgor, E. Yilgor, and B. Erman, "Electrospinning of polyurethane fibers," *Polymer,* vol. 43, pp. 3303-3309, 2002.

[56] R.V.N. Krishnappa, K. Desai, and C. Sung, "Morphological study of electrospun polycarbonates as a function of the solvent and processing voltage," *Journal of Materials Science,* vol. 38, pp. 2357 – 2365, 2003.

[57] T. Jarusuwannapoom, W. Hongrojjanawiwat, S. Jitjaicham, L. Wannatong, M. Nithitanakul, C. Pattamaprom, P. Koombhongse, R. Rangkupan, and P. Supaphol, "Effect of solvents on electro-spinnability of polystyrene solutions and morphological appearance of resulting electrospun polystyrene fibers," *European Polymer Journal,* vol. 41, pp. 409–421, 2005.

[58] L. Wannatong, A. Sirivat and P. Supaphol, "Effects of solvents on electrospun polymeric fibers: preliminary study on polystyrene," *Polymer Int.,* vol. 53, pp. 1851–1859, 2004.

[59] C. J. Buchko, L. C. Chen, Y. Shen, and D.C. Martin, "Processing and microstructural characterization of porous biocompatible protein polymer thin films," *Polymer,* vol.40, pp. 7397–7407, 1999.

[60] Y. Yang, Z. Jia, J. Liu, L. Wang, and Z. Guan, "Effect of solution rate on electrospinning," *Annual Report Conference on Electrical Insulation and Dielectric Phenomena,* pp. 615-618, 2007.

[61] W.K. Son, J.H. Youk, T.S. Lee, and W.H. Park, "The effects of solution properties and polyelectrolyte on electrospinning of ultrafine poly(ethylene oxide) fibers," *Polymer,* vol. 45, pp. 2959–2966, 2004.

[62] X. Yuan, Y. Zhang, C. Dong, and J. Sheng, "Morphology of ultrafine polysulfone fibers prepared by electrospinning," *Polym Int*, vol. 53, pp. 1704–1710, 2004.

[63] E. Biber, G. Gündüz, B. Mavis, and U. Colak, "Effects of electrospinning process parameters on nanofibers obtained from Nylon 6 and poly (ethylene-n-butyl acrylate-maleic anhydride) elastomer blends using Johnson SB statistical distribution function," *Appl Phys A*, vol. 99, pp. 477–487, Feb. 2010.

[64] C. Minghsu, and S. Shivkumar, "Nano-sized beads and porous fiber constructs of Poly(ε-caprolactone) produced by electrospinning," *Journal of Materials Science*, vol. 39, pp. 3003-3013, 2004.

[65] L. S. Nair, S. Bhattacharyya, J. D. Bender, Y. E. Greish, P. W. Brown, H. R. Allcock, and C. T. Laurencin, "Fabrication and Optimization of Methylphenoxy Substituted Polyphosphazene Nanofibers for Biomedical Applications," *Biomacromolecules*, vol. 5, pp. 2212-2220, July 2004.

[66] J. Macossay, A. Marruffo, R. Rincon, T. Eubanks,and A. Kuang, "Effect of needle diameter on nanofiber diameter and thermal properties of electrospun poly(methyl methacrylate)," *Polym. Adv. Technol,.*vol. 18, pp. 180–183, Feb. 2007.

[67] S.L. Shenoya, W.D. Batesa, H.L. Frisch, and G.E. Wnek, "Role of chain entanglements on fiber formation during electrospinning of polymer solutions: good solvent, non-specific polymer–polymer interaction limit," *Polymer,* vol. 46, pp. 3372–3384, 2005.

[68] H. Fong, I. Chun, and D.H. Reneker, "Beaded nanofibers formed during electrospinning," *Polymer,* vol. 40, pp. 4585–4592, 1999.

[69] Y. Christanti, and L.M. Walker, "Surface tension driven jet break up of strain-hardening polymer solutions," *J. Non-Newtonian Fluid Mech.,* vol. 100, pp. 9–26, 2001.

[70] S.J. Kim, C.K. Lee, and S.I. Kim "Effect of ionic salts on the processing of Poly(2-acrylamido-2-methyl-1-propane sulfonic acid) nanofibers," *Applied Polymer Science,* vol. 96, No. 4, pp. 1388-1393, 2005.

[71] W.K. Son, J.H. Youk, T.S. Lee, and W.H. Park, "Electrospinning of ultrafine cellulose acetate fibers: Studies of a new solvent system and deacetylation of ultrafine cellulose acetate fibers," *J. of Polymer Science: Part B: Polymer Physics*, vol. 42, pp. 5-11, 2004.

[72] J.S. Choi, S.W. Lee, L. Jeong, S.H. Bae, B.C. Min, J.H. Youk, and W.H. Park, "Effect of organosoluble salts on the nanofibrous structure of electrospun poly(3-hydroxybutyrate-co-3-hydroxyvalerate)," *International Journal of Biological Macromolecules*, vol. 34, pp. 249–256, 2004.

[73] A.K. Moghe, R. Hufenus, S.M. Hudsona, and B.S. Gupta, "Effect of the addition of a fugitive salt on electrospinnability of poly(3-caprolactone)," *Polymer*, vol. 50, pp. 3311–3318, May 2009.

[74] J. Stanger, N. Tucker, K Kirwan, and M.P. Staiger, "Effect of Charge Density on the Taylor cone in Electrospinning," *International Journal of Modern Physics B*, vol. 23, nos. 6 & 7, pp. 1956–1961, 2009.

[75] D. Garoz, C. Bueno, C. Larriba, S. Castro, I. Romero-Sanz, J. Fernandez de la Mora, Y. Yoshida, and G. Saito, "Taylor cones of ionic liquids from capillary tubes as sources of pure ions: The role of surface tension and electrical conductivity," *Journal of Applied Physics*, vol.102, pp. 064913-10, Sep. 200.

[76] S. N. Reznik, A. L. Yarin, and A. Theron, "Transient and Steady Shapes of Droplets Attached to a Surface in a Strong Electric Field," *J. Fluid Mech*., vol. 516, pp. 349–377, Mar. 2004.

[77] J. F. A. de la Mora, "The Fluid Dynamics of Taylor Cones," *Annu. Rev. Fluid Mech*., vol. 39, pp. 217–243, 2007.

[78] T.A. Kowalewski, S. Barral and T. Kowalczyk, "Modeling Electrospinning of Nanofibers," *In Proc. IUTAM Symposium on Modelling Nanomaterials and Nanosystems*, Aalborg, 2008, pp. 279-292.

[79] A.L. Yarin, S. Koombhongse, and D.H. Reneker, "On bending instability in electrospinning of nanofibers," *J. Appl. Phys*., vol. 89, no. 5, pp. 3018–3026, Mar. 2001.

[80] N.J. Pinto, R. González, A.T. Johnson, and A.G. MacDiarmid, "Electrospun hybrid organic/inorganic semiconductor Schottky nanodiode," Applied Physics Letters, vol. 89, no. 3, pp. 033505 - 033505-3, Jul. 2006.

[81] N.J. Pinto, A.T. Johnson, A.G. MacDiarmid, C.H. Mueller, N. Theofylaktos, D.C. Robinson, and F.A. Miranda, "Electrospun polyaniline/polyethylene oxide nanofiber field-effect transistor," Applied Physics Letters, vol. 83, no. 20, pp. 4244-4246, Nov. 2003.

[82] S.A. Theron, E. Zussman, and A.L. Yarin, "Experimental investigation of the governing parameters in the electrospinning of polymer solutions," *Polymer,* vol. 45, pp. 2017–2030, 2004.

[83] K.H. Lee, H.Y. Kim, M.S. Khil, Y.M. Ra, and D.R. Lee, "Characterization of nano-structured poly(ε-caprolactone) nonwoven mats via electrospinning," *Polymer,* vol. 44, pp. 1287–1294, 2003.

[84] S. D. Vrieze, T. V. Camp, A. Nelvig, B. Hagström, P. Westbroek, and K. De Clerck, "The effect of temperature and humidity on electrospinning," *Journal of materials science*, vol. 44, no. 5, pp. 1357-1362, 2009.

[85] C. Wang, Y. W. Cheng, C. H. Hsu, H. S. Chien, and S. Y. Tsou, "How to manipulate the electrospinning jet with controlled properties to obtain uniform fibers with the smallest diameter?—a brief discussion of solution electrospinning process," *Journal of Polymer Research,* vol. 18, no. 1, pp. 111-123, Feb. 2010.

[86] C.L. Casper, J.S. Stephens, N.G. Tassi, D.B. Chase, and J.F. Rabolt, "Controlling surface morphology of electrospun polystyrene fibers: Effect of humidity and molecular weight in the electrospinning process," *Macromolecules,* vol. 37, pp. 573-578, 2004.

[87] D. Li and Y. Xia, "Direct fabrication of composite and ceramic hollow nanofibers by electrospinning," *Nano letters*, vol. 4, No. 5, pp. 933-938, 2004.

[88] R.P.A. Hartman, D.J. Brunner, D.M.A. Camelot, J.C.M. Marijnissen and B. Scarlett, "Electrohydrodynamic atomization in the cone-jet mode physical modeling of the liquid cone and jet," *J. Aerosol Sci.,* vol. 30, No. 7, pp. 823-849, 1999.

[89] F. Yan, B. Farouk, and F. Ko, "Numerical modeling of an electrostatically driven liquid meniscus in the cone-jet mode," Aerosol Science, vol. 34, pp. 99–116, 2003.

[90] A.L. Yarin, S. Koombhongse and D.H. Reneker, "Taylor cone and jetting from liquid droplets in electrospinning of nanofibers," *Journal of Appl. Phy.,* vol. 90, No. 9, pp. 4836-4836, Nov.2001.

[91] A.F. Spivak, and Y.A. Dzenisa, "Asymptotic decay of radius of a weakly conductive viscous jet in an external electric field," *Appl. Phy. Letters*, vol. 73, No. 21, Nov. 1998.

[92] J.H. He, Y. Wu, and W.W. Zuo, "Critical length of straight jet in electrospinning," *Polymer,* vol. 46, pp. 12637–12640, 2005.

[93] M.M. Hohman, M. Shin, G. Rutledge, and M.P. Brenner, "Electrospinning and electrically forced jets. I. Stability theory," *Physics of Fluids,* vol. 13, No. 8, pp. 2201-2220, Aug. 2001.

[94] J.J. Feng, "The stretching of an electrified non-Newtonian jet: A model for electrospinning," *Physics of Fluids,* vol. 14, No. 11, pp. 3912-3926, Nov. 2002.

[95] A.L. Yarin, S. Koombhongse, and D.H. Renekera, "Bending instability in electrospinning of nanofibers," *Journal of Applied Phy.,* vol. 89, No. 5, pp. 3018-3026, Mar. 2001.

[96] T.A. Kowalewski, S. Błonski, and S. Barral, "Experiments and modelling of electrospinning process," *Bulletin of the polish academy of sciences: Technical sciences,* vol. 53, No. 4, 2005.

[97] M. A. Salam, M. Nakano, and A. Mizuno, "Electric fields and corona currents in needle-to-meshed plate gaps," *J. Phys. D: Appl. Phys.*, vol. 40, pp. 3363–3370, May 2007.

[98] E. Kuffel, W.S. Zaengl, and J. Kuffle, "High Voltage Engineering Fundamentals," Second Edition 2000, published by Butterworth-Heinemann.

[99] User's guide, COMSOL® Multiphysics 3.5a.

[100] User's manual, Keithley model 6514 programmable electrometer.

[101] A.W. Adamson and A.P. Gast, Physical chemistry of surfaces, 6th ed., New York: Wiley, 1997.

[102] R. Baba, C.J. Angammana, and S.H. Jayaram, "Electrospinning of Alginate and Poly-ethylene Oxide Blends Using Pulsed Electric Fields to Fabricate Chopped Nanofibres," *The annual conference of ESA*, Charlotte, USA, June 2010.

[103] R. Baba, "Design of an IGBT-Based Pulsed Power Supply for Non-continuous-mode Electrospinning," Master Thesis, University of Waterloo, Canada, 2010.

[104] A. Saville, ''Electrohydrodynamics: The Taylor–Melcher leaky dielectric model,'' *Annu. Rev. Fluid Mech*., vol. 29, pp.27-64, Jan. 1997.

[105] W. T. Grubb and D. W. Mckee, "Frequency assignment in infra-red spectrum of water," *Nature*, vol. 210, no. 5032, pp. 194-195, April 1966.

[106] R. L. Pecsok, L. D. Shields, T. Cairns, and I. G. Mcwilliam, "Modern methods of chemical analysis," Second Edition 1976, published by John Wiley & Sons.

[107] S. Bian, C.J. Angammana, and S.H. Jayaram, "Use of Electrospinning to Improve the Dispersion of Inorganic Nanofillers in Silicone Rubber," *The annual conference of ESA*, Charlotte, USA, June 2010.

[108] A. M. Ganon-Calvo, "On the theory of electrohydrodynamically driven capillary jets," *J. Fluid Mech.*, vol. 335, pp. 165-188, 1997.

[109] J.H. He, Y.Q. Wan, and J.Y. Yu, "Allometric Scaling and Instability in Electrospinning," *International Journal of Nonlinear Sciences and Numerical Simulation*, vol. 5, no. 3, pp. 243-252, 2004.

[110] D.D. Ebbing and S.D Gammon, *General chemistry*. New york: Houghton Mifflin Company, Eighth edition, 2005.

[111] Instruction Manual, Model 6514, system electrometer.

[112] I. R. Vázquez, "A Study of Nanofilled Silicone Dielectrics for Outdoor Insulation," PhD Thesis, University of Waterloo, Canada, 2009.

[113] H. Nie, A. He, W. Wu, J. Zheng, S. Xu, J. Li, and C. C. Han, "Effect of poly(ethylene oxide) with different molecular weights on the electrospinnability of sodium alginate," *Polymer,* vol. 50, pp. 4926–4934, 2009.

# Appendix A

Table A-1: Polymers that have been electrospun successfully into nanofibres.

| Synthetic Polymer | Natural Polymer | Polymer Blends |
|---|---|---|
| Nylon 6, Nylon 4,6, and Nylon 6,6 | Collagen | Polyvinylchloride/ Polyurethene |
| Polyacrylic acid (PAA) | Bombyx mori silk | Bombyx mori silk/fibroin/ Polyethylene oxide (PEO) |
| Polyacrylonitrile (PAN) | Cellulose acetate | Casein/Polyethylene oxide (PEO) |
| Polycarbonate (PC) | Chitosan | Casein/Polyvinyl alcohol (PVA) |
| Polyetherimide (PEI) | Fibrinogen | Chitosan/Polyethylene oxide |
| Polyethylene oxide (PEO) | Gelatine | Gelatin/Polycaprolactone (PCL) |
| Polyethylene terephthalate (PET) | Wheat gluten | Gelatin/Poly-L-lactide-co-ε-caprolactone (PLCL) |
| Polystyrene (PS) | Chitin | Alginate/Polyethylene oxide (PEO) |
| Polysulfone | | Gelatine/Alginate |
| Polyurethane (PUR) | | Alginate/Polyvinyl alcohol |
| Polyvinyl alcohol (PVA) | | Polyaniline (PANI)/ Polyethylene oxide (PEO) |
| Polyvinylpyrrolidone (PVP) | | Polyaniline (PANI)/ Polystyrene (PS) |
| Polyvinylidene fluoride (PVDF) | | Collagen/Polycaprolactone (PCL) |
| Polyvinylcarbazole (PVK) | | Carboxymethyl chitin (CMC) /Polyvinyl alcohol (PVA) |
| Polyvinyl chloride (PVC) | | |
| Polyvinylidene fluoride-co-hexafluropropylene) (PVDF-HFP) | | |
| Poly(ε-caprolactone) | | |
| Polydioxanone (PDS) | | |
| Polyglycolide (PGA) | | |
| Poly-L-lactic acid (PLLA) | | |
| Poly-L-lactide-co-glycolide (PLGA) | | |
| Poly-L-lactide-co-ε-caprolactone (PLCL) | | |
| Polybenzimidazol (PBI) | | |

# Appendix B

The following one-dimensional differential equation for electrospun jet radius was derived by Spivak et al.

$$\frac{d}{dZ}\left\{R^{-4}+WeR^{-1}-\mathrm{Y}R^{2}-\frac{1}{\mathrm{Re}}\left[\frac{1}{2}\frac{d}{dZ}\left(R^{-2}\right)\right]^{m}\right\}=1 \tag{B-1}$$

Where,

$\rho$ – Fluid density

$Q$ – Constant volumetric flow rate

$I$ – Constant total jet current

$E_0$ – Electric field

$R_0$ – Jet radius at capillary orifice

$\sigma_s$ – Surface tension of the solution

$\varepsilon_0$ – Permittivity of air

$\mu$- Solution viscosity

$m$ – Flow index

$r$ – Actual jet radius at distance z

$Z_0 = \rho Q^3 / 2\pi^2 R_0^4 E_0 I$

$Z = z/Z_0$ – Dimensionless axial coordinate

$R = r/R_0$ – Dimensionless jet radius at distance $Z$

$We = 2\pi^2 R_0^3 \sigma_s / \rho Q^2$ - Weber number

$\mathrm{Y} = \pi^2 I^2 R_0^6 / 4\varepsilon_0 \rho Q^4$ - Ratio of electric force to inertia force

$\mathrm{Re} = \rho Q^2 / \left(2\pi^2 R_0^4 \mu\right)\left[\left(4\pi E_0 I R_0^2\right)/\left(\rho Q^2\right)\right]^{-m}$ - Reynolds number

Chauchy's inequality

$$ab \le \frac{1}{4}(a+b)^2, \quad a>0,\ b>0 \tag{B-2}$$

where $a$ and $b$ are real numbers.

# Appendix C

Table C-1: Symbols used in Hohman's work [93].

| | |
|---|---|
| $h$ | Radius of the jet |
| $v$ | Fluid velocity parallel to the axis of the jet |
| $\sigma$ | Surface charge density |
| $K$ | Conductivity of the liquid |
| $r_0$ | Nozzle diameter |
| $\rho$ | Density of the liquid |
| $\gamma$ | Surface tension of the liquid |
| $\varepsilon$ | Dielectric constant of the liquid |
| $\varepsilon_0$ | Dielectric constant of air |
| $E$ | Electric field parallel to the axis of the jet |
| $g$ | Gravitational acceleration |
| $\nu$ | Kinematics viscosity of the solution |
| $\chi$ | Local aspect ratio (slope of the cone) |
| $E_\infty$ | Applied electric field |
| $z$ | Dimensionless axial coordinate |
| $t$ | Dimensionless time |
| $K^*$ | $K\sqrt{r_0^3\rho/(\gamma\beta)}$ - Dimensionless conductivity |
| $\beta$ | $\varepsilon/\varepsilon_0 - 1$ |
| $g^*$ | $g\rho r_0^2/\gamma$ - Dimensionless gravitational acceleration |
| $\nu^*$ | $\sqrt{l_\nu/r_0}$ - Dimensionless viscosity |
| $l_\nu$ | $\rho\nu^2/\gamma$ |
| $\Omega_0$ | $E_\infty/E_0$ |
| $E_0$ | $\gamma/(\varepsilon-\varepsilon_0)r_0$ |
| $t_0$ | $\sqrt{\rho r_0^3/\gamma}$ - Time scale |

# Appendix D

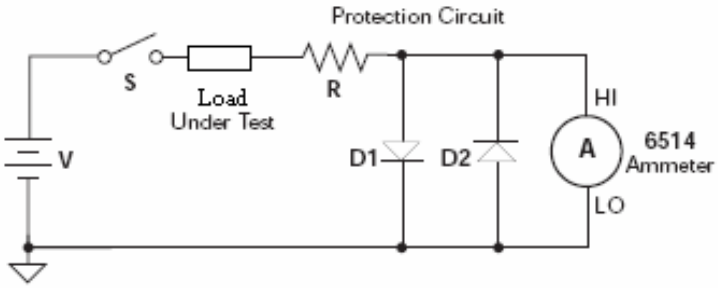


Fig. D-1. Protection circuit that is used for electrometer protection [111].

Silicone is the general term to describe the family of organo-silicon compounds based on a molecular chain of alternating silicon and oxygen atoms. A detailed discussion of silicone rubber can be found in [112].

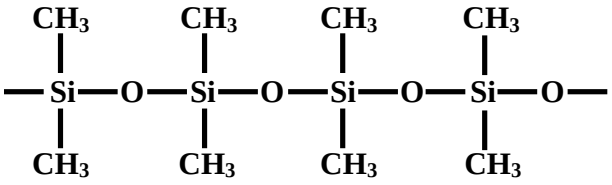


Fig. D-2. Chemical structure of silicone rubber.

Alginate consists of mannuronate (M) and guluronate (G) arranged in a non-regular block wise pattern with varying proportions of GG, MG, and MM units [113].

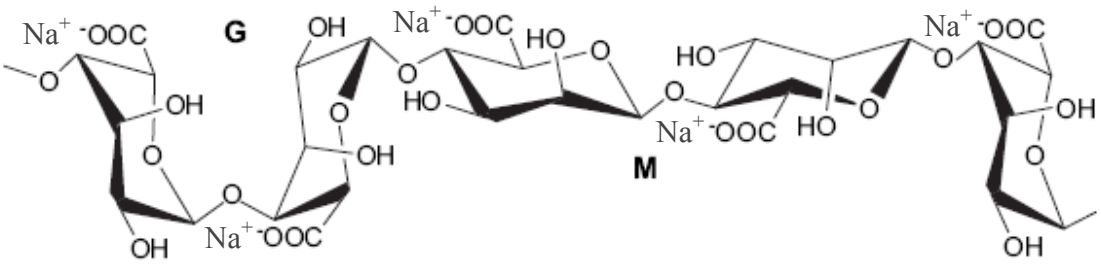


Fig. D-3. Chemical structure of sodium alginate.

# Appendix E

Table E-1: Symbols used in Equations (7.2) – (7.5).

| | |
|---|---|
| $R$ | Jet radius |
| $v$ | Axial velocity |
| $Q$ | Volume flow rate |
| $E$ | *z-axis* component of the electric field |
| $K$ | Conductivity of the liquid |
| $\sigma$ | Surface charge density |
| $\alpha$ | Surface charge parameter |
| $\rho$ | Density of the liquid |
| $g$ | Acceleration of gravity ($9.81 m/s^2$) |
| $\eta$ | Viscosity of the liquid |
| $\gamma$ | Surface tension of the liquid |
| $\varepsilon$ | Dielectric constant of the liquid |
| $\bar{\varepsilon}$ | Dielectric constant of ambient air |
| $E_\infty$ | External electric field |
| $L$ | Entire length of the fibre |
| $R_0$ | Characteristic radius of the jet |
| $R'$, $v'$, $E'$, $\sigma'$ | First derivatives of respective variables with respect to $z$ |
| $\chi$ | $L/R_0$ - Aspect ratio |
| $\beta$ | $\varepsilon / \bar{\varepsilon} - 1$ |

# Appendix F

## List of Experiments